Pathways of Denmark Strait Overflow Water in the Subpolar North Atlantic

A Lagrangian Perspective

Irene Backers

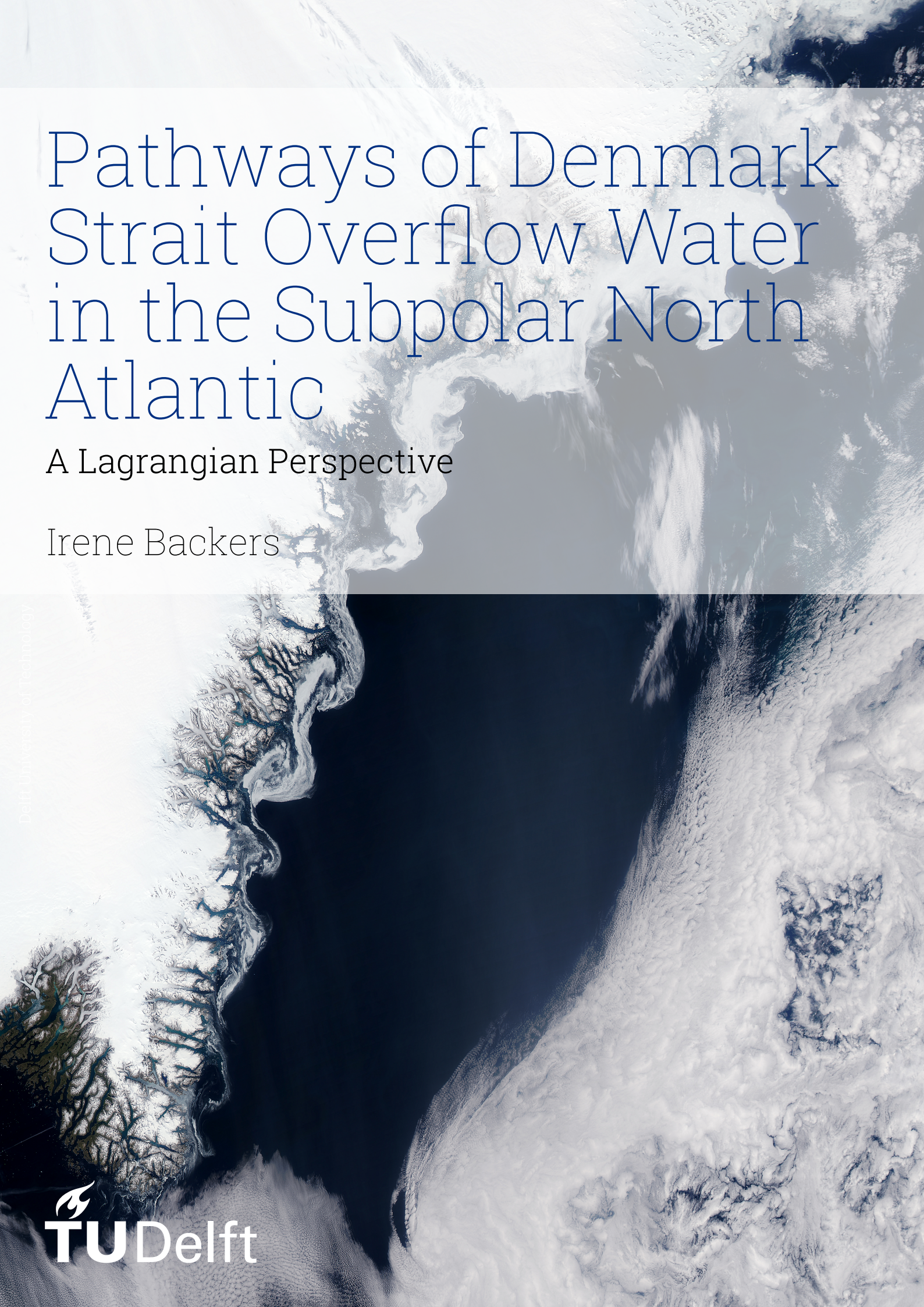

Delft University of Technology

TU Delft

Pathways of Denmark Strait Overflow Water in the Subpolar North Atlantic

A Lagrangian Perspective

by

Irene Backers

to obtain the degree of Master of Science

at the Delft University of Technology,

to be defended publicly on Wednesday December 3, 2025 at 13:00 .

Student number:	4960947	
Project duration:	March 2025 – November 2025	
Thesis committee:	Dr. ir. R. Gelderloos,	TU Delft, Chair
	D.H.A. Vermeulen, Msc MA	TU Delft, Daily Supervisor
	Dr. M. Vizcaino,	TU Delft

Cover:	Sea Ice near Greenland (NASA Earth Observatory)
Style:	TU Delft Report Style, with modifications by Daan Zwaneveld

An electronic version of this thesis is available at http://repository.tudelft.nl/.

TU Delft

Preface

The completion of this master thesis marks the end of my academic journey at the TU Delft at both the faculty of Electrical Engineering, Mathematics and Computer Science and at the faculty of Civil Engineering and Geosciences. Over the years, I have grown both personally and intellectually, with this thesis being a challenging yet insightful part of my studies.

I would like to express my gratitude to my main supervisor Renkse Gelderloos and daily supervisor Dennis Vermeulen for the inspirational discussions and continues support. Their input and motivation during our weekly meetings has shaped this thesis to the report I can proudly present today. I would moreover like to thank Miren Vizcaino for being part of my thesis committee and her sharp questions during the milestone meetings .

A heartfelt thank you to my fellow students and friends for their inspiration, discussions and moral support during our frequent study sessions. Last but definitely not least I would like to thank my family for their unconditional support trough the entire journey.

Irene Backers
Delft, November 2025

Abstract

Denmark Strait Overflow Water (DSOW) forms a major component of the deep limb of the Atlantic Meridional Overturning Circulation (AMOC). This study investigates the main pathways along which DSOW spreads through the subpolar North Atlantic (SPNA) and how its temperature, salinity and density evolve along these routes. We used a Lagrangian particle-tracking approach based on velocity and tracer fields from the Global Ocean Physics Analysis and Forecast system provided by Copernicus Marine Service. Particles were released at the Denmark Strait sill and tracked for three years. We found that DSOW spreads throughout the SPNA via pathways where particles stay in the boundary current and pathways where particles follow both the boundary current and enter an interior. The highest percentage of particles (72.4%) travels via only the boundary current; of the interiors, the Labrador Sea interior is most frequently entered (23.0%), while exchanges with the Irminger Sea (4.4%) interior is smaller. The fraction of particles entering an interior is highest in winter (36%), consistent with enhanced density gradients and eddy activity. Along its pathways, DSOW warms and becomes more saline through mixing with ambient waters. Particles that stay in the boundary currents experience the largest changes in temperature (+14° C), salinity (+2.5 g/kg) and density (-1.2 kg/m^3, while particles that enter an interior experience smaller changes (temperature +9° C, salinity +0.5 g/kg and density -0.7 kg/m^3). Particles that travel via both the boundary current and enter an interior also experience the largest changes in density in the boundary current. These findings suggest that most transport and transformation of DSOW occurs within the boundary current, while exchange with the interior plays a smaller role.

Contents

List of Figures

List of Tables

Nomenclature

Abbreviations

Abbreviation	Definition
AMOC	Atlantic Meridional Overturning Circulation
BC	Boundary Current
CF	Cape Farewell
DS	Denmark Strait
DSO	Denmark Strait Overflow
DSOW	Denmark Strait Overflow Water
DWBC	Deep Western Boundary Current
EGC	East Greenland Current
EGCC	East Greenland Coastal Current
GSR	Greenland-Scotland Ridge
IC	Irminger Current
IcB	Iceland Basin
IrS	Irminger Sea
ISOW	Iceland Scotland Overflow Water
ITCZ	Intertropical convergence zone
LC	Labrador Current
LS	Labrador Sea
NAC	North Atlantic Current
NH	Northern Hemisphere
NIIC	North Icelandic Irminger Current
SH	Southern Hemisphere
PGF	Pressure gradient force
RR	Reykjanes Ridge
SPG	Subpolar gyre
SPNA	Subpolar North Atlantic
SST	Sea surface temperature
STG	Subtropical gyre
WGC	West Greenland Current

1

Introduction

The world's oceans are in constant motion and are connected to each other via the thermohaline circulation, also known as the global ocean conveyor belt, and schematised in Figure 1.1. This circulation consists of wind-driven currents at the surface and currents in the deep ocean driven by density differences (NOAA, 2024). The density of seawater depends on both temperature (thermo) and salinity (haline). This relation is non-linear as temperature and salinity have different effects on density for different values; in regions roughly warmer than 4 °C the temperature is most important for determining the density structure, while in regions colder than 4 °C the salinity sets the density structure (McDougall & Barker, 2011).

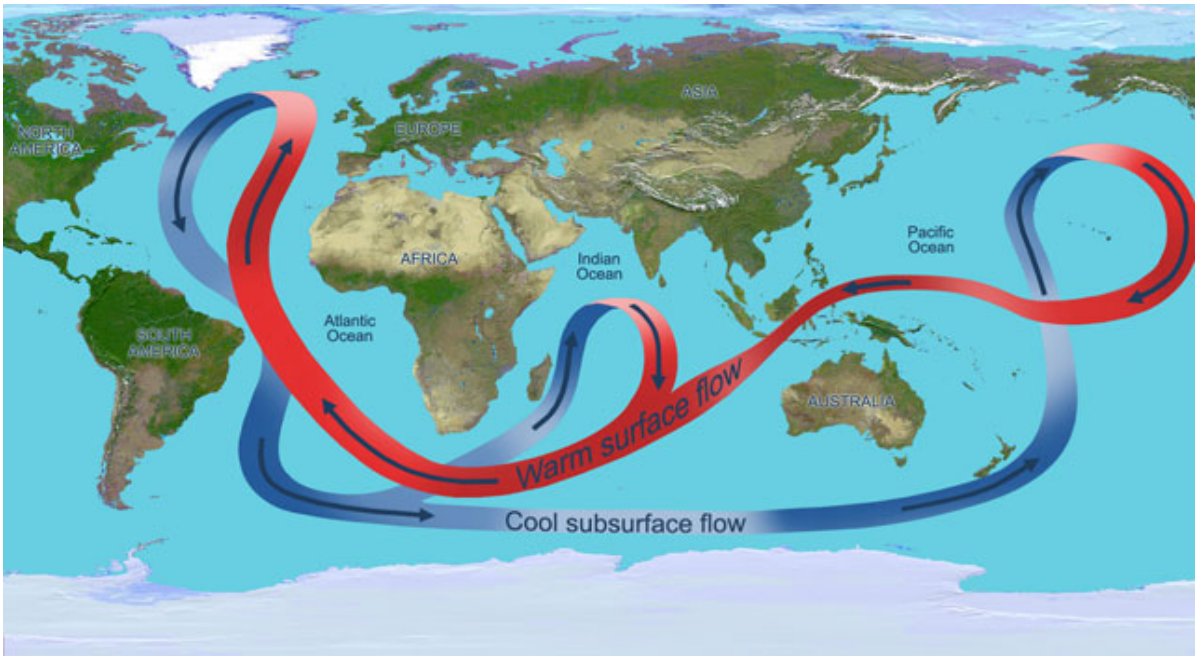

Figure 1.1: A simplified illustration of the overturning circulation of the global ocean. Throughout the Atlantic Ocean, the circulation carries warm waters (red arrows) northward near the surface and cold deep waters (blue arrows) southward. Copied from NASA Jet Propulsion Laboratory (2010).

The Atlantic Meridional Overturning Circulation (AMOC) is a major ocean circulation and part of the thermohaline circulation. Warm surface waters from the equator flow northward along vast distances in the Atlantic. The AMOC in the subtropical North Atlantic at 26° N accounts for 70% of the net poleward heat flux carried by the global oceans (Lavin et al., 1998; Johns et al., 2011) and 25% of the total poleward heat flux carried by both the ocean and the atmosphere at this latitude (Ganachaud and

Wunsch, 2003; Trenberth et al., 2001). The current gradually cools on its journey northward, releasing heat to the atmosphere. In the subpolar and polar regions, the surface waters become dense enough to sink both in density-space and in depth. It forms cold and dense deep waters, which return southward through the Atlantic Ocean. The northward transport of heat due to the AMOC is responsible for the relatively mild climate in (Western) Europe (Buckley and Marshall, 2016; Georgiou et al., 2021).

1.1. Drivers of Ocean Circulation

This northward surface transport is driven by differences in density of seawater between the (sub)tropical and the polar region and is controlled by two mechanisms, one temperature-driven and the other one salinity-driven (Stommel, 1958, Stommel, 1961). The dominant mechanism is currently the temperature-driven one; the waters at the equator are warm and buoyant, while the waters at the poles are cold and dense. The second mechanism is salinity-driven; in the subtropics there is more evaporation than precipitation which makes the seawater saline and dense. At the poles there is freshwater input from precipitation and ice melt that makes the seawater fresher and more buoyant (Stommel, 1961; Weijer et al., 2019; Rahmstorf, 2024). To understand how this forms a circulation some background theory is needed.

The Earth is unequally heated by the sun; the equator warms more than the polar regions. Warm air at the equator rises, cools and descent to the surface in the subtropics, a phenomenon known as Hadley circulation or the Hadley cell described by Hadley (1735). Earths rotation and the resulting easterly trade winds blowing between the equator and 30°and westerlies between 30° and 60° are key components in creating ocean gyres (Woods Hole Oceanographic Institution, n.d.; NASA Ocean Motion, n.d.). The following theory will be explained for the northern hemisphere; for the southern hemisphere the same principles apply but in the opposite direction. The winds set the upper layer of the ocean into motion in the direction of the wind due to friction. The water is deflected by the Coriolis force to the right resulting in convergence of water around the subtropics. This transport of surface water by wind is known as Ekman transport and was first described by Vagn Walfrid Ekman (1905). This creates a local maximum in sea surface height (SSH) that is about 1 m higher than the global mean sea level (Woods Hole Oceanographic Institution, n.d.; NASA Ocean Motion, n.d.). The pull of gravity creates a pressure gradient force (PGF) that pulls water down hill which is deflected to the right by Coriolis. Since the elevation in SSH is very small compared to the scale of the ocean basin (order 1000's of km) the PGF is very small and balanced by the Coriolis force which is known as geostrophic balance. The resulting geostrophic flow is clockwise along the isobars. In the North Atlantic Ocean; this creates the subtropical gyre (STG) centred around 30° N.

At mid latitudes something similar is happening and the subpolar gyre (SPG), centred around 60° N, is formed. Mid latitude westerlies and polar easterlies result in a diverging Ekman transport and a local minimum in SSH. The PGF points inward and is balanced again by Coriolis so that a counter-clockwise rotation forms. The gyres can be compared to high and low pressure systems in the atmosphere, where the STG is a region of high pressure and the SPG a region of low pressure. Exchange between the two gyres can take place at the south of the SPG and the north of the STG where the gyres meet and both flow to the east. This can happen via eddies and cross isobaric components of the flow due to friction from wind or topography. In the case of a cross isobaric component this would be from STG (high pressure) to SPG (low pressure), analogous to flow in the atmosphere.

The anti-cyclonic motion of the STG and the cyclonic motion of the SPG together with downwelling of cold dense water in subpolar regions makes the AMOC to be temperature driven with surface currents to the north and deep currents to the south. If the influence of temperature decreases and the influence of salinity increases this will have effects on the circulation. Freshwater inflow from precipitation and ice melt make the polar waters less dense. In the subtropics on the other hand, there is more evaporation than precipitation making water more saline and dense. This would result in less downwelling at the poles and more downwelling in the subtropics, which opposes the temperature-driven circulation and can result in a weaker northward transport or in extreme cases a southward surface transport if it were dominant.

1.2. Area of Interest: Seas, Topographic Features and Currents

The area of interest of this thesis is the subpolar North Atlantic (SPNA), which is bounded by Scotland, the Faroe Islands, Iceland, Greenland and the Labrador Coast (Canada). The area is characterised by three basins: the Iceland Basin, the Irminger Sea and the Labrador Sea. Figure 1.2 is a schematic of the SPNA and adjacent seas showing topographic features and the main currents. Other topographic features of interest in this thesis are the Rockall Trough to the north-west of Great Britain and Ireland, the Reykjanes Ridge (RR) separating the Iceland Basin and Irminger Sea, the Greenland-Scotland Ridge (GSR) separating the SPNA from the Nordic Seas north of Iceland, Denmark Strait (DS) between Greenland and Iceland, Davis Strait between Canada and Greenland and the Grand Banks to the south-east of Newfoundland.

Main currents are shown in Figure 1.2 and will be named if they reappear later in our study. Red/orange/yellow arrows denote currents associated with poleward heat and salt transport while blue arrows denote currents associated with transport of Arctic-origin waters into the North Atlantic. The SPG is outlined by the red shading. The circulation in the SPNA can generally be described by a strong cyclonic boundary current and a relatively quiescent flow in the interior of the basin (Lavender et al., 2000). Around 45° N the North Atlantic Current (NAC) forms the boundary between the SPG and the STG. It brings warm and salty water from the tropics and subtropics from west to east across the North Atlantic towards Europe, forming the upper branch of the AMOC (Higginson et al., 2011; Klein and Siedler, 1989). West of the European continental shelf, the NAC splits into three banches; one southward branch as part of the STG and two northward branches. One branch goes via the Rockall Trough and crosses the GSR into the Nordic Seas. The second branch flows towards the Iceland Basin where it splits again in two parts. One branch flowing over the GSR to the Nordic Seas and one branch that flows around the Iceland Basin. This second branch becomes the Irminger Current (IC), which crosses the RR, flows north along the west side of the RR and around the Irminger Sea (Bower et al., 2019). A small part of the IC crosses the GSR and continues to the Nordic Seas as the North Icelandic Irminger Current (NIIC). At the East coast of Greenland, the IC is accompanied by the cold and fresh East Greenland Current (EGC) flowing along the shelf break of the East Greenland shelf (Pickart et al., 2005). Not shown in Figure 1.2 is the East Greenland Coastal Current (EGCC) that flows on the East Greenland shelf between DS and Cape Farewell (CF), the most southern tip of Greenland, and has very low salinity (Bacon, 2002). At CF the currents continue along the west coast of Greenland. As the EGC and IC have comparable velocities, the currents are thought to continue as the West Greenland Current (WGC) on the continental shelf (Pickart et al., 2005; Gascard and Clarke, 1983; Fratantoni and Pickart, 2007). The differences in thermohaline properties between the currents remain with the cold fresh Arctic-origin water sitting above the warmer more saline Atlantic-origin water (Yashayaev, 2007). Upon reaching the northern part of the Labrador Sea, the WGC splits in a part that continues to flow north through Davis Strait (Curry et al., 2014) and a part that flows around the Labrador Sea. It is joined by cold and fresh outflow from Davis Strait and together they form the Labrador Current (LC) (Lazier & Wright, 1993). At the Grand Banks the LC splits in one southward branch along the continental shelf and one part that bends east into the NAC.

Also shown in Figure 1.2 but not directly relevant to this study are the Hudson Strait, Baffin Bay, Baffin Island Current (BIF), Eastern Icelandic Current (EIC), Greenland Sea, Norwegian Sea, Iceland Sea and North Sea.

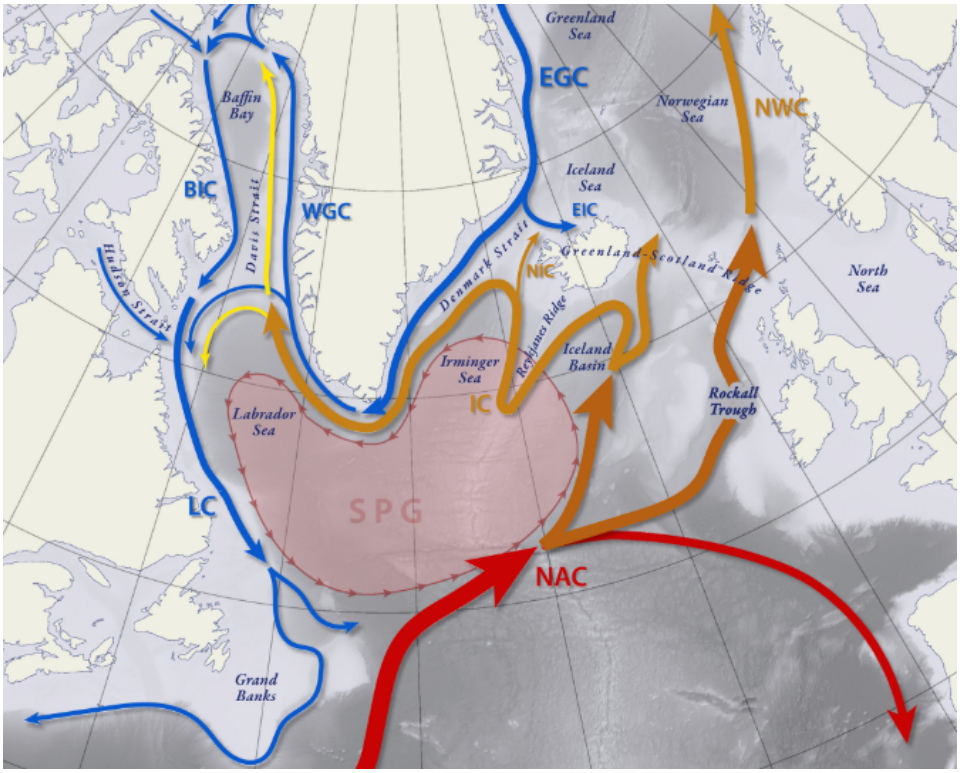

Figure 1.2: Schematic of the main currents in the SPNA and adjacent seas. Red/orange/yellow arrows denote currents associated with poleward heat and salt transport while blue arrows denote currents associated with transport of Arctic-origin waters into the North Atlantic. BIC, Baffin Island Current; EGC, East Greenland Current; EIC, Eastern Icelandic Current; IC, Irminger Current; LC, Labrador Current; NAC, North Atlantic Current; NIC, North Icelandic Irminger Current; NWC, Norwegian Current; WGC, West Greenland Current. The outline of the subpolar gyre (SPG) is shown as red contour. Gray shading denotes bathymetry. Adapted from Tesdal and Haine (2020).

1.3. Sources and Export of Deep Water

Water in the boundary current cools as it travels downstream by releasing heat to the atmosphere. It also freshens by fresh water fluxes of precipitation and inflow of meltwater. Also in the interiors of the Irminger Sea and Labrador Sea strong winter cooling takes place which enables deep convection. Buoyant surface layers loose heat and get denser. If the surface layers become denser than the lower layers, the water column gets unstable, vertical mixing takes place and dense deep water is formed. These waters are exported from the SPNA via interior pathways and by the boundary current via boundary current-interior exchange (Lozier, 2023 and references there in; Brüggemann and Katsman, 2019; Georgiou et al., 2021; Le Bras et al., 2020).

In addition to these locally formed deep waters, a second—source of deep water is formed in the Nordic Seas and enters the region across the Greenland–Scotland Ridge as overflow water. Iceland–Scotland Overflow Water (ISOW) enters the SPNA through the Faroe–Bank Channel (Hansen et al., 2016), while Denmark Strait Overflow Water (DSOW) crosses the ridge via the Denmark Strait (Jochumsen et al., 2017).

The overflow waters formed in the Nordic Seas are a second source of deep water that enters the SPNA by crossing the GSR as visualised in Figure 1.3. Iceland Scotland Overflow Water (ISOW) enters the SPNA via the Faroe-Bank Channel (Hansen et al., 2016) and Denmark Strait Overflow Water (DSOW) enters the SPNA via the Denmark Strait (Jochumsen et al., 2017). These dense deep waters merge together in the Irminger Sea and form the main contributor to the deep southward limb of the AMOC (Xu et al., 2010; Lozier et al., 2022; Pratt and Whitehead, 2008; Østerhus et al., 2019). This deep water is exported from the SPNA via the Deep Western Boundary Current (DWBC) (flowing below the WGC and LC in Figure 1.3), as well as via the interior (Lozier et al., 2022; Bower et al., 2009).

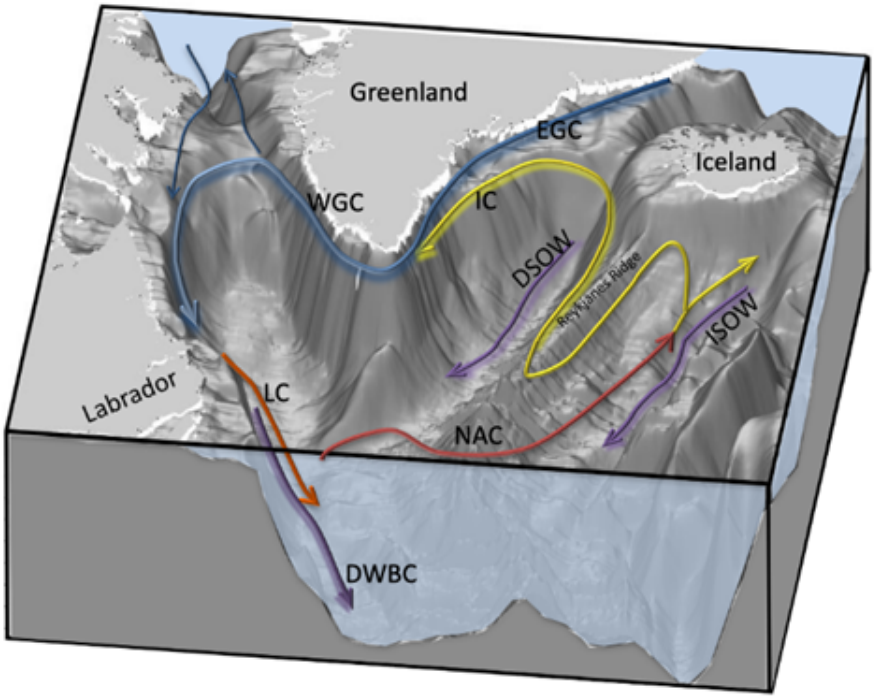

Figure 1.3: View of the subpolar North Atlantic with a schematic of the circulation compiled from ETOPO1 data (Amante & Eakins, 2009). It shows surface currents as well as the deep ISOW, DSOW and DWBC. NAC: North Atlantic Current, IC: Irminger Current, EGC and WGC: East and West Greenland Current, LC: Labrador Current, DSOW: Denmark Strait Overflow Water, ISOW: Iceland Scotland Overflow Water and DWBC: Deep Western Boundary Current. Schematic copied from Georgiou (2021).

1.4. Restratification of the Interior

Eddies play an important role in establishing boundary current-interior exchange for both exporting deep water from the interior to the boundary current as well as for restratification of the interiors of both the Irminger Sea and the Labrador Sea. Eddies in the Irminger Sea result mainly from baroclinic instabilities in the boundary current, have an average radius of 6 km and maximum velocity of 0.1 m s^{-1} (Fan et al., 2013). They are warm core eddies, indicating that they originate from the IC (Sterl & de Jong, 2022) and transport warm and saline water into the Irminger Sea interior. They peak in summer and help to restore the heat lost during winter (Fan et al., 2013). At the surface there is fresh water inflow due to water being driven off the Greenland shelf during strong wind events (Duyck et al., 2022).

In the Labrador Sea there are three types of eddies originating from both baroclinic and barotropic instabilities (Lilly et al., 2003; Katsman et al., 2004; Gelderloos et al., 2011; Rieck et al., 2019). Convective eddies and boundary current eddies develop from baroclinic instabilities in the boundary current and are the most important for boundary current-interior exchange according to Rieck et al. (2019). Their average radius ranges between 5 and 18 km with maximum velocity of 0.1 – 0.3 m s^{-1} (Katsman et al., 2004; Rieck et al., 2019). A third type of eddies are the Irminger Rings (IRs). They have an average radius between 15 and 30 km and maximum velocity of 0.3 – 0.8 m s^{-1} (Katsman et al., 2004; Gelderloos et al., 2011). The eddies have a warm and saline core topped by a colder and fresher core at the surface which is related to the structure of the WGC (Hátún et al., 2007; de Jong et al., 2014). IRs form from barotropic instabilities in the WGC as it encounters a steepening in the topographic slope. According to Katsman et al. (2004) and Gelderloos et al. (2011) IRs have the largest contribution in boundary current-interior exchange. All three types of eddies peak in winter and replenish heat (Katsman et al., 2004; Rieck et al., 2019)

1.5. Denmark Strait and its Overflow

Denmark Strait (DS) is the strait between Greenland and Iceland and part of the GSR, which separates the Nordic Seas from the SPNA. DS has a shallow sill with a maximum depth of 650 m and the part that is deeper than 350 m is only about 60 km wide (Whitehead, 1989b; Østerhus et al., 2019). When water flows across this sill, the flow is hydraulically controlled and is referred to as the Denmark Strait Overflow (DSO).The transport and velocity of the overflow are determined by the upstream density difference and the height of the sill. According to the Bernoulli Principle the pressure at the sill reduces, the flow accelerates and it reaches a critical state, characterised by a Froude number of 1. The Froude number is defined as: $Fr = \frac{U}{\sqrt{g'H}} = 1$, where U is the flow velocity, H the layer thickness, and g' the reduced gravity. It quantifies the ratio between the flow speed and internal-wave speed and thus determines whether upstream communication is possible. Upstream of the sill, the flow is subcritical ($Fr < 1$) and can adjust to signals such as changes in density or forcing, while downstream it becomes supercritical ($Fr > 1$), isolating the upstream reservoir from downstream signals. As the overflow descends into the Irminger Basin, it entrains ambient water, slows down, and eventually returns back to subcritical conditions through an internal hydraulic jump. This transition dissipates kinetic energy and enhances mixing, further modifying the properties of the overflow. This hydraulic control constrains the overflow transport to a maximum determined by the upstream density difference and sill depth, independent of downstream variability (Whitehead et al., 1974; Whitehead, 1989a; Pratt and Whitehead, 2008).

Denmark Strait Overflow Water (DSOW) refers to the dense water mass carried by the overflow, typically defined as water with potential density $\sigma = \rho - 1000 > 27.8$ kg/m^3 at the sill (Dickson and Brown, 1994; Koszalka et al., 2013; Jochumsen et al., 2017; Saberi et al., 2020). The overflow originates from the north via the East Greenland Current, the separated East Greenland Current and the North Icelandic Jet (Saberi et al., 2020; Behrens et al., 2017). The North Icelandic Jet is partly feeded by the North Icelandic Irminger Current flowing along the Iceland shelf to the north and then bending into the North Icelandic Jet. This contribution is only seen in February, March, April and May and is likely to vary interannually depending on the local surface forcings (Saberi et al., 2020). About half of the overflow cascades over the sill into the Irminger Sea (Koszalka et al., 2013), from where it is transported southward along the deep boundary current and into the interior before rounding Cape Farewell and entering the Labrador Sea, where it spreads further along the boundary current and into the basin interior (Lozier et al., 2022). The other half of the overflow recirculates on the Dohrn Bank, a topographic rise between the sill and the Kangerlussuaq Trough along the coast of Greenland, and around the Kangerlussuaq Trough before it cascades off the shelf and rejoins the overflow after 1 to 3 weeks (Koszalka et al., 2013). Upon entering the Subpolar North Atlantic, the overflow experiences mixing that rapidly decreases its density in the first 200 km from the sill (Koszalka et al., 2013).

1.6. Impacts of Climate Change on the AMOC

Climate change is an urgent issue which has a lot of environmental, social and economic implications (Tol, 2018; Abbass et al., 2022). DSOW formation and the AMOC are also affected by climate change. As described above, the AMOC has two stable regimes, the thermo- and the haline-regime of which to date the thermo-regime is dominant (Stommel, 1961; Weijer et al., 2019; Rahmstorf, 2024). Due to polar amplification the polar regions warm more than the (sub)tropical regions (Previdi et al., 2021). At the same time, an enhanced hydrological cycle freshens polar and subpolar water by increased precipitation and ice melt, while subtropical waters become more saline due to enhanced evaporation (Collins et al., 2013; Held and Soden, 2006). The fresh water from glacier and ice melt could form a buoyant cap over the SPNA and Nordic Seas, reducing winter cooling in the more saline subsurface layers and decrease deep convection. As a results, less dense water is formed and available to feed DSOW, weakening the lower limb of the thermo-regime of the AMOC. Together with an increased salinity gradient between high and low latitudes, these changes can affect the stability of the AMOC and push it closer to the tipping point between a thermo-dominant AMOC and haline-dominant AMOC (Stommel, 1961; Weijer et al., 2019; Rahmstorf, 2024).

As the AMOC weakens it will transport less water from the tropics to the subpolar and polar regions. The change in ocean heat transport and sea surface temperature (SST) this causes, would have massive implications for climate and weather worldwide (van Westen et al., 2024; Ma et al., 2024). According to the IPCC, changes in the subpolar gyre circulation and AMOC result in a reduced northward heat trans-

port by the ocean, and hence a lowering of the SST mostly North Atlantic north of 50° N (Fox-Kemper et al., 2021). Although there is significant uncertainty in the precise magnitude of the responses, the overall direction of the changes is likely robust. Under a severely weakened AMOC, lower SSTs and a redistribution of heat result in lower atmospheric temperatures in the Northern Hemisphere (NH), specifically very strong winter cooling of up to 3.5 °C per decade in north-western Europe, and warming in the Southern Hemisphere (SH) as can be seen in Figure 1.4a. The Arctic sea-ice pack is expanding down to 50° N in March, which further amplifies Northern Hemispheric cooling by reflecting more incoming radiation back to space via the ice-albedo feedback, while the Antarctic sea-ice pack is retreating. In the NH a stronger meridional temperature gradient strengthens the Hadley cell and the subtropical jet stream, while in the SH the opposite would happen. Due to a redistribution of heat, the thermal equator shifts southward and hence also the intertropical convergence zone (ITCZ) will shift southward and precipitation patterns will change. As can be seen in Figure 1.4b precipitation in the SH increases and decreases in most of the NH, especially around the equator and in northwestern Europe. It switches around the dry and wet season in the Amazon and has major effects on the monsoon in West Africa and India because less moist air reaches these regions. North of 40° N, a significant sea level rise is expected, related to changes in the SPG and STG. In the present-day circulation, the SPG corresponds to a region of relatively low sea level (a low-pressure area), while the STG is associated with high sea level. When the AMOC weakens, the density and pressure gradients in the North Atlantic change and the geostrophic balance is disturbed. As the circulation readjusts to weaker pressure gradients, the low-pressure anomaly in the SPG becomes less pronounced, leading to a regional sea level rise north of 40° N (van Westen et al., 2024; Chafik and Rossby, 2019; Fox-Kemper et al., 2021; Ma et al., 2024).

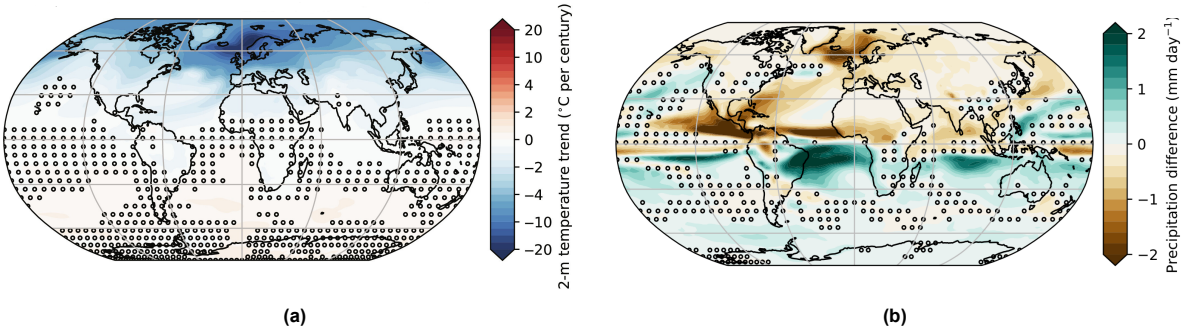

Figure 1.4: Changes in **(a)** global temperature and **(b)** global precipitation. The markers indicate nonsignificant trends. Copied from van Westen et al. (2024).

1.7. Research Questions

Although timing and magnitude are uncertain, a weakening of the AMOC in the 21st century is very likely according to the IPCC (Fox-Kemper et al., 2021) and a recent study by van Westen et al. (2025). Pathways of dense water within the Labrador Sea are extensively studied in Georgiou et al. (2021). However, pathways of DSOW within the Irminger Sea and a possible connection between the two basins is less well known and there is no consensus yet on which percentage of water follows which path. Recent studies have shown that much more overturning takes place in the eastern SPNA than in the Labrador Sea, emphasizing the importance of the Irminger Sea for the AMOC (Lozier, 2023). DSOW, which enters the SPNA in the Irminger Sea, is very cold and dense, contributing significantly to the lower limb of the AMOC. Gaining a better understanding of the current behaviour of DSOW, on the partitioning of DSOW between pathways in the SPNA via the boundary current and interiors and on the density, temperature and salinity of the water along the pathways forms the focus of this thesis.

What are main pathways via which Denmark Strait Overflow Water spreads within the subpolar North Atlantic and how do water properties change along these pathways?

To answer the main research question, the following subquestions are defined:

- Which pathways can be identified and what percentage of DSOW particles follows each pathway?
- How do DSOW density, temperature and salinity evolve as it travels down the pathways?

2

Methodology

2.1. Copernicus Marine Data

For this thesis we used data from the Global Ocean Physics Analysis and Forecast (GLOPAF) (Copernicus Marine Service, 2025, Galloudec et al., 2025). It is provided by Copernicus Marine Environment Monitoring Service (CMEMS) or short Copernicus Marine Service and uses the NEMO 3.6 numerical ocean model (Gurvan et al., 2017). GLOPAF has 1/12° spatial resolution with 50 depth layers from 0 to 5500m depth. It outputs, among others, 3D data on u-, v-, and w-velocity, on potential temperature and on salinity. Here 3D means that the variables have dimensions latitude, longitude and depth. For these variables we use daily mean values from the first available day, 01-06-2022 up until 31-05-2025. The bathymetry used by GLOPAF is a combination of GEBCO8 data for the upper 200m, ETOPO1 data below 300m and a linear interpolation between 200 and 300m depth. GLOPAF does not output density, hence we calculated it from the other available variables using TEOS-10 via the Gibbs-SeaWater (GSW) Oceanographic Toolbox (McDougall & Barker, 2011).

GLOPAF includes atmospheric forcings that influence the oceans and the currents, such as fresh water fluxes, heat and wind, from ECMWF IFS HRES (European Centre for Medium-Range Weather Forecasts Integrated Forecast System analyses and forecasts with High spatial and temporal Resolution) (ECMWF, n.d.). Monthly run-off from the 100 major rivers from Dai et al. (2009) and run-off fluxes from Greenland and Antarctica are also included. The effect of sea ice is also included via the LIM3 sea ice model, a model with different categories of sea ice able to represent unresolved subgrid-scale variations in ice thickness (Vancoppenolle et al., 2012).

GLOPAF is accurate when compared with observations (Lellouche et al., 2025). The ocean water masses are very accurate on average with very weak biases of 0.05 °C and 0.02 psu at the surface. For a reference temperature of 2.0 °C and practical salinity of 34.9 g/kg (Jochumsen et al., 2015; Tanhua et al., 2005) this bias in temperature would result in a change in density of 0.004 kg/m^3 and the bias in salinity would result in a change in density of 0.016 kg/m^3. The temperature and salinity are both well represented except for regions with high spatial and temporal variability such as Western Boundary Currents and the Arctic marginal seas during melt season, where the output is too salty and too warm; the sea surface temperature is very close to observations. This could impact our analysis as Arctic water, which is a source for DSOW, is represented too warm and salty by the model. The currents at 100 m depth are properly estimated in both magnitude and direction; about the accuracy of deeper currents nothing is stated.

2.2. Tracking Denmark Strait Overflow Water

To track where in the Subpolar North Atlantic (SPNA) Denmark Strait Overflow Water (DSOW) spreads, we perform a Lagrangian particle tracking simulation using the OceanParcles software from Delandmeter and van Sebille (2019). We seed the particles that we want to track along a transect in the Denmark Strait and track them for three years, from 01-06-2022 (the first day the data is available) up until 31-05-2025.

2.2.1. Selecting Transect

The red line in Figure 2.1a is the location of the transect. We define the location of the transect using both literature and bathymetry. Based on literature the transect starts at Latrabjarg, the most western point of Iceland, and is oriented to the north-west; this part contains the sill of DS that is the deepest part of the transect of 644m and a small part of the shelf. After arriving at the shelf, we choose to change the orientation of the transect to the north in order to avoid the Kangerlussuaq Trough and other unevenness in the bathymetry. By visual inspection we ensure that the bathymetry of the north oriented part of the transect is relatively smooth. Figure 2.1b shows a cross-section of the bathymetry of the transect looking at it from the south-west with the East Greenland coast on the left and Latrabjarg on the right. The dashed black line at 205 km separates the East Greenland shelf on the left from the sill in DS and the Iceland shelf on the right. The Iceland shelf starts from Latrabjarg and ends where the bathymetry steepens around 90 km distance along the transect. We choose this separation based on a study by Koszalka et al. (2013) where they used the same location for the shelf break to split the east Greenland shelf from the DS sill.

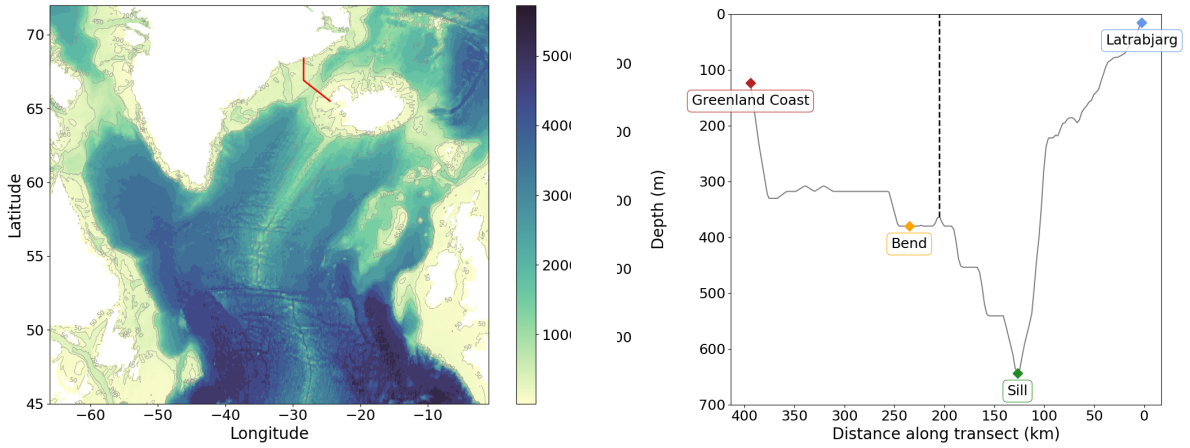

Figure 2.1: (a) The transect at Denmark Strait in red. The shading shows the ocean bathymetry from GLOPAF. **(b)** The bathymetry with distance along the transect. Latrabjarg is marked in blue, the sill at 127 km is marked in green, the bend in the transect at 235 km is marked in orange and the east coast of Greenland at 394 km is marked in dark red. The dashed black line at 205 km separates the east Greenland shelf on the left from the sill and Iceland shelf on the right. The Iceland shelf starts at Latrabjarg and ends where the bathynetry steepens around 90 km distance along the transect.

Hydrographic sections of the Copernicus Marine data used along the transect averaged per season are shown in Figure 2.2. Here we define spring as March/April/May, summer as June/July/August, autumn as September/October/November and winter as December/January/February. Hydrographic sections of potential density are shown in Figure 2.2a, 2.2b shows velocity orthogonal to the section, 2.2c shows potential temperature and2.2d shows practical salinity interpolated along the transect. Overlying in dashed are the isopycnals with the 27.8 kg/m^3 isopycnal highlighted in solid.

The clearest seasonal differences are in the surface layer on the Greenland shelf. Density is lowest in winter and spring (σ = 25.5 – 26.7 kg/m^3) and highest in summer and autumn (σ = 25.8 – 27.3 kg/m^3); velocities peak in spring (0.15 m/s magnitude) and are weakest in autumn (0.09 m/s magnitude); temperatures are lowest in winter and spring (T = -2.0 – -0.8 °C) and highest in summer and autumn (T = -1.2 – 0.4 °C); and salinity is lowest in winter and spring (S = 31.8 – 32.6 kg/m) and highest in summer (S = 33.8 – 34.6 kg/m), already decreasing again in autumn (S = 32.2 – 33.8 g/kg). Bacon et al. (2014) found that freshwater transport reaches a maximum in February and a minimum in August, while Le Bras et al. (2018) found a maximum freshwater transport in late fall and winter. The seasonality in the hydrographic sections is generally in line with what is described in the literature, although the precise timing differs. The timing of lowest salinity water on the shelf in winter and spring does not align with the freshwater inflow from seasonal melt of glaciers and sea ice which peaks in August (Le Bras et al., 2018). ”This may be due to delays in export from glaciers to fjords to the shelf, control by wind-driven transport divergence on the shelf, or dominance of Arctic origin freshwater” (Le Bras et al., 2020).

We are however, most interested in what happens below the 27.8 kg/m^3 isopycnal at the sill because this is where DSOW is located. The densest water is found in summer and spring where also the isopycnals are shallowest. In summer the isopycnal on the sill is located around 150 m depth and is shallower than in autumn when its around 220 m depth while on the shelf the depth of the isopycnal is around 220 m for summer and autumn. Hence in autumn there is relatively more dense water on the shelf compared to the sill than in summer. In total there is most dense water in summer. In winter and spring the isopycnal above the shelf is at comparable depth between 240 and 270 m while above the sill the isopycnal in spring is around 200 m depth and is shallower than in winter when it is around 230 m depth. This means that in winter there is the smaller amount of dense water than in spring. Velocities on the sill are toward the south-west (negative, blue) and the core with highest velocity (0.27 – 0.42 in magnitude) is bigger in summer and autumn; the temperature is coldest in summer and autumn (T = -1.6 – -0.4 °C) and warmest in winter and spring (T = -0.4 – 0.8 °C); the most saline water on the sill is in summer (S = 35.0 – 35.2 g/kg), autumn is the freshest water (S = 34.6 – 35.0 g/kg) and winter and spring are in between (S = 34.8 – 35.0 g/kg). This observed seasonal variability could be linked to the passage of boluses and pulses over the sill in DS (Almansi et al., 2017). A bolus, first introduced by Cooper (1955) refers to a large lens of cold, weakly stratified overflow water that crosses the strait. The term pulse was introduced by Bruce (1995) and describes an intermittent increase in bottom velocity in the strait corresponding to a thinning and acceleration of the DSOW layer (von Appen et al., 2017). Both the boluses and pulses result in increased transport of DSOW over a period of several days. Boluses have an average duration of 57.1 hours, occur every 3.2 days and are most frequent in summer; pulses are 27.5 hours long, occur every 5.5 days and are most frequent during winter (von Appen et al., 2017; Almansi et al., 2017).

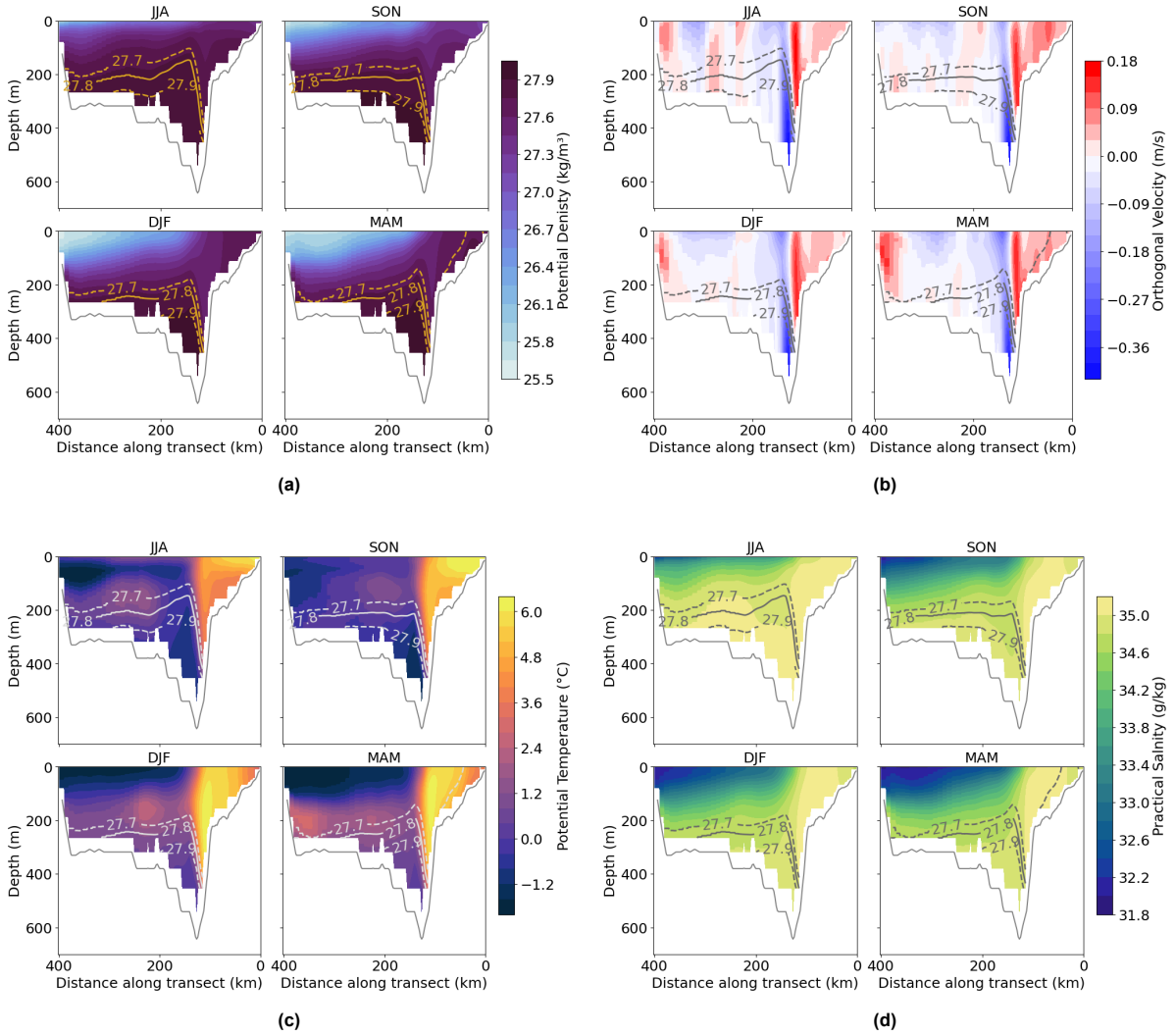

Figure 2.2: Hydrographic sections of seasonal averages of the GLOPAF data of (**a**) potential density, (**b**) orthogonal velocity, (**c**) potential temperature and (**d**) practical salinity along the transect. Dashed are the isopycnals with the 27.8 kg/m^3 isopycnal solid.

Since DSOW is hydraulically controlled we expect little seasonal and inter-annual variability in the volume of the overflow (Girton & Sanford, 2003). However, in the hydrographic sections above we do observe seasonal variability in isopycnal depth, temperature, salinity and velocity. We nevertheless choose to use the GLOPAF data, as previous studies have described mechanisms that can introduce seasonal variability in DSOW, such as boluses and pulses (Almansi et al., 2017; von Appen et al., 2017). Moreover, the model has fine resolution allowing to resolve small scale patterns, it has vertical velocity which is important when analysing overflow water and it is accurate when compared with observations according to Lellouche et al. (2025). This agreement with observations is consistent with our findings as well, as both the structure of the hydrographic sections and the DSOW transport display similar patterns and magnitude when compared with observations. In literature the estimated DSOW transport varies between 3.18 and 3.54 Sv (Jochumsen et al., 2012; Jochumsen et al., 2017; Lin et al., 2020). The calculated average transport of water denser than 27.8 kg/m^3 is 1.98 Sv which is smaller but in the same order of magnitude as the transport of DSOW in literature. Comparing the model's hydrographic sections to observational hydrographic sections from Mastropole et al. (2017), we see the warm and saline water on the Iceland shelf although the temperature is not as high in the model (T = 4.0 – 5.8 ° C) as in the observations (T = 7.0 – 8.0 °C). The cold and fresh Arctic-water at the surface at the western side of the section is also present. The model has temperature here between -1.8 and 0.0 °C and salinity between 33.8 and 34.6 g/kg, and the observations have temperatures between 1.5 and 2.5 °C

ans salinity between 31.0 and 34.6 g/kg. On the sill the model data shows the densest water with low temperatures between -1.2 and -0.4 °C and high salinity between 35.0 – 35.2 g/kg. The observations also show the densest water on the sill with temperature between 0.0 and 1.5 °C and salinity between 34.8 and 34.9 g/kg. According to Lellouche et al. (2025) the model represents the Arctic marginal seas too warm and salty during melt season. This may be seen in two ways in the hydrographic sections since Arctic-origin water is located at the western side of the transect on the Greenland shelf and it is a source of deep water that feeds DSOW. However for both locations we observe the model to be colder than the observations. We do see slightly more saline water in the model than in the observations; on the sill the model is about 0.2 g/kg more saline and on the east Greenland shelf the range in salinity to low values is much smaller. The depth of the 27.8 isopycnal in the model and in observations is comparable over the Greenland shelf, both are at a depth around 250 m. On the sill however the model isopycnal is shallower than in the observations; its minimum depth is slightly less than 200 m and it goes down to 400 m while the observed isopycnal is always deeper than 250 m with a maximum depth of 430 m. This can be related to the fact that the models has colder and slightly more saline water on the sill than the observations which result in denser water in the model than in the observations. In summary, the model reproduces the main hydrographic patterns associated with the IC, EGC, EGCC, and the dense overflow. However it has lower temperature and higher salinity which, especially on the sill, results in a shallower 27.8 isopycnal in the model than inferred from observations.

2.2.2. Release Moments and Release Points

To capture the seasonal variability evident in the hydrographic sections, we release particles at the beginning of each season. In addition, short-term variability of 2 – 5 days in velocity and layer thickness (Girton & Sanford, 2003), as well as 3 – 5 day variability in transport (Saberi et al., 2020), leads us to release particles over multiple consecutive days. We release particles during the first five days of each month, resulting in releases from 1–5 June ‘22, September ‘22, December ‘22, and March ‘23.

Following earlier Lagrangian studies of the Denmark Strait Overflow and the subpolar North Atlantic (Koszalka et al., 2013, Saberi et al., 2020, Georgiou et al., 2021), we choose a horizontal particle spacing of 500 m and a vertical spacing of 25 m. This resolution captures the horizontal and vertical structure of the overflow and boundary current, while remaining computationally efficient. In literature DSOW is defined as water with a potential density of 27.8 kg/m^3 or higher. Model isopycnals do not always agree with isopycnals from observations; hence we chose to track all particles with a potential density of 27.7 kg/m^3 and higher at the DS sill. To determine the density of every point, we used linear interpolation to interpolate the density from the tracer field onto the seeding points. Figure 2.3 shows in the background in light blue all possible seeding points defined by the 500 m horizontal and 25 m vertical spacing. The red points are the sum of the selected seeding points of all five days for June ‘22 (Figure 2.3a), September ‘22 (Figure 2.3b), December ‘22 (Figure 2.3c) and March ‘23 (Figure 2.3d). This means that a point is coloured red if its density is 27.7 kg/m^3 or higher for at least one of the five days. All particles located to the left of the dashed black line are on the shelf, corresponding to 27% in June ‘22, 41% in September ‘22, 19% in December ‘22 and 22% in March ‘23. Over all four seasons together 45519 particles are seeded in total, of which 13643 in June ‘22, 14323 in September ‘22, 8370 in December ‘22 and 9183 in March ‘23. Note that we seed most particles in June ‘22 where the isopycnal in Figure 2.2a is shallowest; that in September ‘22 a big part (41%) of the particles is seeded on the shelf; and that in March 12% of the particles is seeded on the Iceland shelf. According to Saberi et al. (2020) and Behrens et al. (2017) the particles on the Iceland shelf cross the GSR with the NIIC and can become part of the overflow by returning south with the NIJ.

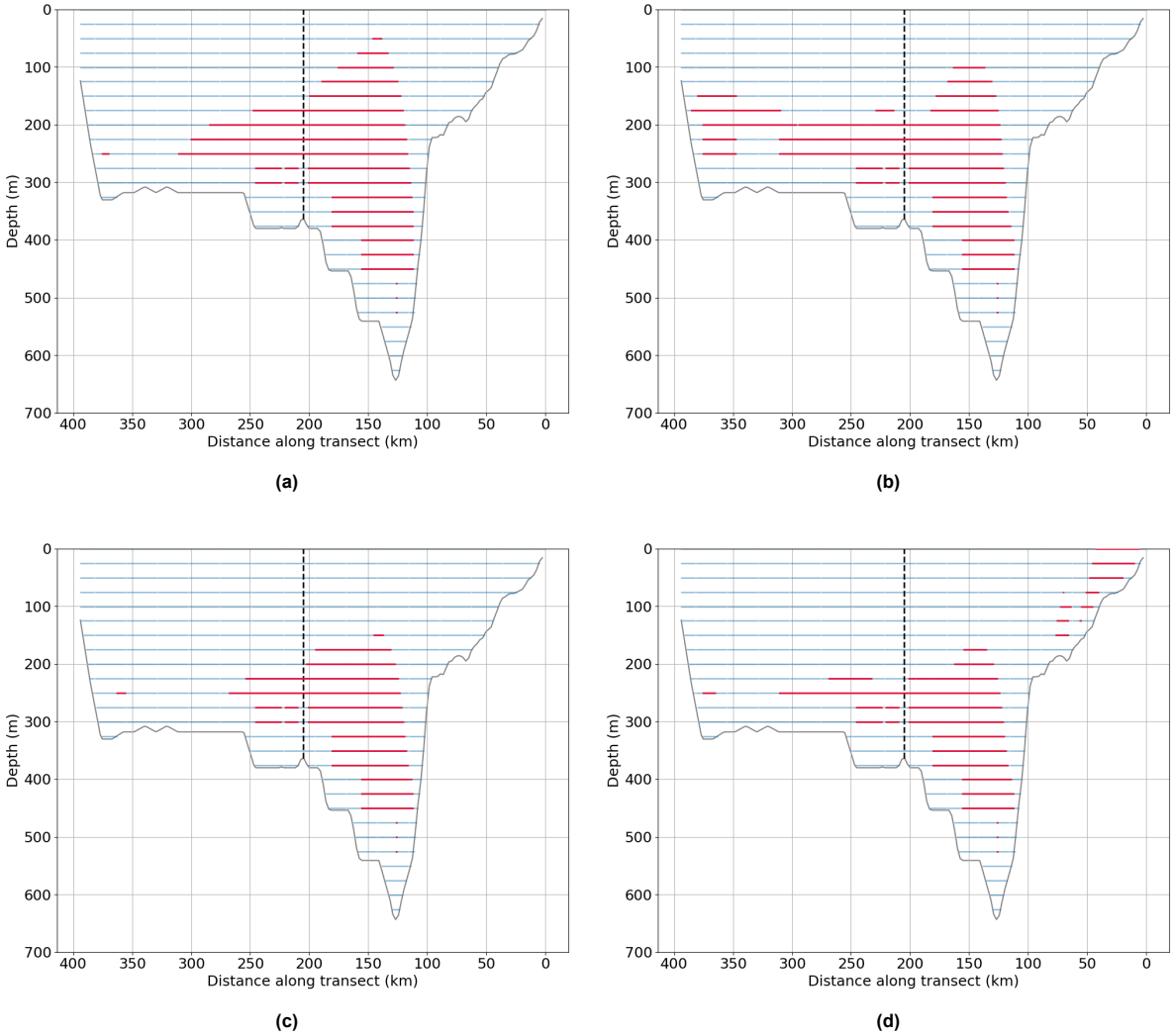

Figure 2.3: Selected seeding points per season. In the background in light blue are all possible seeding points defined by the 500 m horizontal and 25 m vertical spacing. The red points are the sum of the selected seeding points of all five days together for (**a**) June ‘22, (**b**) September ‘22, (**c**) December ‘22 and (**d**) March ‘23. The dashed black line at 205 km separates the east Greenland shelf on the left from the sill and Iceland shelf on the right.

2.2.3. Running Simulation, Defining Kernels

In order to run the simulation, we first defined kernels and interpolation methods to determine the behaviour of the particles during the simulation. We used the ‘AdvectionRK4_3D’ kernel included in Parcels, which applies a fourth-order Runge–Kutta integration and offers a good balance between numerical accuracy and computational cost. We wrote kernels ourselves to keep track of a particle’s temperature, salinity, density and velocity along the path and to avoid errors when a particle is going out of the domain or out of the ocean. For u- and v-velocity we used the free slip interpolation method to avoid particles from getting stuck on bathymetry. When using the free slip interpolation method “the tangential velocity is constant in the direction normal to the boundary” according to OceanParcels (2025b). This means that a particle slides along the bathymetry without feeling resistance. For w-velocity, temperature, salinity and density we used linear interpolation.

2.3. Processing Simulation Output

2.3.1. Selecting Particles for the Analysis

Taking a first look at the particle trajectories, the particles fill the entire SPNA and also the Iceland Sea north of Iceland. We want to continue the analysis only with particles that flow southward into the SPNA and not the particles that go north into the Iceland Sea. We define a particle to not be part of our analysis

if, at the end of the three year simulation, its final position is to the north-east of the transect and it did not cross the zonal section at 64.5° N between Greenland and Iceland (the blue line in Figure 2.4) from north to south. All the other particles are part of our analysis. When selecting the latitude of the zonal section, we took several aspects into account. Some particles first go to the south-east of the transect, circulate around the Kangerlussuaq Trough or in eddies and then go to the north of Iceland. To avoid these particles crossing the zonal section, we selected it sufficiently far south of the transect. We also notice particles that go to the north of the transect, all the way around Iceland in clockwise direction until the Reykjanes Ridge. In order to avoid these particles becoming part of our analysis, we selected the zonal section north of the Reykjanes Ridge.

This results in 87% of the released particles (39765 from total 45519 particles) to be part of our analysis. Figure 2.4a shows the trajectories of particles part of our analysis with the transect in red and the zonal section in blue; Figure 2.4b shows the trajectories of the particles that are not part of our analysis. One can see that particles part of our analysis fill up the SPNA and that a part first goes to the north-east of the transect before returning back to cross the GSR via DS. Seven particles circulate clockwise around Iceland and enter the SPNA between Iceland and Great Britain. Although they are not part of DSOW, they are part of our analysis because their final position is not to the north of the transect. Since these particles only account for 0.02% of all particles in our analysis, their influence on the results is negligible. These trajectories could be filter out of our analysis by an extra selection criterion based on where particles enter the SPNA for example. For the particles not part of our analysis, one can see that a part goes to the south-west of the transect and then goes back to the north/north-east of Iceland.

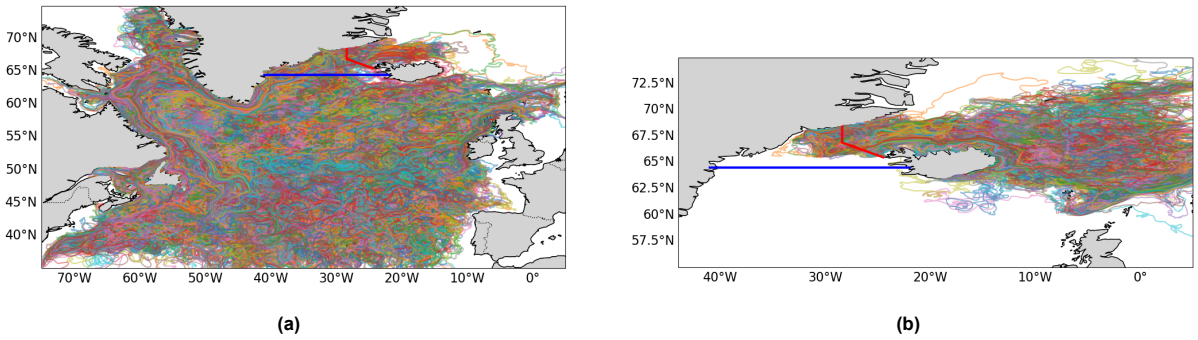

Figure 2.4: Particle trajectories of **(a)** particles that are part of our analysis and **(b)** particles that are not part of our analysis. In red is the transect and in blue is the zonal section at 64.5° N. Particles are excluded from our analysis if their final position is to the north-east of the transect and they did not cross the zonal line. The zonal section is selected based on observed particle trajectories. More details on how we selected this zonal section are described in subsection 2.3.1.

2.3.2. Removing Stationary Particles

Although we defined the free slip interpolation method for u- and v-velocity, particles still get stuck at the bathymetry. The fraction of moving particles over time is shown in Figure 2.5a for each of the four months in which we release particles. The first five days of every month the fraction of moving particles increases. Then the fraction decreases rapidly at first and more slowly afterward. For the particles seeded in June, after about one month 30% of the particles have stopped moving and after four to five months half of the particles has stopped. In September this decrease is less fast. Here, around 10% of the particles gets stuck in the first month and half of particles after eight months. For particles released in December and March about 20% gets stuck in the first month. After six to seven months half of the particles released in December stopped moving. For March this takes about seven months.

Figure 2.5b shows the percentage of particles that get stuck at a certain location. It can be seen that particles mainly get stuck in areas with shallow bathymetry around Greenland, along the Labrador coast and near the Grand Banks. The highest percentage of particles get stuck at the Greenland shelf, especially at the eastern shelf. When a particle gets stuck, its latitude, longitude, and depth no longer change, and its temperature and salinity drop to zero. To prevent these non-physical values from biasing the results, we retain only the parts of each trajectory where the particle is still moving. This ensures physically meaningful and interpretable results. A particle is considered stuck if the difference

between consecutive timesteps in latitude, longitude, and depth is smaller than 1e-6 or if the difference in temperature and salinity remains smaller than 1e-6 for five days in a row. The non-moving part is then removed using the bisection method.

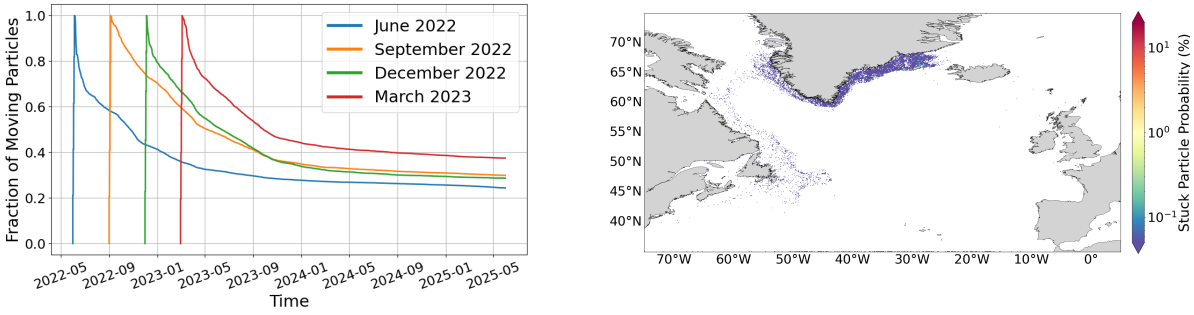

(a) **(b)**

Figure 2.5: **(a)** Fraction of moving particles over time per month of release. **(b)** Concentration of particles that get stuck at a certain location.

2.4. Analysing the Output

2.4.1. Particle Concentration Maps

Particle concentration maps are helpful when analysing main pathways of particles. To create them, we divide the SPNA in a $0.1° \times 0.1°$ (latitude, longitude)-grid. This resolution is detailed enough to show the main features and smaller pathways, but not so fine that the maps become noisy or patchy. The chosen resolution is also in line with a previous Lagrangian study by Georgiou et al. (2021). For every grid cell we count how many particles pass through this grid cell over all times. Dividing by the total number of particles this gives a percentage of particles passing through a grid cell. Note that we only considered the presence of a particle in a grid cell, not how many times the particle enters the cell. The approach we chose highlights the main pathways and spatial distribution of particles, rather than regions where particles recirculate such as troughs.

We make particle concentration maps for all particles together, as well as for only the dense (denser than 27.8 kg/m^3 at the moment of seeding at DS) and intermediate dense (between 27.7 and 27.8 kg/m^3 at the moment of seeding at DS) particles, all as a percentage of all particles.

2.4.2. Categorising Particles into Regions

Besides particle concentration maps, it is helpful to categorise particles based on where in the SPNA they go. Therefore, we defined four regions:

1. Boundary current (BC);
2. Irminger Sea interior (IrS);
3. Labrador Sea interior (LS); and
4. Iceland Basin interior (IcB).

To divide particles between boundary current and interior we chose the -22 Sv barotropic streamline as boundary. Figure 2.6a shows the particle concentration map for all particles with -22 Sv streamline dashed in black. The -22 Sv streamline is located where the particle concentration towards the interior is decreasing. This decrease in particle concentration marks the transition from the coherent boundary current to the more diffuse interior. The same particle concentration map with barotropic streamline zoomed in on the east Greenland coast, the west Greenland coast, and the coast of Newfoundland is shown in Figures 2.6b, 2.6c and 2.6d respectively. At the east Greenland coast the -22 Sv streamline clearly contains the entire boundary current; at the west Greenland coast it is on the edge of the boundary current and at the coast of Newfoundland a small part of the boundary current is cut off. This is a consequence of the volume transport in the boundary current that increases as it flows downstream because of extra inflow of water into the boundary current. If a particle stays offshore (inside) of the

-22 Sv barotropic streamline for at least 20 consecutive days, we consider that particle a interior particle; otherwise it is considered a boundary current particle. We chose 20 consecutive days to filter out possible short and fast excursions of particles into an interior.

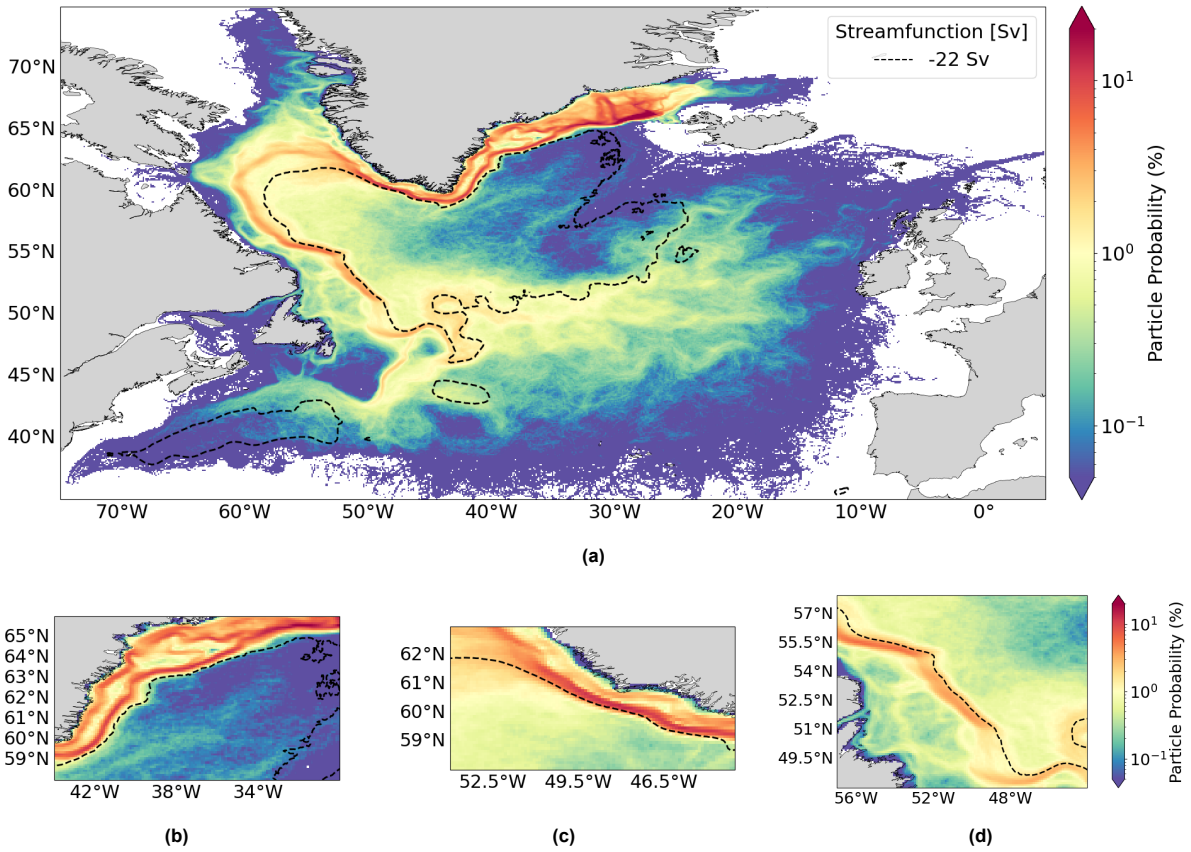

Figure 2.6: Particle concentration map for all particles with dashed the -22 Sv barotropic streamline. **(a)** Shows the entire region, **(b)** is zoomed in on the east Greenland coast, **(c)** on the west Greenland coast and **(d)** on the coast of Newfoundland.

The -22 Sv barotropic streamline makes a closed region. We split this region into three different interiors. As border between the Labrador Sea and the Irminger Sea we chose a meridional line at Cape Farewell at 44° W. As border between the Irminger Sea and the Iceland Basin we choose the Reykjanes Ridge based on the geographical coordinates of Marine Regions (n.d.) extended to keep following the bathymetry of the ridge. This gives the regions shown in Figure 2.7. We use spline interpolation to smooth the southern and northeastern part of the streamline in the Irminger Sea to make a smooth boundary that does not include the standing eddies at the southern part of the Irminger Sea and the irregularities in the north-east.

We classify particles into one of the three interiors depending on which interior they enter first. If for example a particle first enters the Irminger Sea interior and later the Labrador Sea interior, we consider it an Irminger Sea particle. This gives the following four categories of particles:

- Boundary Current (BC) particles: particles that stay onshore of the smoothened -22 Sv barotropic streamline;
- Irminger Sea (IrS) particles: particles that enter the Irminger Sea as first interior for at least 20 consecutive days;
- Labrador Sea (LS) particles: particles that enter the Labrador Sea as first interior for at least 20 consecutive days;
- Iceland Basin (IcB) particles: particles that enter the Iceland Basin as first interior for at least 20 consecutive days.

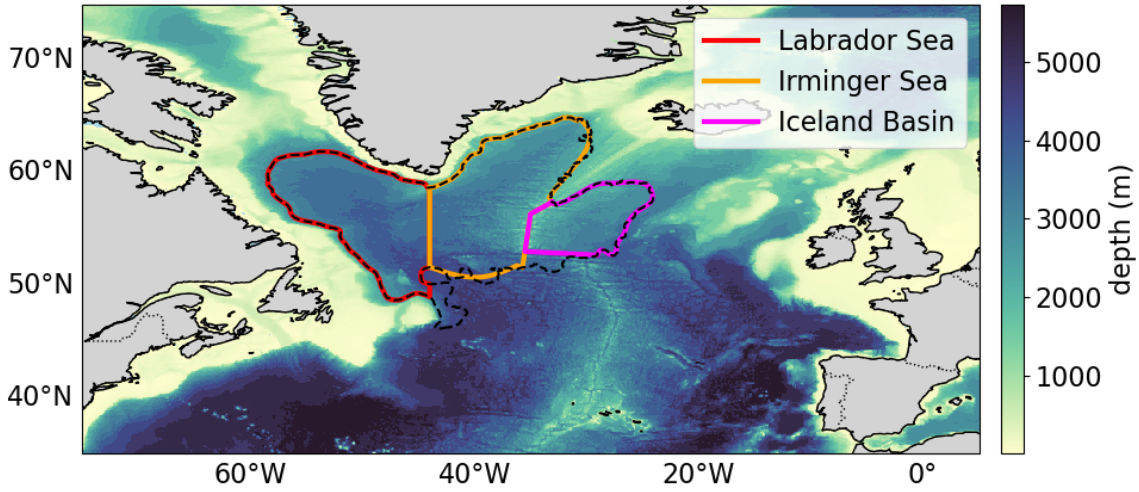

Figure 2.7: Definition of boundary current and interior regions. In red the Labrador Sea interior, in orange the Irminger Sea interior and in magenta the Iceland Basin interior. Dashed in black is the -22 Sv barotropic streamline; boundary current particles stay outside the streamline, interior particles are categorised in the interior which they enter first for at least 20 consecutive days. The border between the Labrador Sea and the Irminger Sea is a meridional section at 44° W, the border between the Irminger Sea and the Iceland Basin is the Reykjanes Ridge. The background shows the ocean bathymetry.

2.4.3. Temperature, Salinity and Density Changes

To analyse how and where temperature, salinity and density change, we create T,S diagrams and density change heatmaps. For the T,S diagrams we order the particles based on relative time, this is the time since release at DS. Relative time is used here to describe the typical thermohaline evolution of particles along their trajectory. To quantify seasonal differences, separate T,S diagrams for each release month are made instead. For every timestep we calculate the median conservative temperature and absolute salinity across particles as well as median depth. We use the median rather than the mean to represent the typical evolution across particles, because it is less affected by outliers. We do this for each of the categories of particles and also per month in which particles are released. The resulting T,S diagrams help answering how much temperature, salinity and density change.

To identify where in the SPNA particles become denser or more buoyant, we create density change heatmaps. We use the same $0.1° \times 0.1°$ (latitude, longitude)-grid as for the particle concentration maps. First, for each particle and each timestep, we calculated the rate of density change, $\frac{\mathrm{d}\sigma}{\mathrm{d}t}$. Next, we assign every particle to its corresponding grid cell based on its position at that timestep. Then, for each grid cell and timestep, we compute the median $\frac{\mathrm{d}\sigma}{\mathrm{d}t}$ across all particles present in that cell. Here, in contrast to the particle concentration maps, a particle is included every time it is present in a grid cell. This is to also capture density changes in areas with slow flow and recirculation, which would be underestimated if only unique visits would count. Finally, to obtain one representative value per grid cell, we take the mean of these values over all timesteps. The resulting maps show where particles on average increase or decrease in density. Positive and negative values are shown in separate heatmaps for clarity.

3

Results

3.1. Particle Concentration

Particle concentration maps provide a first impression of the main pathways in the SPNA. A map for all particles over all four seasons together is shown in Figure 2.6a together with the -22 Sv barotropic streamline. Since all particles start at the transect in Denmark Strait, the highest concentrations occur there. The Kangerlussuaq Trough and the circulation around it are clearly visible, as is the boundary current along the east coast of Greenland, which follows two branches: the East Greenland Coastal Current close to the shore on the Greenland shelf, and the East Greenland Current farther offshore at the shelf break. Around Cape Farewell the boundary current continues along the west coast of Greenland, circles the Labrador Sea, and continues along the east coast of Canada. At the Grand Banks, the boundary current splits into a southward branch and an eastward branch following the North Atlantic Current towards the UK.

One can also see that particles enter the interiors of the Irminger Sea, Labrador Sea and Iceland Basin. A larger fraction of particles enters the Labrador Sea than the Irminger Sea, indicating that this pathway is more likely followed. In the Labrador Sea, particle concentrations per grid cell range between 0.5 and 2%, whereas in the Irminger Sea they are between 0.1 and 0.5%.

Particle concentration maps for only particles with an initial density at DS of 27.8 kg/m^3 or higher, defined as dense particles, and for particles with an initial density at DS between 27.7 and 27.8 kg/m^3, defined as intermediate-density particles (Figure A.1), show similar patterns as Figure 2.6a. The boundary current is still clearly visible, just as the Kangerlussuaq Trough and particles entering the interior of the Irminger Sea, Labrador Sea and Iceland Basin. The largest difference in particle concentration between dense and intermediate-density particles is at the east coast of Greenland; the dense particles follow mainly the East Greenland Current, while the intermediate-density particles follow more the East Greenland Coastal Current. This difference becomes clear from Figure 3.1, which shows the difference in particle concentration for intermediate-density particles minus dense particles. Blue colours are locations where most particles are dense, while red colours are location where most particles are of intermediate-density. Locations with a light colour, have a small difference in percentage of dense and intermediate-density particles. At locations with a darker colour the difference is bigger. Locations with more dense than intermediate-density particles are further offshore than locations with more intermediate-density than dense particles. This is clearest at the east coast of Greenland and in the Labrador Sea. The East Greenland Coastal Current is marked in dark red and has more than 0.4 percent point more intermediate-density than dense particles. The East Greenland Current, marked in blue, on the other hand, transports more than 0.4 percent point more dense than intermediate-density particles. In the Labrador Sea interior we observe 0.1–0.4 percent point more dense than intermediate-density particles, while along the coasts of West Greenland and East Canada, and northward through Davis Strait, intermediate-density particles are more present than dense particles by similar margins. At the Grand Banks, the southward branch contains regions with nearly equal proportions of dense and intermediate-dense particles, as well as areas with up to 0.15 percent point more dense particles. The

eastward branch likewise has regions with equal proportions and regions containing up to 0.15 percent point more intermediate-density particles. Finally, in the interior of the Iceland Basin, dense and intermediate-dense particles occur in nearly equal proportions, with parts that have up to 0.1 percent point more dense particles.

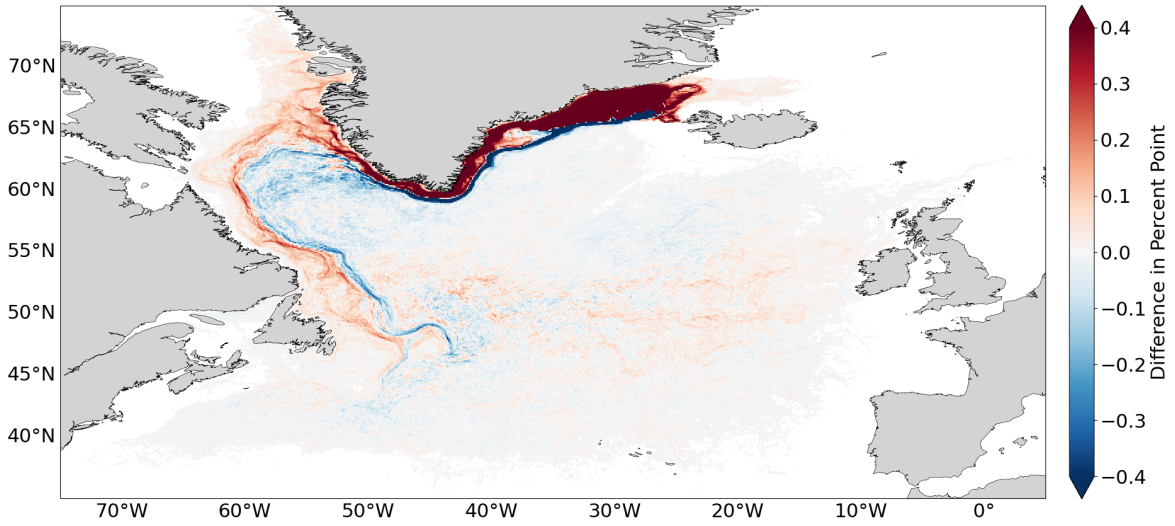

Figure 3.1: Difference in concentration for intermediate-density ($27.7 \leq \sigma < 27.8$ kg/m^3 at the moment of seeding at DS) minus dense ($\sigma \geq 27.8$ kg/m^3 at the moment of seeding at DS) particles in percentage point. Blue colours denote locations that are visited more by dense particles, while red colours denote locations that are visited more by intermediate-density particles.

As described in subsection 2.4.2, we divide the SPNA into a boundary current region and the interior regions of the Irminger Sea, Labrador Sea, and Iceland Basin to analyse particle distribution between boundary and interior in more detail. As Table 3.1 shows, of all particles 72.4% stays in the boundary current, 4.4% enters the Irminger Sea interior as first interior, 23.0% enters the Labrador Sea interior as first interior, and 0.15% enters the Iceland Basin as first interior.

The fact that so few particles enter the Iceland Basin interior as first interior is a consequence of our definition of when we consider a particle as IcB-particle. We only consider a particle as IcB-particle if it, after its release at DS, follows the boundary current all the way past the Irminger Sea, around the Labrador Sea, bends east with the NAC and then enters the Iceland Basin interior for at least twenty days. On its way to the Iceland Basin, a particle can make small excursions of less than 20 days to the Irminger Sea or Labrador Sea interior. If these excursions would be longer than 20 days, the particles would be considered as IrS- or LS-particle depending on which interior it enters. Another factor is the time of our simulation, which is only three years. Before reaching the Iceland Basin particles need to follow the boundary current over long distances. Three years may be too short for many particles to travel this path. For longer simulations we would expect more particles to reach the Iceland Basin interior as their first interior. Since so few particles enter the Iceland Basin, we will not consider them for further analysis.

Particle concentration maps for the boundary current, Irminger Sea and Labrador Sea particles are shown in Figure 3.2. Figure 3.2a shows the pathways of particles that remain within the boundary current. Overall, the particles follow the same pathways described at the beginning of this section. The main difference is seen at the east Greenland shelf, where a higher concentration of particles follow the EGCC rather than the EGC. As the boundary currents continues downstream, the particle concentration becomes smaller, from 5 to 10% on the east Greenland shelf to maximum 2% in the LC and NAC. This can be related to the fact that a lot of particle in the boundary current get stuck on the east and west Greenland shelves, while the particle concentration shown in the plot is still a percentage of all released particles. The boundary current is also clearly visible for particles that enter an interior meaning that these particles do not all stay in the interior but also leave the interior and re-enter the boundary current. Note that, at the east coast of Greenland, particles entering an interior mostly follow the EGC and to

a lesser extend the EGCC. Figure 3.2b shows particles that as first interior enter the Irminger Sea. Since the interior of the Labrador Sea shows particle concentrations between 1–5% per grid cell, this indicates that IrS-particles at a later time also enter the Labrador Sea interior. The opposite, where particles first enter the Labrador Sea interior and later the Irminger Sea interior, happens as well, yet to smaller extent. This can be seen from Figure 3.2c which shows particle concentrations for particles that as first interior enter the Labrador Sea. The south-western part of the Irminger Sea interior is coloured with particle concentrations between 0.1–0.7% per grid cell indicating that Labrador Sea particles also enter the Irminger Sea interior at a later time.

Table 3.1: Percentage of particles classified in each region.

Boundary Current	Irminger Sea	Labrador Sea	Iceland Basin
72.4%	4.4%	23.0%	0.15%

Figure A.2 shows particle concentration maps as in Figure 3.2 for the dense and intermediate-density particles separately. In order to identify differences in pathways that dense and intermediate-density particles follow, we analyse the difference in particle concentration between intermediate-density and dense particles per region shown in Figure 3.3. For all regions, we observe more intermediate-density particles closer to the coast, while offshore we find larger concentrations of dense particles. For every region, the EGCC transports more intermediate-density than dense particles and is marked in dark red. On the other hand, the EGC carries a higher percentage of dense than intermediate-density particles and is marked in blue. For particles that stay in the boundary current (Figure 3.3a), this separation disappears at the west coast of Greenland where the topographic slope steepens. Here increased eddy activity can enhance mixing which can result in regions with equal concentrations of dense and intermediate-density particles. For IrS- and LS particles (Figure 3.3b and Figure 3.3c) a higher percentage of dense particles enters the interior. At the Grand Banks, the LS-particles have a higher concentration of dense particles (0.25 – 0.75 percent point) in the southward branch, while the eastward branch is a mix of dense and intermediate-density particles alternating close to each other. For Irminger Sea particles both the southward branch and eastward branch are a mix of dense and intermediate-density particles.

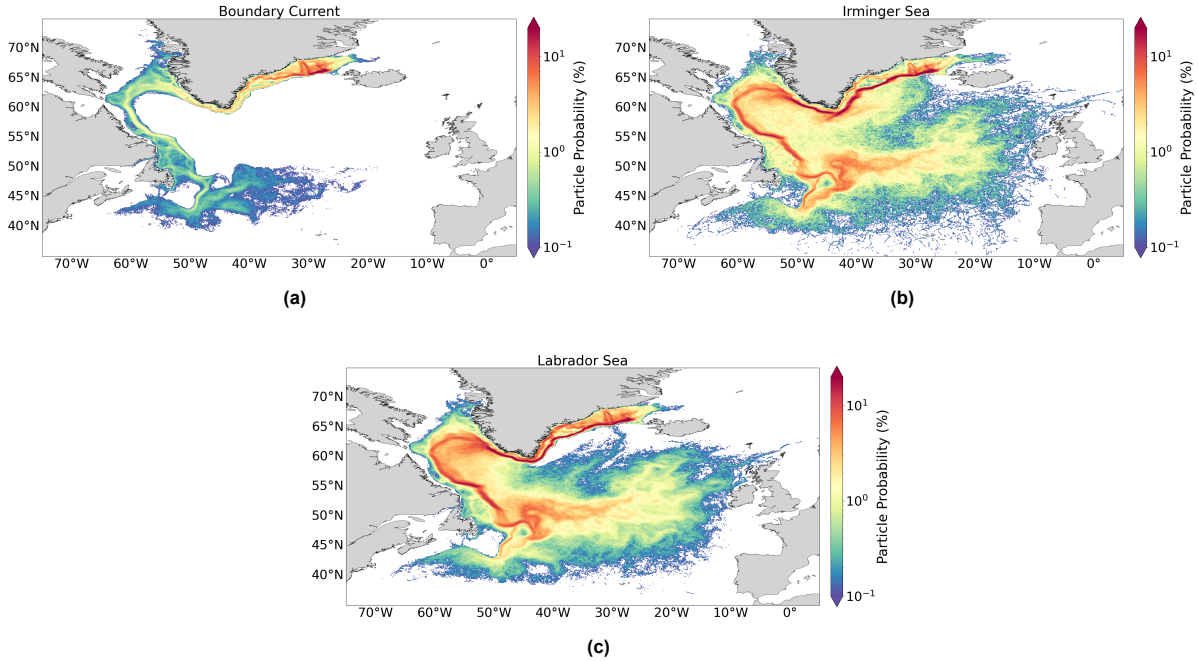

Figure 3.2: Concentration plots for all particles classified in **(a)** the boundary current, **(b** the Irminger Sea interior and **(c)** the Labrador Sea interior. How particles are classified in a region is explained in subsection 2.4.2. The particle probability is as a percentage of the number of particles per region.

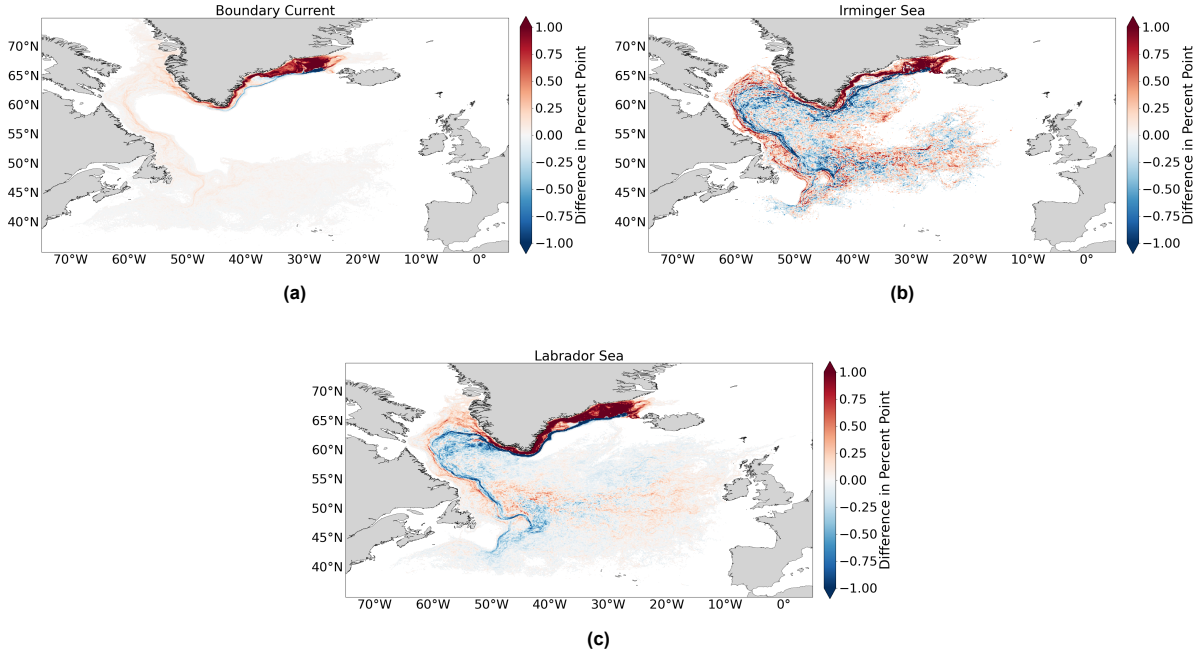

Figure 3.3: Difference in particle concentration (intermediate-density ($27.7 \leq \sigma < 27.8$ kg/m^3 at the moment of seeding at DS) minus dense ($\sigma \geq 27.8$ kg/m^3 at the moment of seeding at DS) for all particles in **(a)** the boundary current, **(b)** the Irminger Sea interior and **(c)** the Labrador Sea interior.

3.1.1. Seasonal Differences

Another way to analyse particle trajectories is to look into difference between particles released in different months. In every month of release, particles are divided in a similar way over the regions as before when taking all particles together. The largest percentage of particles is found in the boundary current; the second largest percentage is in the Labrador Sea; third is the Irminger Sea and the Iceland Basin is the smallest. Figure 3.4 shows a histogram of the number of particles per region (BC, IrS, LS) per month they are seeded. For every region the bars from left to right represent particles seeded in June ‘22, September ‘22, December ‘22 and March ‘23.

The numbers of the histogram are shown as percentages in Table 3.2. This table gives the percentage of particles in a region per month compared to the total number of particles in that month. E.g. 77% boundary current in June means that 77% of the particles seeded in June is categorised as boundary current particles. Particles seeded in September and December ‘22 have very similar percentages per region. The biggest difference in percentages is between particles seeded in June ‘22 and particles seeded in March ‘23. In March there is 13 percent point less particles categorised as boundary current than in June, 64% compared to 77%. To balance this, more particles are categorised as IrS- and LS-particles, 5.8% compared to 4.4% for the Irminger Sea, and 30% compared to 18% for the Labrador Sea. So the highest percentage of particles entering an interior is for particles seeded in March. In this month the gradient in density between the interiors and the boundary current is the largest because the interiors are very dense due to winter cooling. This large gradient creates baroclinic instabilities and a high eddy activity driving large boundary-interior exchanges (Brüggemann and Katsman, 2019, Fan et al., 2013). This is consistent with the seasonal restratification cycle described in the introduction, in which eddies transport heat and salt from the boundary current back into the interior after winter cooling.

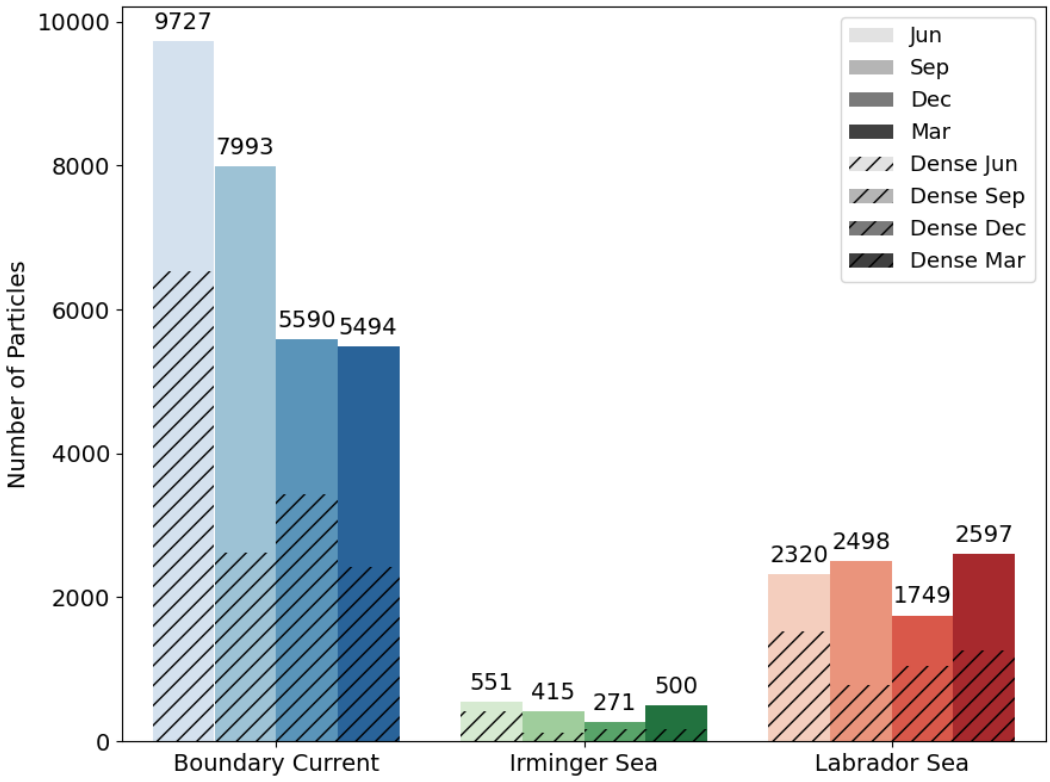

Figure 3.4: Histogram of the number of particles per region (BC, IrS, LS) per month they are released. For every region the bars from left to right represent particles seeded in June '22, September '22, December '22 and March '23. On top of the bar is the number of particles in that region and month. Summing the numbers of all bars in a region gives the total number of particles categorised as that region; adding the numbers of one month for all three regions plus the IcB-particles gives the total number of particles seeded in that month. Note that the IcB-particles are not shown here. The hatched area of every bar shows the fraction of dense ($\sigma \geq 27.8$ kg/m^3 at the moment of seeding at DS) particles in that bar.

Table 3.2: Percentage of particles in a region per month compared to the total number of particles in that season. E.g. 77% boundary current in June means that 77% of the particles seeded in June are categorised as boundary current particles.

	Boundary Current	Irminger Sea	Labrador Sea
June	77%	4.4%	18%
September	73%	3.8%	23%
December	73%	3.6%	23%
March	64%	5.8%	30%

Particle concentration maps per region and per month of initialisation all show similar patterns as the particle concentration maps per region for all months together in Figure 3.2. For completeness the figures are added in Appendix A (Figures A.3, A.4 and A.5). Particle concentration difference plots in Figures 3.5 to 3.7 show big differences per month of seeding. These plots show the difference in concentration of intermediate-density minus dense particles per region (BC-particles in Figure 3.5, IrS-particles in Figure 3.6 and LS-particles in Figure 3.7) per month of seeding (June '22 in a, September '22 in b, December '22 in c and March '23 in d).

For all three regions, for particles seeded in June and December '22, most grid cells contain a higher percentage of dense particles than intermediate-density particles. For September '22 and March '23,

the opposite is true: most grid cells have a higher percentage of intermediate-density particles. An exception is the Labrador Sea in March, where grid cells with a higher percentage of intermediate-density and grid cells with a higher percentage of dense particles alternate. In the EGC, WGC and NAC there are more intermediate-density particles, whereas in the interior of the Labrador Sea and south of the Grand Banks there are also grid cells with a higher percentage of dense particles.

This pattern can be explained by the density composition of the particles at the moment of release. In June, 67% of the released particles is dense; in December, 62%; in September, only 32%; and in March, 45%. We expect a seasonal pattern with denser water in December and March and more buoyant water in June and September, although there can be a delay in the transport of dense water. The passage of boluses and pulses as explained in subsection 2.2.1 can also play a role by increasing the transport of dense water over the sill in June and December.

In June and December, when almost all grid cells have a higher percentage of dense particles, the released particles also have the highest fraction of dense particles. Conversely, in September, when most grid cells contain a higher percentage of intermediate-density, the smallest fraction of released particles is dense. In March, when grid cells with a higher percentage of intermediate-density and grid cells with a higher percentage of dense particles alternate, the released particles are nearly evenly split, with slightly less than half being dense.

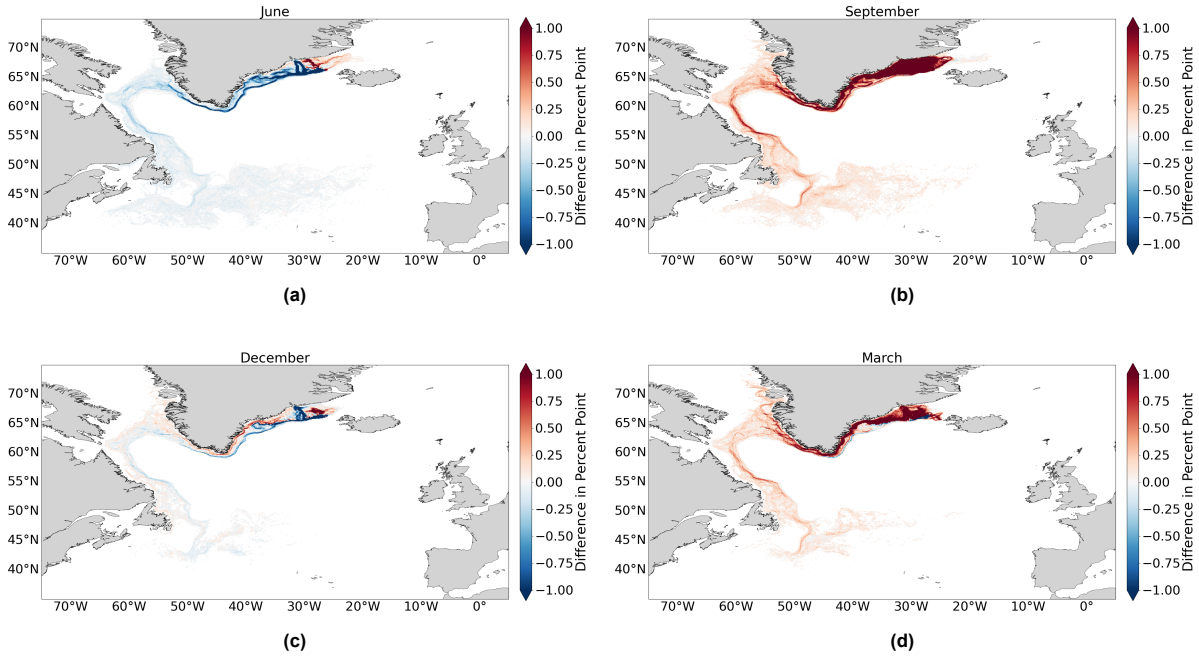

Figure 3.5: Difference in particle concentration (intermediate-density ($27.7 \leq \sigma < 27.8$ kg/m^3 at the moment of seeding at DS) minus dense ($\sigma \geq 27.8$ kg/m^3 at the moment of seeding at DS)) for all particles that stay in the boundary current and are seeded in **(a)** June '22, **(b)** September '22, **(c)** December '22 and **(d)** March '23.

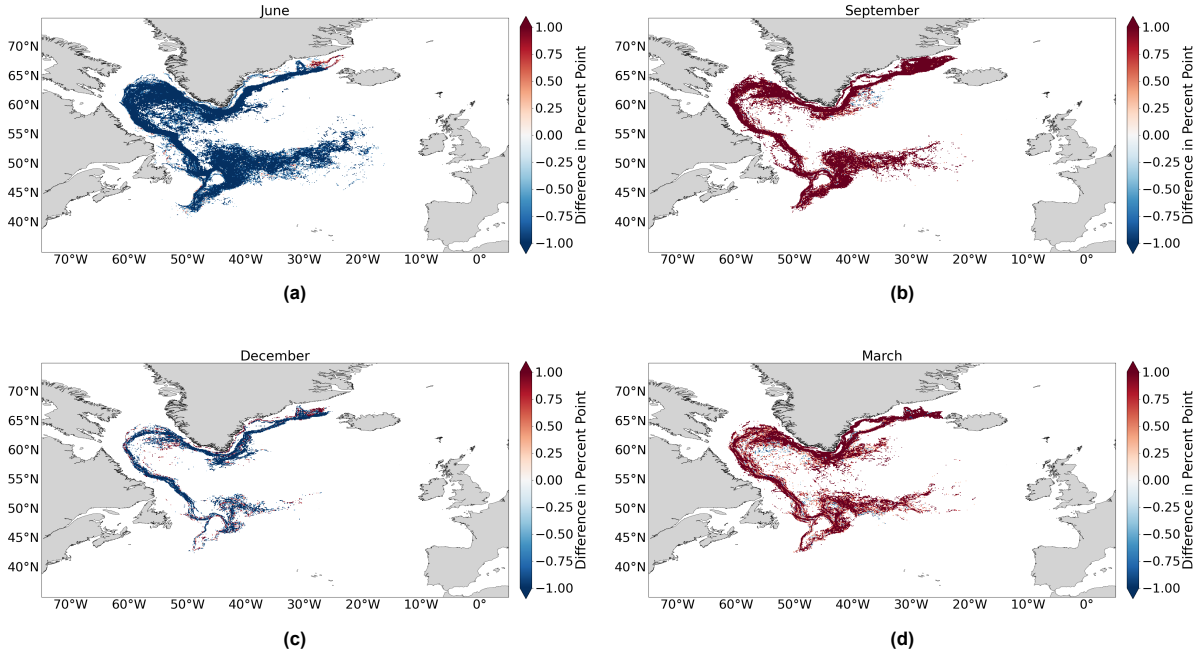

Figure 3.6: Difference in particle concentration (intermediate-density ($27.7 \leq \sigma < 27.8$ kg/m^3 at the moment of seeding at DS) minus dense ($\sigma \geq 27.8$ kg/m^3 at the moment of seeding at DS) for all particles that enter the Irminger Sea interior as first interior and are seeded in **(a)** June '22, **(b)** September '22, **(c)** December '22 and **(d)** March '23.

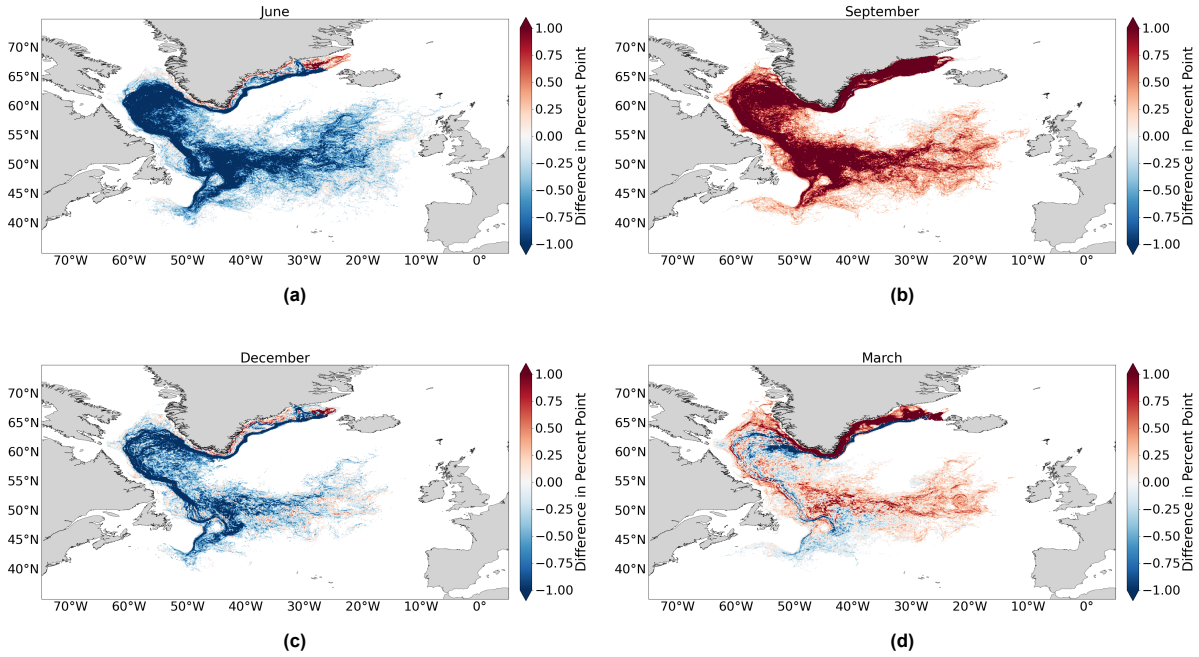

Figure 3.7: Difference in particle concentration (intermediate-density ($27.7 \leq \sigma < 27.8$ kg/m^3 at the moment of seeding at DS) minus dense ($\sigma \geq 27.8$ kg/m^3 at the moment of seeding at DS) for all particles that enter the Labrador Sea interior as first interior and are seeded in **(a)** June '22, **(b)** September '22, **(c)** December '22 and **(d)** March '23.

3.2. Evolution of Temperature, Salinity and Density

The T,S diagram in Figure 3.8 shows median temperature, salinity and density for in blue BC-particles, in orange IrS-particles and in red LS-particles released in June, September and December '22 and March '23 together. All regions have an initial median density higher than 27.8 kg/m^3 and the overall trend is that particles get warmer and more saline over time. For each region, particles first show an increase in

both temperature of 2 to 4 °C and salinity of 0.10 to 0.15 g/kg. This is because the water is released at Denmark Strait and immediately enters warmer and more saline water. BC-particles show the biggest changes with absolute salinities decreasing from 34.9 to 33.5 and again increasing to 35.8 g/kg and conservative temperatures changing from 1 to 15 °C. This results in density decrease from 27.8 up to 26.6 kg/m^3. The IrS- and LS-particles show much smaller variations than the BC-particles and show a very similar pattern of change to each other. LS-particles show a slightly lower salinity and higher temperature than IrS-particles. For the IrS-particles absolute salinity and conservative temperature change from 34.9 to 35.2 g/kg and from 1 to 9 °C with resulting density decrease from 27.8 to 27.2 kg/m^3. For the LS-particles temperature and salinity change from 34.8 to 35.4 g/kg and from 1 to 11 °C, respectively with density decreasing from 27.8 to 27.0 kg/m^3.

Figure 3.9 shows the same T,S evolution as in Figure 3.8 for each of the regions separately. The shading on the T,S evolution gives the median depth of the particles per time step of relative time. The black dots on the T,S evolution indicate intervals of 100 days travel time. Particles that stay in the boundary current (Figure 3.9a) increase temperature by about 2 °C in the first 100 days. From 100 to 400 days the particles experience a strong diapycnal decrease in density of 1.0 kg/m^3 due to a decrease in salinity. Also temperature decreases from 3.7 °C to 2.5 °C. This fits in the general trend that the boundary current gets colder and less saline as it travels from Greenland downstream to the Labrador Coast (Brüggemann and Katsman, 2019, Yashayaev, 2024). Also the median temperature is below 4.1 °C so that according to Brüggemann and Katsman (2019) diapycnal processes become important and there is a diapycnal transport from the warmer into the colder layer. From Figure 3.10b one can see that most of the particles are located on the shelf in the EGCC, which is a current with low salinity, and in the WGC. Between 400 and 500 days travel time, the median temperature and salinity hardly change. At this time, particles are spread out over the EGCC, WGC, LC and the Grand Banks as can be seen in Figure 3.10c. Taking the median of cold and fresh water at the Greenland shelf and more warm and saline water further toward the Grand Banks makes that it averages out and not so much change is seen. Here we also observe strong decrease in particle probability which can be related to particles getting stuck on the east and west Greenland shelf. After 500 days the water experiences a strong increase in both temperature of 12 °C and salinity of 2.4 g/kg, that is mostly isopycnal. The median particle depth in the water column is decreasing in this part to very shallow depths between 0 and 40 meters, indicating that particles rise in depth-space but not in density space. This implies that the isopycnal they follow tilts upward toward the surface downstream and that surface waters are entrained into deeper and denser layers. From Figure 3.10d it can be seen that most of the particles are at the Labrador Coast, at the Grand Banks and in the NAC. There are hardly any particles on the Greenland shelf left. Although particles at the Labrador Coast are still in a regime with low temperatures and salinities, most particles are past the Grand Banks and experience the inflow of warm and saline waters of the NAC.

Figures 3.9b and 3.9c show that IrS- and LS-particles both experience a 4 °C temperature increase and 0.15 g/kg salinity increase in the first 50 days that results in a decrease in density of just over 0.2 kg/m^3. The particles experience these changes as they enter the SPNA in the EGC and are not yet in an interior as can be seen from Figures 3.11a and 3.12a. Between 50 and 400 days temperature and salinity decrease along the isopycnal. Both the IrS- and LS-particles temperature decrease 1 °C, while salinity decreases by 0.15 g/kg for IrS-particles and by 0.2 g/kg for LS-particles. From Figure 3.11b we can see that IrS-particles at that moment are located in the EGC, WGC, LC and in the interior of the Irminger Sea and also in the interior of the Labrador Sea. LS-particles in Figure 3.12b are also found in the boundary current, in the EGC, EGCC, WGC and LC, and in the interior of only the Labrador Sea. From 400 to 850 days particles experience a diapycnal decrease in density due to an increase in temperature and salinity. For the IrS-particles temperature increases by 4 °C and salinity increases by 0.15 g/kg. For LS-particles temperature increases by 5 °C and salinity by 0.2 g/kg. As can be seen from Figures 3.11c and 3.12c particles are mostly at the coast of Labrador and Newfoundland, at the Grand Banks and in the NAC. IrS-particles are also still in the interior of the Irminger Sea and Labrador Sea. LS-particles are also found in the interior of the Labrador Sea and a very small percentage in the south-western part of the interior of the Irminger Sea. The last 245 days, where both IrS- and LS-particles experience an increase in salinity while temperature stays approximately constant most of the particles are located in the NAC from Canada up to the United Kingdom as can be seen from Figures 3.11d and 3.12d. Here particles mix with warm and saline NAC-water but particles also already start

losing heat to the atmosphere as they flow towards the UK. Hence the median temperature stays more or less constant while the water does get more saline.

Looking at the median particle depth, it can be seen that IrS-particles stay at greater depths than BC-particles and LS-particles but that all particles have relatively shallow depth. Regarding the particles depth of maximum 310 m, it is unlikely that a high fraction of particles gets into de DWBC that is deeper than 400 m (Handmann et al., 2018). Since the DWBC is an important current in transproting DSOW or deep water in general this is surprising.

From panels b and c in Figures 3.11 and 3.12 we see that particles are widely spread across both the boundary current and interior regions their temperature and salinity changes. Because these changes occur while particles are spread over many different locations rather than concentrated in one area, we do not identify a specific region where these changes occur.

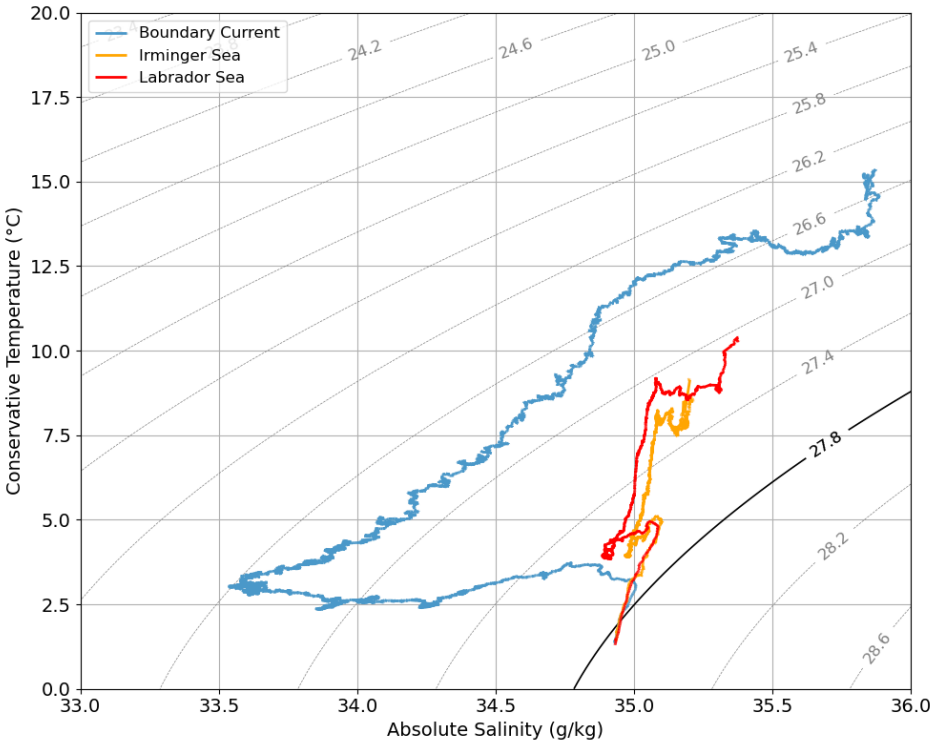

Figure 3.8: T,S diagram showing how median salinity (x-axis) and temperature (y-axis) evolve over time for all particles per region. The dashed gray contours indicate isopycnals with the 27.8 kg/m^3 highlighted in solid black. The blue line is the T,S evolution for BC-particles, orange for IrS-particles and red for LS-particles. How particles are classified in a region is explained in subsection 2.4.2.

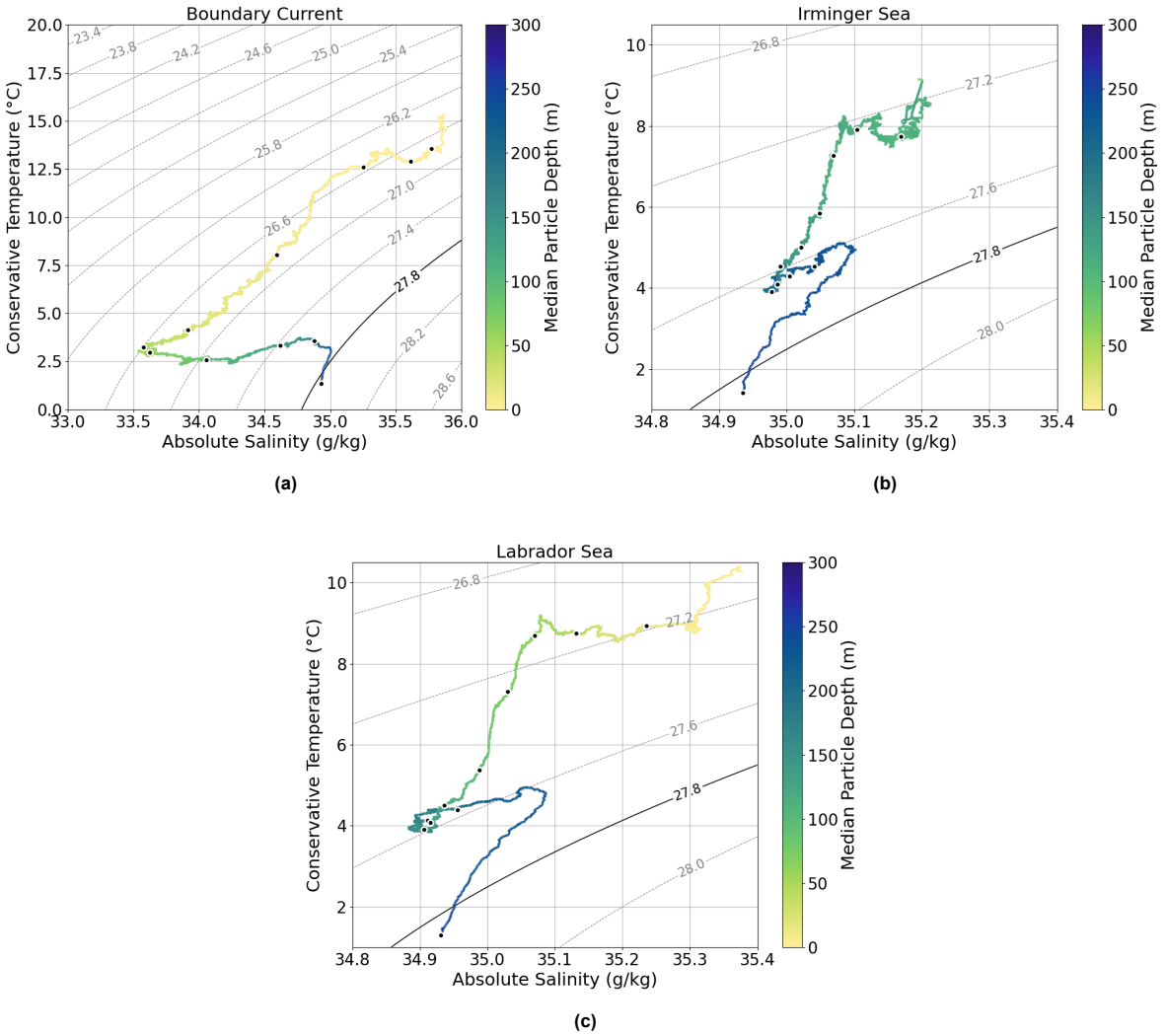

Figure 3.9: T,S diagrams showing how median salinity (x-axis) and temperature (y-axis) evolve over time for **(a)** BC-particles, **(b)** IrS-particles and **(c)** LS-particles. The dashed gray contours indicate isopycnals with the 27.8 kg/m^3 highlighted in solid black. The trajectory is coloured by median particle depth. The dots on the T,S evolution indicate intervals of 100 days since release.

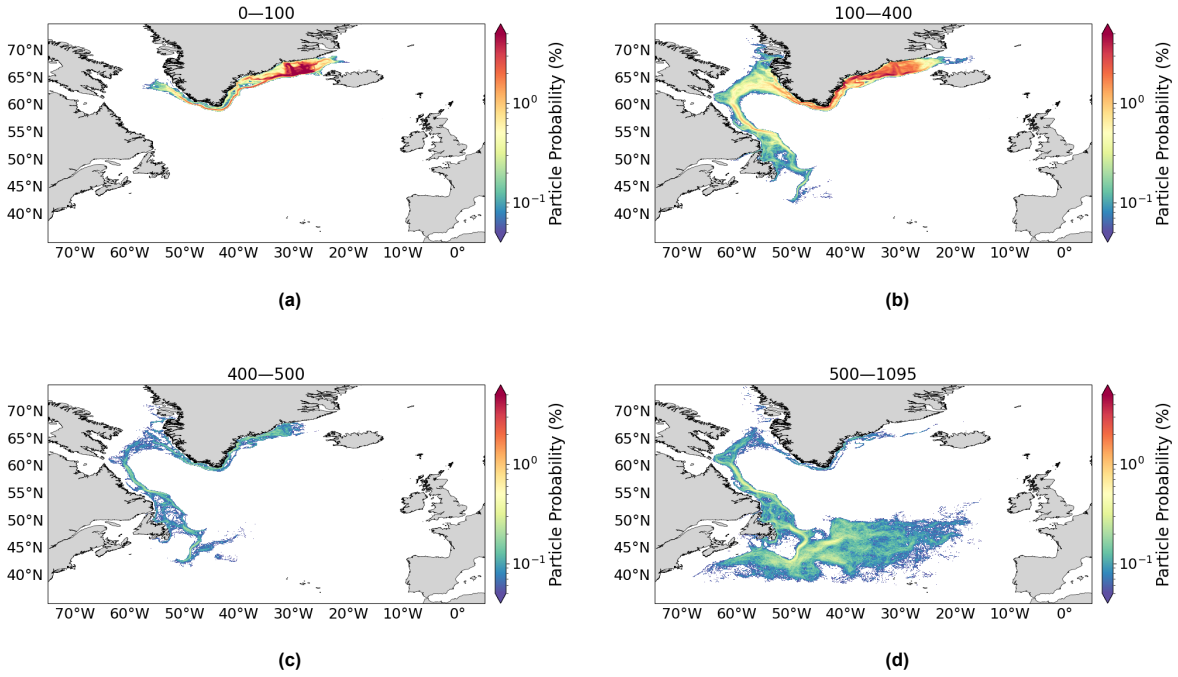

Figure 3.10: Particle concentration maps of BC-particles at given intervals of relative time: **(a)** 0 to 100 days, **(b)** 100 to 400 days, **(c)** 400-500 days and **(d)** 500 days till the end of the simulation.

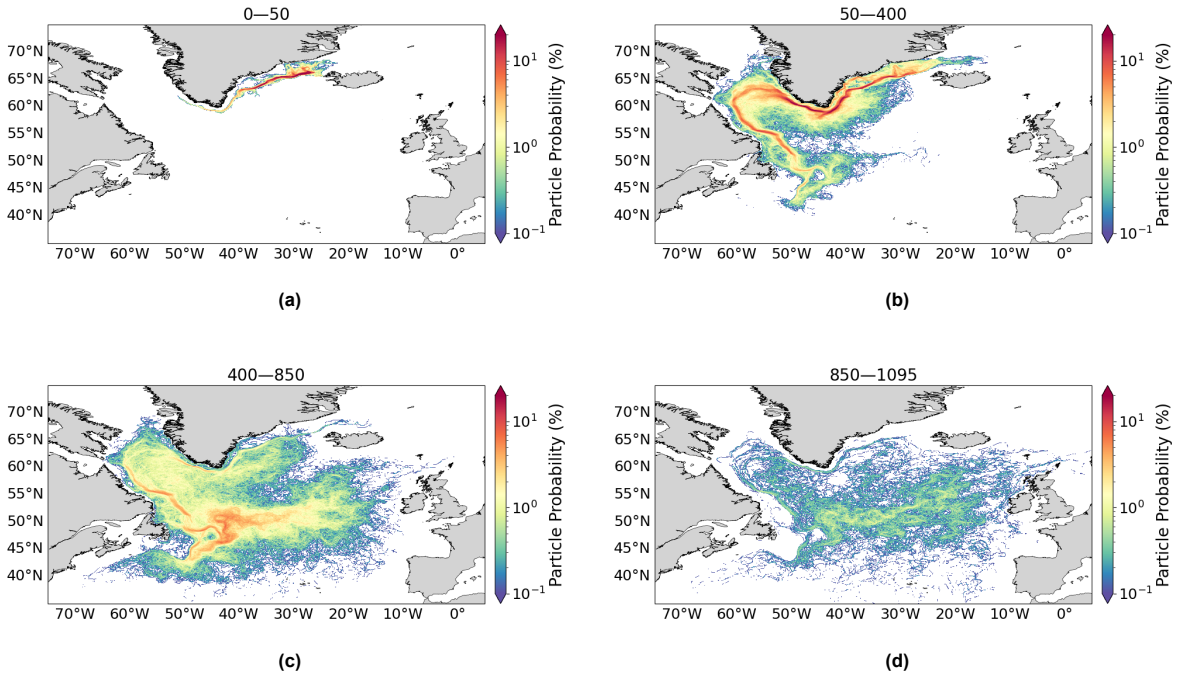

Figure 3.11: Particle concentration maps of IrS-particles at given intervals of relative time: **(a)** 0 to 50 days, **(b)** 50 to 400 days, **(c)** 400-850 days and **(d)** 850 days till the end of the simulation.

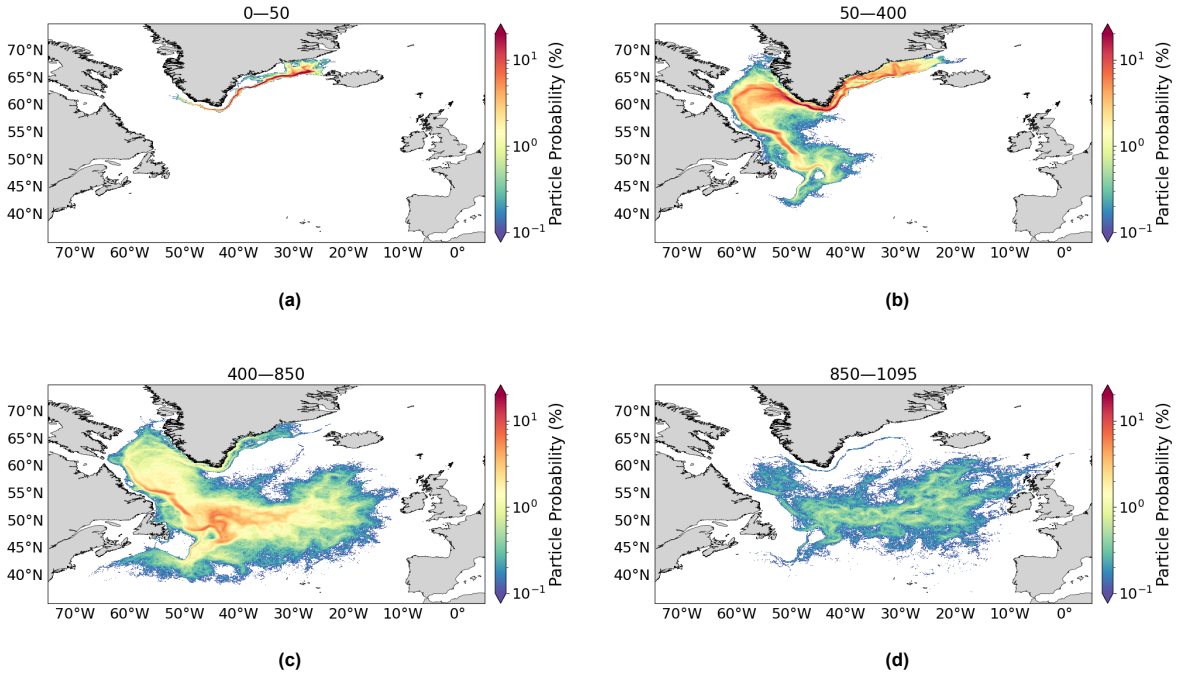

Figure 3.12: Particle concentration maps of LS-particles at given intervals of relative time: **(a)** 0 to 50 days, **(b)** 50 to 400 days, **(c)** 400-850 days and **(d)** 850 days till the end of the simulation.

3.2.1. Spread in T, S, sigma

The T,S diagrams show median temperature, salinity, density and depth of particles. The spread in these properties is shown in Figures 3.13a – d for BC-particles (left), IrS-particles (middle) and LS-particles (right), with dense particles in darker colours and intermediate-density particles in lighter colours.

From Figure 3.13a it can be seen that BC-particles have the biggest range in temperature, salinity and density consistent with the T,S diagrams. LS-particles are slightly warmer than IrS-particles and BC-particles have the shallowest depth. What did not appear from the T,S diagrams is that the temperature is concentrated around two peaks. For BC-particles, the dense particles are concentrated between 2 – 4 °C and 13 – 14 °C, while the intermediate-density particles are shifted to about 0.5 °C lower temperatures. Interior particles have narrower ranges but clearer separation between dense and intermediate-density particles. Dense IrS-particles are concentrated around 3.5 – 5.5 °C and at 7 – 8 °C, and intermediate-density particles around 4 – 5 °C and 8 – 9.5 °C. LS-particles mainly have temperatures between 3.5 – 5.5 °C and between 8 – 9 °C for the dense particles; the intermediate-density particles peak from 3.5 – 4.5 °C and from 8.5 – 9.5 °C. The two peaks may reflect polar- and Atlantic-origin water. For interior particles, they might also be related to particles that stay in the interior and particles that later rejoin the boundary current. The slightly higher temperatures of intermediate-density particles in the Irminger Sea compared to the Labrador Sea can be explained by the warmer boundary current around the Irminger Sea than around the Labrador Sea.

As shown in Figure 3.13b, BC-particles span a wide salinity range (33.5 – 35.9 g/kg) for both dense and intermediate-density particles, with a nearly uniform distribution except for fewer particles between 35.1 – 35.4 g/kg. This gap corresponds to the salinity at which both IrS- and LS-particles peak. IrS-particles show similar salinities for dense and intermediate-density particles between 34.95 – 35.2 g/kg. LS-particles show a wider range in salinity for intermediate-density particles (34.7 – 35.5 g/kg) compared to dense particles (34.95 – 35.3 g/kg). This might indicate that water masses with relatively consistent salinity values develop in the Irminger Sea and Labrador Sea interior. These water masses may subsequently be exported from the SPNA, possibly via the boundary current, without substantial mixing with surroundign water masses. The wider range for intermediate-density LS-particles may result from a small part of the boundary current being included in the Labrador Sea interior, causing some particles that stay in the boundary current to be classified as LS-particles.

BC-particles also show a larger density range (Figure 3.13c) from 26.1 – 27.7 kg/m^3 than IrS- and LS-particles, with dense particles concentrated between 26.1 – 26.8 kg/m^3 and intermediate-density particles between 26.3 – 26.8 kg/m^3. For BC-particles the distribution of density is similar for dense and intermediate-density particles, while interior particles show a clearer difference in distribution between the two. All groups display two peaks in density around which the particles are concentrated, though these are least pronounced for dense IrS-particles. Because density depends on both temperature and salinity, the two density peaks likely relate to the two temperature peaks and may again reflect difference between particles that remain in the interior and those that re-enter the boundary current. For LS-particles, the peak representing the most buoyant water may additionally reflect particles in the boundary current that are nevertheless classified as LS-particle.

From Figure 3.13d it can be seen that 35 to 40% of BC-particles have very shallow depth between 0 – 10 m. They show similar distributions for dense and intermediate-density particles, while interior particles show clear differences between the two densities. For the IrS-particle, most of the intermediate-density particles are located between 0 – 220 m depth with a gap between 20 – 60 m. The dense particle on the other hand are located between 120 – 310 with two peaks from 140 – 150 m and from 250 – 270 m depth. For LS-particles we see a similar spread with intermediate-density particles at depths between 0 – 210 m and dense particles between 10 – 310 m depth with a peak from 210 – 220 m and gaps with no particles at depths from 30 – 60 and from 90 – 110 m. The depth peaks likely correspond to the peaks in temperature and density, again distinguishing between particles that stay in the interior and particles that re-enter the boundary current. The high concentration of intermediate-density LS-particles between 0 an 20 m depth might be related to the boundary current particles that we classify as LS-particles. Why there are certain depths with no particles for both IrS- and LS-particles is unclear.

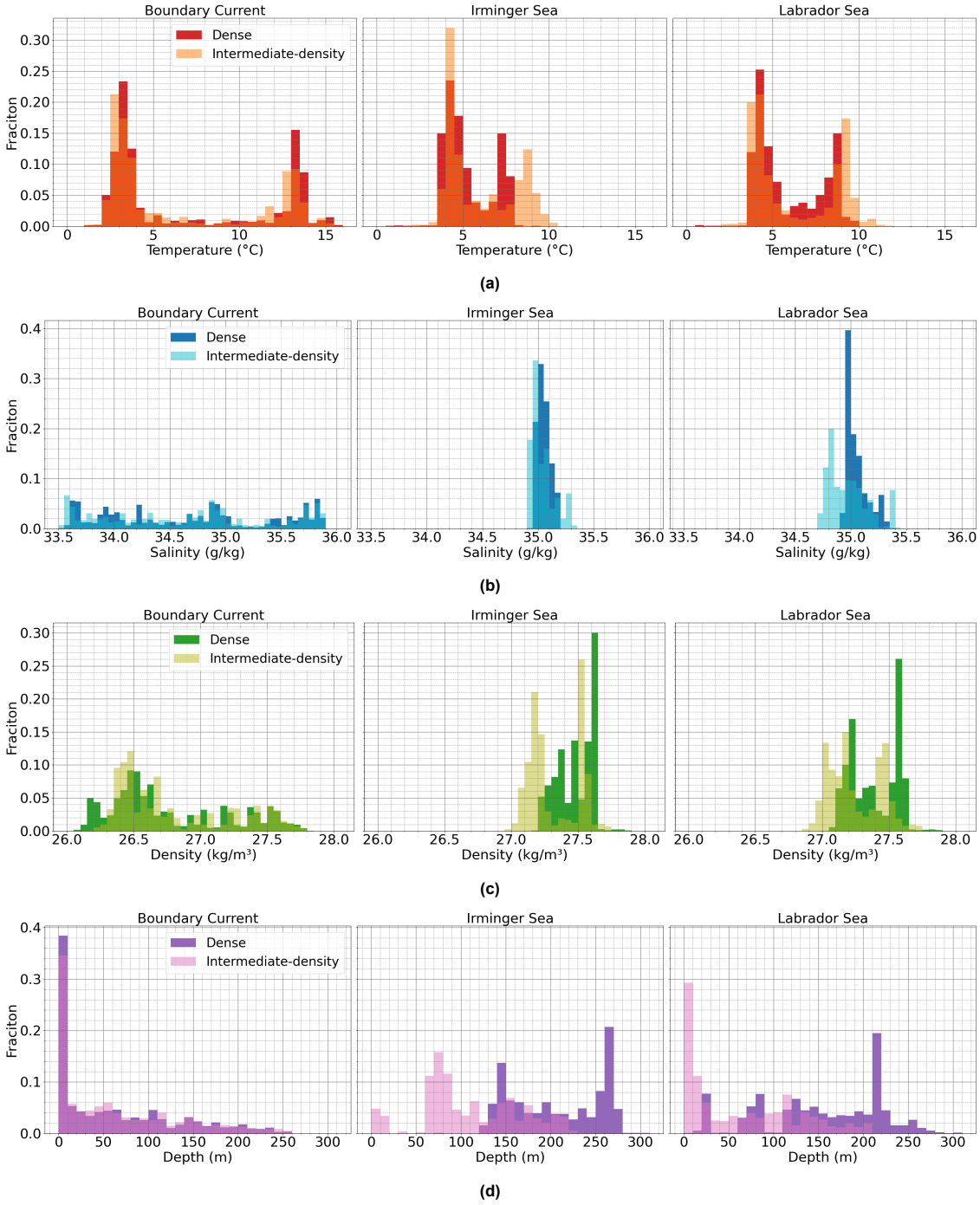

Figure 3.13: Histograms of **(a)** temperature, **(b)** salinity, **(c)** density and **(d)** depth for BC-particles (left), IrS-particles (middle) and LS-particles (right). The lighter colour represents intermediate-density particles ($27.7 \leq \sigma < 27.8$ kg/m^3 at the moment of seeding at DS) and the darker colour dense particles ($\sigma \geq 27.8$ kg/m^3 at the moment of seeding at DS).

3.2.2. Seasonal Differences in median T,S evolution

The diagrams in Figure 3.14 show T,S evolution for BC-, IrS- and LS-particles releases in (a) June ‘22, (b) September ‘22, (c) December ‘22 and (d) March ‘23. The T,S evolution of particles in one region show a similar trend for each of the four months of release, which also agrees with the trend seen in Figure 3.8. For all regions and all months of release the overall trend is a decrease in density by warming and salinisation. Lowest densities are observed for particles released in June and September; for December and March particles remain denser. The largest ranges in temperature and salinity are observed for particles seeded in June ‘22. Considering first the BC-particles, they first experience a

strong diapycnal freshening followed by a substantial increase in temperature and salinity which, to a varying extent, follow the isopycnals. The range in salinity is similar for all months, with minimum values around 33.5 g/kg and maximum values between 35.5 and 35.9 g/kg. The temperature varies more strongly per month of release. Minimum temperatures are between 0 and 1.5 °C, while maximum temperatures reach about 12.5 °C for particles released in September, December, and March, and nearly 20 °C for those released in June.

IrS- and LS-particles show very similar patterns to each other. Both experience mainly an increase in temperature and a much smaller variation in salinity. Salinity ranges between 34.8 and 35.2 g/kg, except for LS-particles in June; here salinity ranges between 34.6 and 35.4 g/kg. These particles also experience the largest variation in temperature between 0 °C and 12 °C. This is the largest spread in temperature together with IrS-particles released in June that have temperatures between 0 and 10 °C. Particles released in December and March experience the smallest variability in temperature and remain colder and denser.

The T,S evolution is plotted from the month of release until the end of the simulation (31-05-2025), meaning that every trajectory spans multiple seasons. The variation in median temperature, salinity and density therefore cannot directly be linked to a specific season or seasonal processes such a winter cooling or summer restratification. However, it does become clear that the season in which particles are released can have influence on the evolution of temperature, salinity and density that particles experience along pathways. The seasonal difference we can observe from these plots is at the moment of release at DS. It can be seen that particles released in June have the highest median density with lowest median temperature and medium median salinities. Particles released in September are the most buoyant due to the freshest median salinity and relatively high median temperatures. The highest median temperatures are observed in particles released in March when particles also have the highest median salinity which result in relatively buoyant water. Particles released in December have a relatively fresh median salinity and low median temperature which result in a relatively high median density at the moment of release. Overall, the particles released in June and December have the highest median density, particles released in September are the most buoyant and particles released in March have a median density in between. This can be related to the fraction of particles that is dense at the moment of release. Recall from subsection 3.1.1 that the percentage of dense particles at the moment of release is highest in June (67%) and December (62%) in which we also observe the highest median density. In September the smallest fraction of particles, 30%, is dense at the moment of release when we also observe the lowest median density; and in March 45% of the particles is dense at the moment of release when we observe a relatively low median density. These patterns therefore are consistent with the variability in overflow density described and explained earlier in subsection 3.1.1.

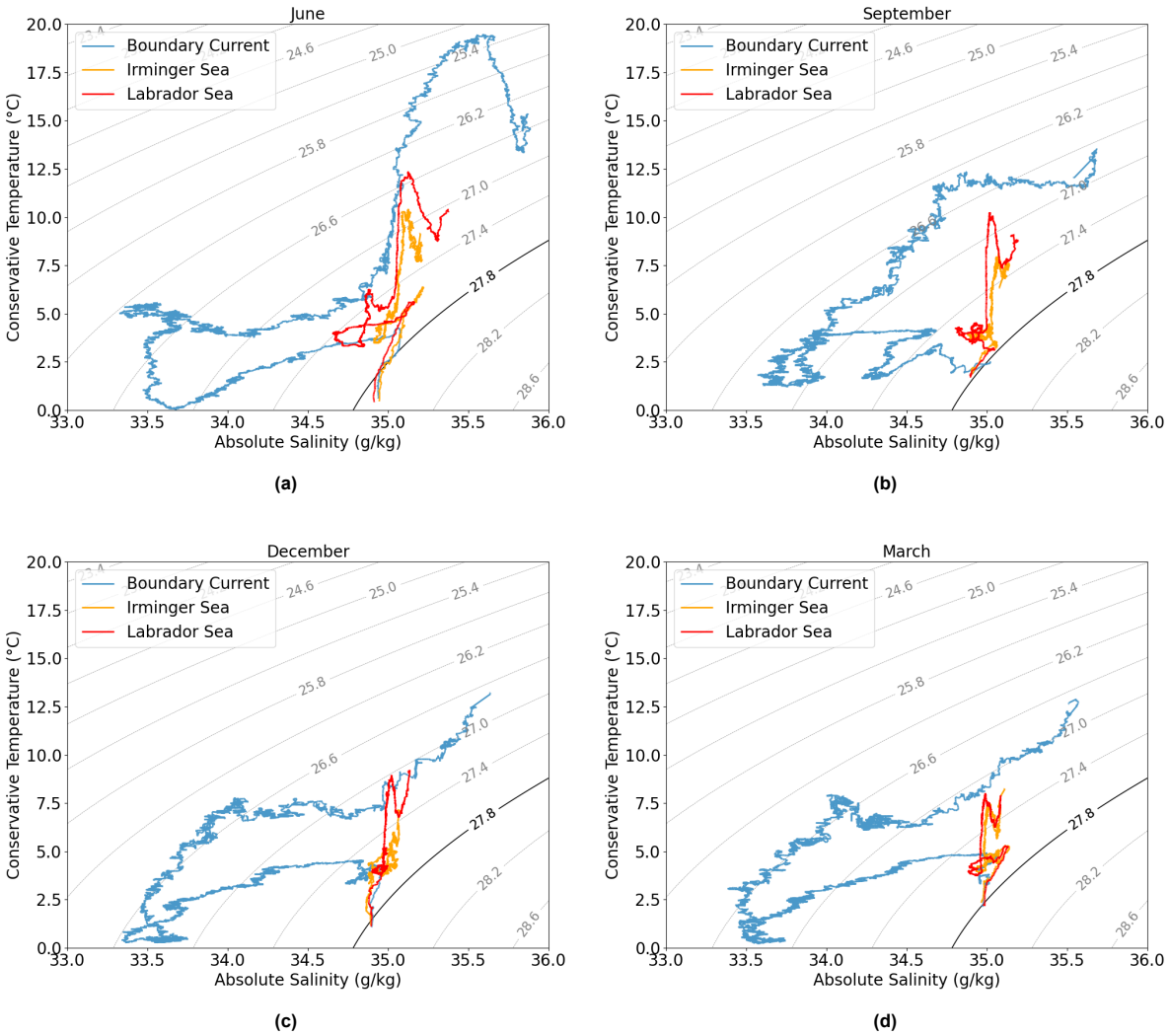

Figure 3.14: T,S diagrams showing how median temperature (y-axis) and salinity (x-axis) change over time for particles seeded in **(a)** June '22, **(b)** September '22, **(c)** December '22 and **(d)** March '23. Blue are BC-particles, orange are IrS-particles and red are LS-particles.

3.2.3. Density Change Heatmaps

From the T,S diagrams and corresponding particle concentration maps we could not distinguish certain hotspots for density changes. Figures 3.15 to 3.18 show heatmaps of density changes over time, $\frac{\mathrm{d}\sigma}{\mathrm{d}t}$, for (a) dense particles and (b) intermediate-density particles. The left panels show density increases (positive $\frac{\mathrm{d}\sigma}{\mathrm{d}t}$, particles get denser) and the right panels show density decreases (negative $\frac{\mathrm{d}\sigma}{\mathrm{d}t}$, particles get more buoyant). Figure 3.15 is the density change heatmap for all particles together. Figure 3.16, Figure 3.17 and Figure 3.18 respectively show density change heatmaps for all BC-particles, IrS-particles and LS-particles. One can see that the grid cells with the largest values of $\frac{\mathrm{d}\sigma}{\mathrm{d}t}$, both increase and decrease, are at the margins of the area of the SPNA. In the EGCC, WGC and LC particles have a stronger decrease than increase in density, indicating that the water there gets more buoyant. Fresh outflow from the Arctic and inflow from fresh glacier melt water can explain this. Noteworthy is the strong increase in density on the upstream part of the Kangerlussuaq Trough. Between 35° N and 45° N there is a lot of activity in density change, both increase and decrease, because of interaction between the SPG and STG. The NAC shows a stronger increase in density due to heat loss to the atmosphere.

From Figures 3.17 and 3.18 one can see that particles that enter an interior have bigger changes in density per grid cell than all particles together in Figure 3.15. This is visible in both the boundary current and in the interiors, where still the largest changes take place in the boundary current. We again see

stronger decreases in density in the EGCC, WGC and LC and stronger increases in density in the NAC. Note that particles that enter the Irminger Sea as first interior (Figure 3.17) show stronger density changes in the Iceland Basin than in the Irminger Sea and that particles that enter the Labrador Sea as first interior (Figure 3.18) show stronger density changes in the Irminger Sea and Iceland Basin than in the Labrador Sea. In the Labrador Sea, particles experience the smallest amount of density change.

By comparing the density change heatmaps for dense and intermediate-density particles in (a) and (b) respectively, BC-particles appear to experience a similar amount of increase as decrease. For interior particles, the intermediate-density particles experience slightly larger density changes than dense particles , which is visible from the overall slightly darker colours in panel (b) and consistent with Table 3.3. This table shows the median density change across all grid cells for each region and density-class. Given the large spatial variability, the median is not necessarily the most representative metric, but it is sufficient for comparing the different regions and density-classes. The two left columns give median values for dense particles with left the positive and right the negative changes. The two right columns give median values for intermediate-density particles. For IrS- and LS-particles, both the positive and negative density changes are larger for intermediate-density particles than for dense particles in the same row; for BC-particles the values are the same. The differences are small which matches the very similar colours in the heatmaps.

Considering the presence of deep convection areas in the Irminger Sea and Labrador Sea, we would expect larger density changes in both interiors for particles that enter an interior. The strong similarity between particles classified in different regions instead suggests that the density changes seen in the maps are not primarily driven by deep convection and restratification. More likely, they reflect the degree of stratification, which is independent of the region in which a particle is classified.

Table 3.3: Median density change over all grid cells for all particles in, (top row) all regions, (second row) BC-particles, (third row) IrS-particles and (bottom row) LS-particles. The left columns show values for dense particles ($\sigma \geq 27.8$ kg/m^3 at the moment of seeding at DS) with left the positive changes (density increase) and right the negative changes (density decrease); the right columns show values for intermediate-density particles ($27.7 \leq \sigma < 27.8$ kg/m^3 at the moment of seeding at DS) with also left positive changes and right negative changes.

	Dense		Intermediate-density	
	positive	negative	positive	negative
All regions	0.0025	-0.0024	0.0028	-0.0028
Boundary Current	0.0060	-0.0057	0.0060	-0.0057
Irminger Sea	0.0032	-0.0030	0.0038	-0.0036
Labrador Sea	0.0026	-0.0026	0.0030	-0.0032

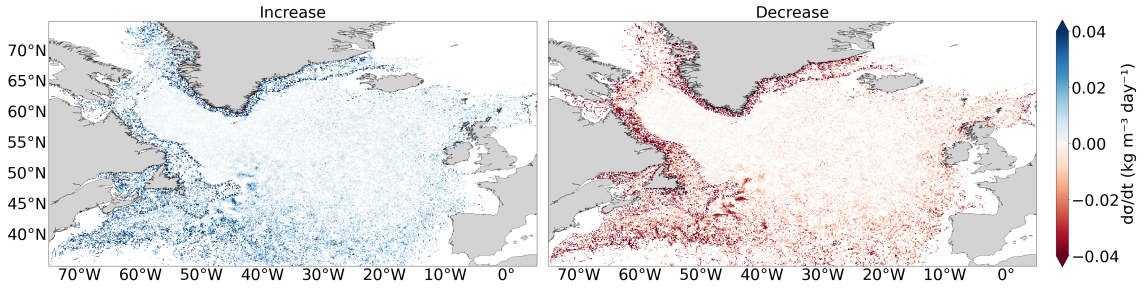

(a)

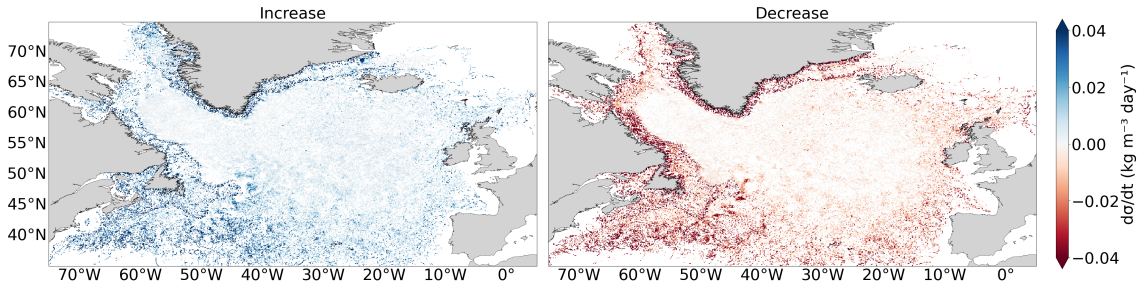

(b)

Figure 3.15: Heatmap of the changes in density in kg/m^3/day for **(a)** all dense particles ($\sigma \geq 27.8$ kg/m^3 at the moment of seeding at DS) and for **(b)** all intermediate-density particles ($27.7 \leq \sigma < 27.8$ kg/m^3 at the moment of seeding at DS). Left shows grid cells where density increases and right shows grid cells where density decreases.

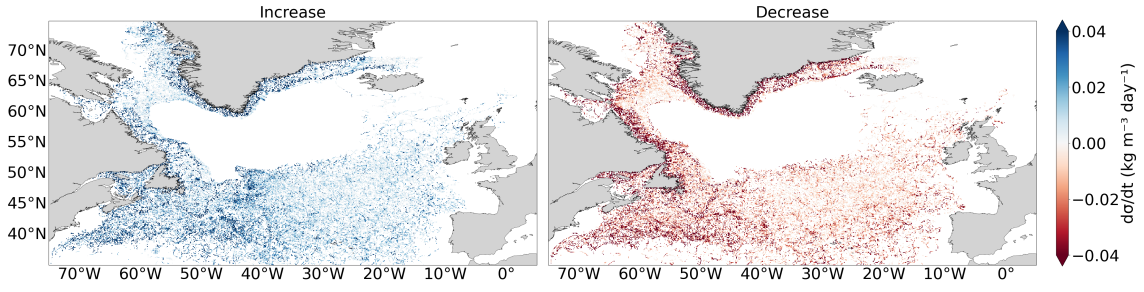

(a)

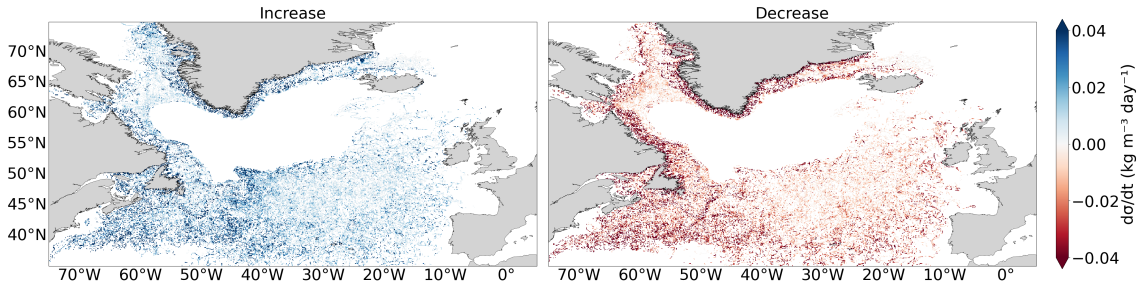

(b)

Figure 3.16: Heatmap of the changes in density in kg/m^3/day for **(a)** all dense ($\sigma \geq 27.8$ kg/m^3 at the moment of seeding at DS) BC-particles and for **(b)** all intermediate-density ($27.7 \leq \sigma < 27.8$ kg/m^3 at the moment of seeding at DS) BC-particles. Left shows grid cells where density increases and right shows grid cells where density decreases.

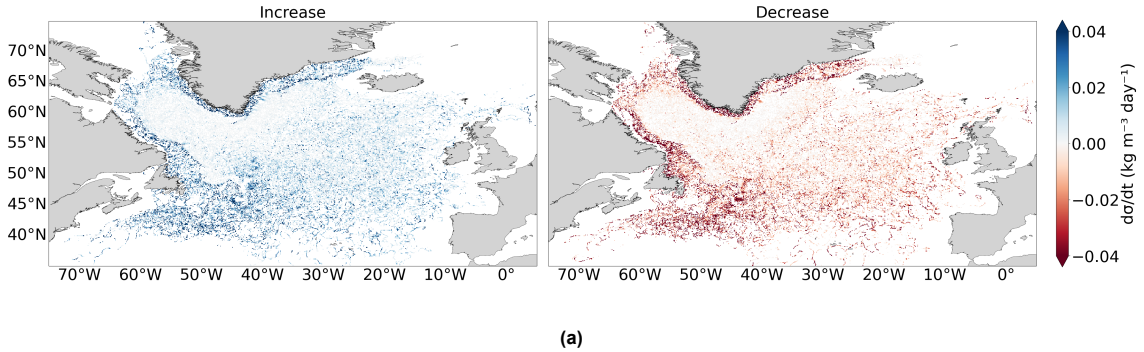

(a)

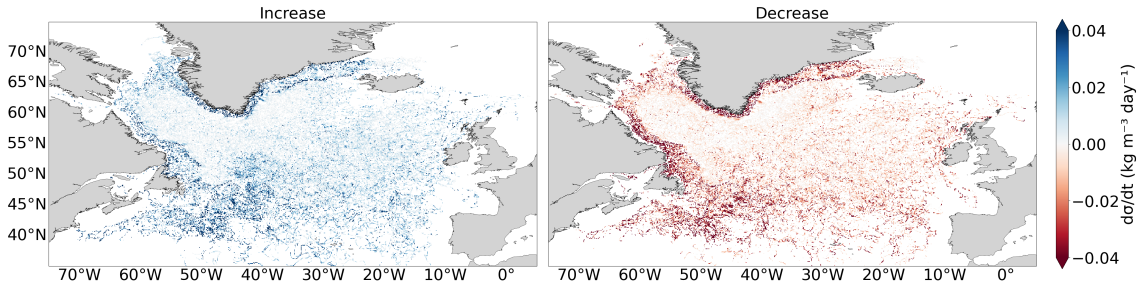

(b)

Figure 3.17: Heatmap of the changes in density in kg/m^3/day for **(a)** all dense ($\sigma \geq 27.8$ kg/m^3 at the moment of seeding at DS) IrS-particles and for **(b)** all intermediate-density ($27.7 \leq \sigma < 27.8$ kg/m^3 at the moment of seeding at DS) IrS-particles. Left shows grid cells where density increases and right shows grid cells where density decreases.

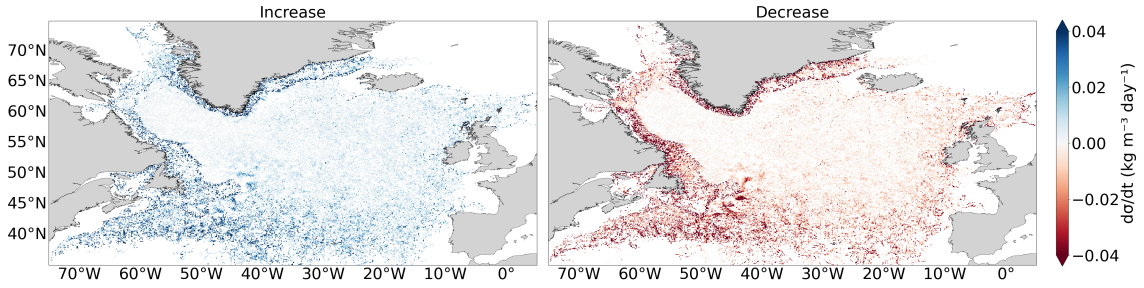

(a)

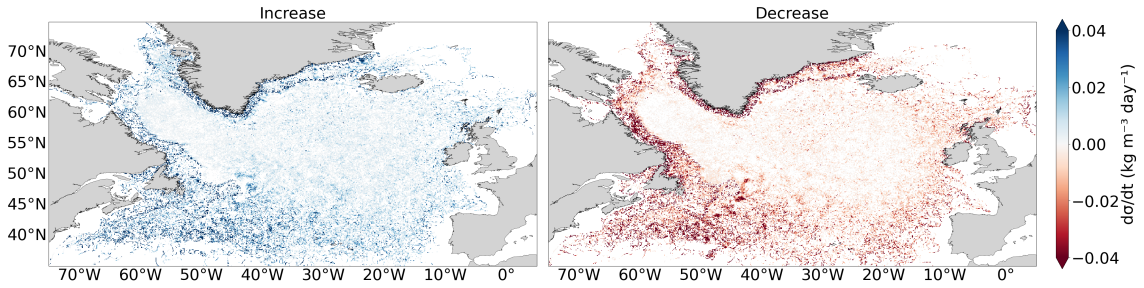

(b)

Figure 3.18: Heatmap of the changes in density in kg/m^3/day for **(a)** all dense ($\sigma \geq 27.8$ kg/m^3 at the moment of seeding at DS) LS-particles and for **(b)** all intermediate-density ($27.7 \leq \sigma < 27.8$ kg/m^3 at the moment of seeding at DS) LS-particles. Left shows grid cells where density increases and right shows grid cells where density decreases.

4

Discussion

4.1. Improvements for Methodology

In this section we discuss several choices made during the simulation setup. These include the seeding strategy, interpolation methods, kernels and selecting particles in our analysis. We discuss possible effects on the results and suggest ways they could be improved in future work.

The horizontal and vertical spacing between seeding points is based on literature that also performs Lagrangian particle tracking (Koszalka et al., 2013; Saberi et al., 2020; Georgiou et al., 2021). Ideally, we would do a sensitivity analysis to find the best spacing; the smaller the spacing, the more particles to seed. At a certain spacing and number of particles the results do not change any more. This would be the ideal spacing. However in view of time, this was not realistic.

How we defined the kernels and interpolation methods can also be improved. Instead of using linear interpolation for w-velocity, temperature, salinity and density, it might be better to use the "linear_invdist_land_tracer" interpolation method. This is a built-in interpolation method in Ocean Parcels that according to the description of OceanParcels (2025a) uses "linear interpolation except near land where the field value is zero. In that case, inverse distance weighting interpolation is computed, weighting by squares of the distance." This way the zero-values of the fields at the land and below the bathymetry are weighted less strongly and temperature, salinity, density and w-velocity close to bathymetry will be based more on physical values instead of zero-values. During our analysis we have seen particles with extremely low temperature, salinity and density. This can be a consequence of using the linear interpolation method which gives the same weight to the field-values in the ocean as the zero-values on land. These particles with temperature, salinity and density unrealistically close to zero, effect the evolution of these three variables. The temperature is represented to cold, the salinity to low and the density to buoyant. Also the spread we observe in these variables can be represented to large. Using the weighted interpolation close to the bathymetry could help to reduce some of the extremely low values.

We still advice to use the free slip interpolation method for u- and v-velocity and to define an additional kernel to prevent particles form getting stuck. The free slip interpolation makes particles slide along the bathymetry without feeling resistance. However, it does not prevent particles from being advected below the bathymetry from one time step to another time step in the simulation. If at one time step a particle is close to the bathymetry and has a velocity towards the bathymetry, it can happen that at the next time step this particle ends up below the bathymetry. To prevent this, it would be best to write a kernel. One could think of a similar approach as the kernel we wrote for particles that end up above the ocean surface and place the particle back in the ocean ten centimetres above the bathymetry. The particles that get stuck affect both the distribution of particles across regions and the particle concentration maps. Because most stuck particles get stuck on the east Greenland shelf, they are classified as BC-particles. If these particles had continued to flow, some of them might have entered an interior, which would have increased the percentages in the interiors and lowered the percentage in the boundary current. Particles that get stuck on the west Greenland shelf or along the Labrador coast do have

a chance to enter an interior, but fewer particles get stuck there compared to the east Greenland shelf. Stuck particles also influences the concentration maps, since concentrations are calculated relative to all released particles. Once particles gets stuck in the EGC, EGCC or WGC, the remaining moving particles represent a smaller fraction of the total release, decreasing the resulting concentrations downstream.

As could be seen from Figure 2.4 a percentage of the particles released also travels to the north-east of the transect before crossing the zonal section and going into the SPNA. Although we consider these particles in our analysis, they are not part of the overflow at the moment of seeding according to literature, as these particles do not have a south-eastward velocity. We however still took them into our analysis because attempts to filter on flow-velocity were unsuccessful. This can influence the results because the recirculating water can mix with ambient waters, such as fresh polar water and warm Irminger Current water (Koszalka et al., 2013). This mixing can change the temperature and salinity of the particles, and therefore their density and the pathways they follow. Recirculating particles may become warmer and fresher, which makes them more buoyant than they would have been if they had crossed the sill directly. This can also increase the number of particles that move onto the east Greenland shelf, which may partly explain why we find such a strong concentration of particles in the EGCC compared to other Lagrangian studies of DSOW where virtually non of the particles get entrained into the EGCC (Saberi et al., 2020; Koszalka et al., 2013). It can also be seen from the concentration maps in Figure A.1 and the concentration difference plot (Figure 3.1 that a higher percentage of intermediate-density particles follows the EGCC. Dense particles follow more the shelf break EGC but are also present in the EGCC. Taking into account that then 27.8 kg/m^3 above the shelf has approximately the same depth in the model data used as in observations it might have been better to track only particles denser than 27.8 kg/m^3 and not all the particles denser than 27.7 kg/m^3 as in this study.

Also our criterion that particles are left out of the analysis if their final position is to the north-east of the transect can be improved. There are a few particles that go all the way around Iceland in clockwise direction and continue southward. They enter the SPNA between Iceland and Scotland so they are not part of DSOW but because their final position is not to the north-east of the transect they are part of our analysis. To not include these particles in our analysis one could think about checking where particles enter the SPNA. If particles enter the SPNA between Greenland and Iceland then they are part of our analysis and if particles enter between Iceland and the UK they are not. Or one could take the Reykjanes Ridge, if particles enter the SPNA to the north-west of the ridge then they are part of our analysis, if the enter the SPNA to the south-east of the ridge they are not.

4.2. How are Particles Distributed over Pathways

The highest percentage of particles is found in the Boundary Current (72%). The second largest group is particles that enter the Labrador Sea interior as first interior (23%). The third group is particles that enter the Irminger Sea interior as first interior (4.4%), and the smallest group is particles that as first interior enter the Iceland Basin (0.15%). As discussed in section 3.1, the small number of IcB-particles is largely a consequence of our definition of interior particles which classifies particles based on the first interior they enter for at least 20 consecutive days. In order to be classified as IcB-particle, a particle must remain in the boundary current without entering the Irminger Sea and Labrador Sea interior for more than 20 days. Combined with the simulation period of three years, which is short to finish the full travel from DS to the Iceland Basin, only a very small fraction of particles is classified as IcB-particle.

A high percentage of the interior particles is also present in the boundary current. It might therefore be better to use a different categorisation of boundary current and interior particles. One could for example think of the categories where particles stay in the boundary current, where particles enter an interior and then rejoin the boundary current or where particles enter an interior and do not rejoin the boundary current. This could give a better overview of how particles that enter an interior spread afterwards.

Also the choice to take the -22 Sv barotropic streamline as the border between the boundary current and the interiors plays an important role in determining if particles are categorised as boundary current or as interior particle. The -22 Sv barotropic streamline we chose in this study counts a small part of the Irminger Sea interior to the boundary current domain meaning that particles have to travel further offshore to reach the Irminger Sea interior. In the Labrador Sea a small part of the WGC and LC are

cut off and counted into the interior. This means that, although particles stay in the boundary current, they might be classified as LS-particle. By taking a less negative number, the streamline shifts closer to the coast and the interior region gets larger. This could be useful in the Irminger Sea, where the -22 Sv streamline cuts off a small part from the interior. However, this would also mean that part of the WGC and the LC are considered as Labrador Sea interior. This can make it easier for particles to enter an interior so more particles are classified as interior particle and fewer as boundary current particle. Since in the Labrador Sea part of the boundary current will be counted as interior, the effect would be largest there. By taking a more negative number, the streamline moves more offshore and the opposite will happen. A larger part of the Irminger Sea interior is counted as boundary current and especially in the Labrador Sea less particles will be classified as interior particles because less of the WGC and LC are considered as Labrador Sea interior. Particles that do enter an interior in this case, have to travel further offshore, which might make them more likely to stay in the interior or enter another interior rather than re-enter the boundary current.

The particle concentration maps in this study show the percentage of particles that passed through each grid cell at least once. This highlights the main pathways of overflow water through the SPNA. However, if we instead counted the number of visits to each grid cell, the resulting maps would likely look different. Regions where particles recirculate or experience slower flow, such as basin interiors and troughs, would show higher intensities because particles can pass through the same grid cell multiple times. In contrast, regions where particles move rapidly downstream, such as the boundary current, would appear less dominant. Such an approach could therefore provide more insight into residence times and retention areas of DSOW, whereas the approach used in this study is more suitable to identify the overall spatial distribution of DSOW pathways in the SPNA.

The highest percentage of particles is categorised as boundary current particles. From literature it is known that on a large scale ocean currents are steered by bathymetry (Gille & Llewellyn Smith, 2003). More precisely, according to the Taylor-Proudman theorem water follows contours of constant f/H, where f is the Coriolis parameter and H is the ocean depth (Gille et al., 2015). Particles that at DS are released on the east Greenland shelf will tend to stay on the shelf. In order to get off the shelf, particles would need to overcome a big change in H which is dynamically difficult as f only changes a little bit on this scale. Locally, water can go off the shelf for example in the East Greenland Spill Jet (von Appen et al., 2014) and off the West Greenland shelf (Marson et al., 2017) since on a small scale, other forces as friction and turbulence can play an important role and the flow can be ageostrophic. A second reason why the boundary current is the largest group can be related to the location where most particles get stuck as already discussed in section 4.1.

The second largest group of particles enters the Labrador Sea interior as first interior. This can be explained by differences in eddy activity in the Irminger Sea and Labrador Sea. Recall that in the Irminger Sea eddies mainly form from baroclinic instabilities in the Irminger Current, that they have an average radius of 6 km, an average maximum velocity of 0.1 m s^{-1} and that they peak in summer (Fan et al., 2013; Sterl and de Jong, 2022). In the Labrador Sea there are three types of eddies observed, forming from both baroclinic and barotropic instabilities, they have an average radius between 5 and 30 km, an average maximum velocity of 0.1 to 0.8 m s^{-1} and they peak in winter (Lilly et al., 2003; Katsman et al., 2004; Gelderloos et al., 2011; Rieck et al., 2019). As there are several types of eddies in the Labrador Sea that have a larger average radius and maximum velocity, these eddies can be more effective in shedding water into the interior than eddies in the Irminger Sea, resulting in more particles entering the Labrador Sea interior than the Irminger Sea interior. Two additional factors may also play a role in explaining why more particles enter the Labrador Sea interior than the Irminger Sea interior. First, the location of the −22 Sv streamline affects how easily water is classified as interior. In the Labrador Sea the streamline is very close to the boundary current, so water does not need to be shed far into the interior to be considered interior, whereas in the Irminger Sea particles have to move further away from the boundary current. Second, our criterion of requiring at least twenty consecutive days in the interior can influence how easily a particle can count as interior particle. In the Irminger Sea, particles have to travel further before they count as interior than in the Labrador Sea. It takes particles more time to reach the Irminger Sea interior than the Labrador Sea interior so that short excursions into the Labrador Sea interior occur more often than in the Irminger Sea. The particles that do reach the Irminger Sea interior however had to do more effort to reach the interior and might be more likely to stay there for longer times.

In initialisation months June and December, a higher percentage of released particles is dense, while in September and March a higher percentage of particles is of intermediate-density. For September this is expected since 41% of the particles is seeded on the shelf as seen from Figure 2.3b. These particles are at shallower depth and therefore more buoyant. Moreover, we expect the water in September to be more buoyant because it is the end of summer. The sea temperature is high and the sea ice concentration, and hence brine rejection, is low. Also for December we expect that a higher percentage of particles is dense. It is the beginning of winter so waters start to get colder and denser, also sea ice starts to form so that brine rejection results in more saline and dense water. One would expect this to be most visible on the shelf as most sea ice forms there and only weakly affect the deeper overflow layer, which is more influenced by processes acting on the sources of DSOW in the Nordic Seas. An example is the passage of pulses in winter which increase the dense water transport over the sill. In summer the passage of boluses increase the dense water transport which can result in a higher percentage of particles in June to be dense at the moment of release at DS. However, we do not expect a higher percentage of intermediate-density particles in March. In March one would expect more dense water since it is end of winter, the sea temperatures are lowest, the sea ice concentration is highest and most brine is rejected, both locally and in the Nordic Seas. The hydrographic sections in Figure 2.2 show however relatively warm water on the sill in March which could explain the higher percentage of intermediate-density particles. June shows indeed a shallow 27.8 kg/m^3 isopycnal over the sill with a cold overflow that corresponds to a thickening in the overflow layer and the passage of cold water lenses due to boluses (Almansi et al., 2017). In September the depth of the isopycnal is approximately the same on the sill as on the shelf indicating a relative high percentage of particles being released on the shelf. In December and March the isopycnal is located deeper where in March we see the relatively warm overflow.

4.3. Evolution of Temperature, Salinity and Density

4.3.1. T,S diagrams

From the T,S diagram in Figure 3.8 we observe that BC-particles experience larger changes in median temperature, salinity, density and depth than IrS- and LS-particles. The histograms in Figure 3.13 show the same pattern where BC-particles have the widest ranges in temperature, salinity, density and depth, while interior particles show narrower distributions. For BC-particles, dense and intermediate-density particles show similar ranges, whereas in the interior intermediate-density particles span broader ranges and peak at different values than dense particles.

These differences can be explained from physical processes that differ for BC- and interior particles. The boundary current around the Irminger Sea and Labrador Sea cools and freshens as it flows cyclonically around the SPG and is joined by fresh polar-origin outflows (Yashayaev & Clarke, 2008). It is also “strongly baroclinic with rapid transition between the less-saline waters over the shelves and the more-saline waters over the deep basins” (Yashayaev, 2007). Consequently, BC-particles can undergo large changes in temperature and salinity when they move between these contrasting water masses. A second factor is atmospheric interaction. Near the Labrador Coast and in the NAC the median depth of BC-particles becomes shallower than 40 meters, allowing atmospheric heat and freshwater fluxes to directly influence water properties (Evans et al., 2023). The histograms also shows that a large fraction of BC-particles, both dense and intermediate-density, is located very shallow. Third, BC-particles travel along steep topographic slopes where strong shear and eddy activity enhance mixing (Brüggemann & Katsman, 2019). Together, these factors explain the wide ranges in temperature, salinity, density and depth observed for BC-particles.

Particles that enter an interior, especially the deeper located dense particles, are less exposed to this big variability. Concentration maps show that interior particles are also present in the boundary current but they are mainly found in the shelf break current and less in the coastal current on the shelf. Hence they experience smaller changes than BC-particles that travel between the coastal current and shelf break current. Furthermore, interior particles that remain in the interior are less exposed to steep topographic slopes than BC-particles. Note however that a high percentage of particles that enter an interior later return to the boundary current and can thus be exposed to the same steep topographic slopes and the related mixing. Interaction with the atmosphere can also play a role. For particles entering an interior most of the dense particles are located deeper than 110 m and show smaller ranges in temperature,

salinity and sigma corresponding to weaker mixing and less air-sea exchange. Intermediate-density interior particles are located shallower and show bigger ranges than the dense interior particles but they are located deeper and show smaller ranges than the BC-particles. The shallowest intermediate-density water can probably be related with the peaks we see of less dense water, with lower salinity and higher temperature. Finally, about 40% of LS-particles has a very shallow between 0 and 20 m depth. This may reflect particles that stay in the boundary current but that are counted as LS-particles because part of the WGC and LC is cut off by the -22 Sv barotropic stream line and is considered as LS-interior.

The temperature histograms show two distinct peaks and relatively few particles in between. This likely reflects two water masses that carry most of the particles: a colder, fresher water mass of polar origin and a warmer, saltier Atlantic-origin water mass. For interior particles, the two peaks may also be associated with whether particles remain in the interior or re-enter the boundary current. This means that the median temperature in the T,S diagrams may not be the most representative value, because it can fall in the range between the two peaks where only a small fraction of the particles is found. In contrast, salinity for interior particles shows a narrow range, suggesting that a relatively coherent water mass with this salinity is formed in the Irminger Sea and Labrador Seas which subsequently experiences limited mixing with surrounding waters. For salinity, the median value in the T,S diagrams is therefore more representative than for temperature.

In the T,S diagrams we observe that LS-particles have slightly higher median temperature and lower median salinity compared to IrS-particles. This also appears from the histograms and could be explained from the locations where the LS-particles have a higher concentration than the IrS-particles. Figures 3.11b and c and 3.12b and c show that a higher percentage of LS-particles in the EGCC and NAC. The EGCC is a fresh current which could result in a slightly lower median salinity for LS-particles than for IrS-particles. More particles in the NAC can result in a slightly higher temperature but since it is also a high salinity current it can also result in more saline water instead of the fresher water we observe now. A second explanation could be that, according to de Jong and de Steur (2016) and Grist et al. (2015) winter cooling is more pronounced in the eastern part of the SPG east of Greenland so that a stronger cooling is expected in the Irminger Sea interior. On the other hand, Chafik et al. (2022) states that the Labrador Sea is the region of largest heat losses and that waters in the Irminger Sea are primarily cooled in the Labrador Sea before they are exported east towards the Irminger Sea with the SPG.

Finally, the T,S evolution is plotted as function of time since release, which highlights spatial variability but hides temporal or seasonal variability. Using absolute time instead could allow changes in properties to be linked more directly to the time of year at which they occur. Such an approach could show seasonal signals such as deep convection, which would result in deeper and colder particles in winter, or summer restratification, if particles are located in an interior and increase their temperature.

4.3.2. Density Change Heatmaps

Different from the T,S diagrams which show the temporal evolution of density, the density change heatmaps highlight the spatial variability of density changes. From the maps in Figures 3.15 – 3.18 we saw that particles experience the largest density changes in the boundary current. This is true also for IrS- and LS-particles and for both dense and intermediate-density particles. The median values in 3.3 confirm this: BC-particles show the largest changes with similar magnitude for dense and intermediate-density particles, whereas IrS- and LS-particle experience smaller changes overall, with intermediate-density particles showing slightly larger changes than dense particles. What stands out is that the heatmaps for the different particle regions and both density-classes are remarkably similar in both pattern and magnitude. Taken together, this suggests that the density changes shown in the maps reflect less the processes that actively modify density such as deep convection and restratification but instead primarily represent the degree of stratification.

As discussed earlier, the boundary current is strongly baroclinic (Yashayaev, 2007) and therefore strongly stratified. Particles in the boundary current can experience large density changes with only a relatively small change in depth if they move between the different water massses. This likely explains why the largest density changes take place in the boundary current for both BC-, IrS- and LS-particles. For BC-particles, tha magnitude of density change is similar for dense and intermediate-density parti-

cles. Since both groups are found at approximately the same depths (Figure 3.13d), they are exposed to similar eddies and mixing processes and therefore undergo comparable density changes.

For IrS- and LS-particles, intermediate-density particles are located shallower than dense particles (Figure 3.13d). We expect the deeper located dense particles to be in more stable layers that are less affected by eddies and mixing, whereas the shallower intermediate-density particles are more strongly influenced by these processes. Nevertheless, the depth ranges of the two density-classes overlap, meaning that both are exposed to the same mixing. As a result, the density changes are similar for both classes, with intermediate-density particles showing slightly larger changes overall.

A clear decrease in density is visible in the upstream half of the Kangerlussuaq Trough, especially for intermediate-density particles. Although polar-origin water and glacial meltwater are present along the entire Greenland shelf, the trough topography may enhance the mixing and entrainment of the overlying fresh layer into the overflow, leading to a locally stronger freshening signal.

The density change heatmaps showed the largest changes in the boundary current and much smaller changes in the interior. Given that the T,S diagrams in section 3.2 show shallow median depths within the mixed layer and considering the deep convection areas in the Irminger Sea and Labrador Sea, we would expect higher density change values in the interior than those shown in Figure 3.15 to 3.18. The relatively small density changes in the interior may partly result from taking the median over the full three year simulation, which smooths out possible seasonal signals. In addition, the heatmaps use relative time, meaning that particles released in different seasons can contribute to the same relative timestep which further averages out seasonal variablity. To examine whether density change patterns vary seasonally, one could make heatmaps per season and based on date and time rather than relative time.

5

Conclusion and Recommendations

5.1. Conclusions

The goal of this thesis was to find main pathways along which Denmark Strait Overflow Water spreads in the Subpolar North Atlantic and how density, temperature and salinity change along these pathways.

Denmark Strait Overflow Water spreads over the entire Subpolar North Atlantic via both the boundary current and pathways via the interior. The largest fraction of particles, 72%, stays in the boundary current. The other 28% of the particles enters one of the interiors of the Labrador Sea, the Irminger Sea or the Iceland Basin. Of the interiors, the Labrador Sea interior is entered most often as first interior with 23% of the particles, 4.4% of the particles enters the Irminger Sea interior as first interior and only 0.15% of the particles enters the Iceland Basin as first interior. This aligns with our expectations from previous studies where particles are found to spread and exit the SPNA via both the boundary current and interior pathways (Lozier et al., 2022; Georgiou et al., 2021). We observed that a higher percentage of dense particles (potential density higher than 27.8 kg/m^3 at DS) enters an interior and that a higher percentage of intermediate-density particles (potential density between 27.7 and 27.8 kg.m^3 at DS) stays in the boundary current; especially we find a higher percentage of intermediate-density particles in the East Greenland Coastal Current. For each of the four months that particles were released, a higher percentage of particles stays in the boundary current than that particles enter an interior although the percentages vary per month of release. The percentage of particles entering an interior is highest for particles released in March, 64% in the boundary current and 36% in the interior of which 30% in the Labrador Sea. Since in winter the density gradient between boundary current and interior is largest and eddy activity in the Labrador Sea peaks (Katsman et al., 2004; Rieck et al., 2019) it is expected to have the highest percentage of particles that enter an interior in March.

The overflow we are analysing mixes with saltier and warmer ambient water from the SPNA. This is seen in an overall salinisation and warming of the particles over time. The biggest changes in median temperature, salinity, density and depth are seen for particles that stay in the boundary current (BC-particles). After entering the SPNA a large fraction of these particles mix with the fresh East Greenland Coastal Current and experience a strong diapycnal density decrease due to freshening. As they continue further into the SPNA, especially when they continue into the North Atlantic Current, the particles experience a strong isopycnal increase in temperature and salinity. Particles that enter an interior experience smaller changes changes in temperature, salinity density and depth than particles that stay in the boundary current. They mainly experience an increase in temperature and a small increase in salinity but much smaller than the particles that stay in the boundary current. This behaviour is consistent with the spread in these properties where BC-particles occupy the widest ranges in all four properties with dense and intermediate-density particles showing very similar distributions. Interior particles, on the other hand, display narrower ranges and clearer differences between dense and intermediate-density particles. For both boundary current and interior particles the temperature distribution reveals two peaks around which particles are concentrated. They likely reflect the presence of both polar-origin and Atlantic-origin water. For interior particles, it might also reflect particles that remain in the interior

and particles that rejoin the boundary current. In the distribution of salinity we see a uniform distribution for BC-particles, while interior particles are concentrated around one relatively narrow peak, indicating the formation of a coherent water mass in the interior.

Looking into the spatial variability in density changes, particles experience the largest changes at the margins of the research area, in the East Greenland Current and East Greenland Coastal Current, in the West Greenland Current, in the Labrador Sea and in the North Atlantic Current; much less density change is seen in the interiors of the Irminger Sea, Labrador Sea and Iceland Basin. Taking into account the deep convection areas in the Irminger Sea and Labrador Sea, one would expect to see more density changes in the interior than we do now, especially when taking into account the shallow median depth of maximum 310 m which is well within the mixed layer depth of both interiors (Fröb et al., 2016; Yashayaev, 2024). However, the density change heatmaps likely reflect the regional degree of stratification rather than processes such as deep convection and restratification. This also explains why the spatial patterns are so similar for particles classified in different regions and for different density-classes; the degree of stratification is largely the same, regardless of in which region particles are classified.

5.2. Recommendations

We saw that the interiors of the Labrador Sea, Irminger Sea and Iceland Basin are connected. It would be interesting to examine via which pathways and in which direction the interiors are connected. Possible questions include: Do particles move between interiors mainly via interior pathways or via the boundary current? Is the flow mainly from the Irminger Sea towards the Labrador Sea and/or Iceland Basin, from the Labrador Sea towards the Irminger Sea and/or Iceland Basin or from the Iceland Basin towards the Labrador Sea and/or Irminger Sea? Given the concentration maps, we expect interior exchange to occur in multiple directions. The presence of both IrS- and LS-particles in the other basin suggests that DSOW may flow from the Labrador Sea interior toward the Irminger Sea interior and vice versa. For the Iceland Basin, we expect that it mainly receives DSOW from the Irminger Sea and Labrador Sea within the three-year simulation. Over a longer simulation, a larger fraction of particles may reach the Iceland Basin which could provide insight into their subsequent pathways. This exchange may also be linked to differences in particle density and depth. If multiple connections are found, are some preferred by particles within particular density or depth ranges? To better investigate interior pathways, it is recommended to refine the classification of boundary current and interior particles. We observed a high percentage of interior particles in the boundary current. Therefore, we advise defining different categories such as: particles that remain in the boundary current; particles that enter one interior and then rejoin the boundary current; particles that enter one interior, follow the boundary current and then enter another interior; particles that enter an interior and do not return back to the boundary current; and particles that move from one interior to another via interior pathways.

A second unanswered question concerns the travel time along different pathways. Travel times play an important role in determining to what extent DSOW properties such as temperature, salinity and density, can change. For longer residence times, particles experience enhanced exposure to mixing, (deep) convection and surface fluxes, as they have more time to interact with these processes compared to particles with a short residence time. Quantifying pathway-specific travel times would also help to understand how quickly signals from the overflow can propagate downstream through the SPNA and to what extent they can be modified by local processes such as mixing or restratification. To get reliable travel times, we advice to write a kernel that prevents particles from getting stuck on the bathymetry e.g. by placing particles that are advected below the bathymetry, back in the ocean several centimetres above the bathymetry. This would not only lead to more realistic travel times, but also prevent decreases in particle concentrations further downstream and could alter the distribution of particles between boundary current and interior regions, as discussed in chapter 4.

While using time since release is useful for determining travel times along pathways and temporal evolution in properties such as temperature, salinity, density and depth, it is not sufficient to identify seasonal signals in these properties. To capture such temporal variability, a different definition of time could be more appropriate. We therefore recommend using the actual date and time of a particle instead. This would allow seasonal differences to appear more clearly in the average or median temperature, salinity, density and depth at each time step. When colouring the T,S evolution by average or median depth in

T,S diagrams, one would then expect to see greater depths during winter when deep convection takes place. To identify regions with strong density changes, density change heatmaps could be used as in this study. However, instead of taking the median density change over all three years, we recommend calculating the median density change for each season separately. This approach would make it possible to highlight regions of strong density changes associated with deep convection during winter and restratification during summer.

Moreover, we observed a different spreading of dense and intermediate-density particles. Considering that climate change is likely to affect deep water formation and thus the production and possible the density of DSOW, future work could explore how these pathways change under different climate conditions. In the Nordic Seas, an increased inflow of freshwater from enhanced ice melt and precipitation, together with a reduced inflow of Atlantic-origin water under a weaker AMOC, is expected to decrease surface salinity in the Nordic Seas (Madan et al., 2024). Combined with higher atmospheric temperatures and reduced winter cooling, these factors would lower seawater density and potentially weaken downwelling and deep convection, resulting in a reduced supply of dense overflow water. Because Earth's climate system is highly complex, it is difficult to predict the effect of these changes on DSOW formation and spreading. We therefore recommend performing a similar analysis as in this study using a perturbed climate system. The Global Ocean Physics Analysis and Forecast system cannot simulate such scenarios, so a different model framework should be used such as NEMO or CMIP models. CMIP models compute velocity and tracer fields under different climate scenarios and provide them as output but they are generally limited by their coarse resolution of 1°. In contrast, NEMO can be run at a much finer resolution, although it requires more extensive setup and computational power, as velocity and tracer fields need to be self-computed. To distinguish between processes on the shelf and around the shelf break we recommend a resolution of at least 1/6°but preferably higher such as 1/9° or 1/12°. Further, we suggest to use the SSP2-4.5 climate scenario also know as the "middle of the road' scenario because it currently represents the most likely emissions trajectory given global emission and policy trends (Hausfather & Peters, 2020).

Finally, as this study is based on model data, it would be valuable to assess how well the simulated pathways and water mass transformations agree with observations. Observational datasets such as Argo floats, moorings, and ship-based hydrographic sections could be used to evaluate DSOW pathways and water properties in the subpolar North Atlantic. Each of these observation types has advantages and limitations. Argo and Deep Argo floats provide broad spatial coverage and are well suited to study large-scale variability in temperature, salinity, and density. However, their temporal resolution is relatively low. Moorings, such as those from the OSNAP array, offer high temporal resolution and direct velocity time series, but are limited to specific locations. Ship-based hydrographic sections provide detailed vertical profiles and high spatial resolution along transects, but very low resolution in time of one or several years. To assess DSOW pathways in the SPNA, observations with broad spatial coverage, such as Argo and Deep Argo floats, are preferred. Combining different types of observational data will offer a more complete understanding and help validate modelled DSOW pathways and transformations.

References

Abbass, K., Qasim, M. Z., Song, H., Murshed, M., Mahmood, H., & Younis, I. (2022). A review of the global climate change impacts, adaptation, and sustainable mitigation measures. *Environmental science and pollution research international*, *29*(28), 42539–42559. https://doi.org/10.1007/s11356-022-19718-6

Almansi, M., Haine, T. W. N., Pickart, R. S., Magaldi, M. G., Gelderloos, R., & Mastropole, D. (2017). High-frequency variability in the circulation and hydrography of the denmark strait overflow from a high-resolution numerical model. *Journal of Physical Oceanography*, *47*(12), 2999–3013. https://doi.org/10.1175/JPO-D-17-0129.1

Amante, C., & Eakins, B. W. (2009). *ETOPO1 1 Arc-Minute Global Relief Model: Procedures, Data Sources and Analysis* (NOAA Technical Memorandum No. NESDIS NGDC-24) (Accessed 2025-05-23). NOAA National Geophysical Data Center. https://doi.org/10.7289/V5C8276M

Bacon, S. (2002, January). *The dense overflows from the Nordic Seas into the deep North Atlantic* (Rep.). ICES MSS Vol.215 - 100 years of science under ICES. https://doi.org/10.17895/ices.pub.8741

Bacon, S., Marshall, A., Holliday, N. P., Aksenov, Y., & Dye, S. R. (2014). Seasonal variability of the east greenland coastal current. *Journal of Geophysical Research: Oceans*, *119*(6), 3967–3987. https://doi.org/https://doi.org/10.1002/2013JC009279

Behrens, E., Våge, K., Harden, B., Biastoch, A., & Böning, C. W. (2017). Composition and variability of the denmark strait overflow water in a high-resolution numerical model hindcast simulation. *Journal of Geophysical Research: Oceans*, *122*(4), 2830–2846. https://doi.org/10.1002/2016JC012158

Bower, A., Lozier, M., Gary, S., & Böning, C. (2009). Interior pathways of the north atlantic meridional overturning circulation. *Nature*, *459*, 243–247. https://doi.org/10.1038/nature07979

Bower, A., Lozier, S., Biastoch, A., Drouin, K., Foukal, N., Furey, H., Lankhorst, M., Rühs, S., & Zou, S. (2019). Lagrangian Views of the Pathways of the Atlantic Meridional Overturning Circulation. *Journal of Geophysical Research: Oceans*, *124*(8), 5313–5335. https://doi.org/10.1029/2019JC015014

Bruce, J. (1995). Eddies southwest of the denmark strait. *Deep Sea Research Part I: Oceanographic Research Papers*, *42*(1), 13–29. https://doi.org/10.1016/0967-0637(94)00040-Y

Brüggemann, N., & Katsman, C. A. (2019). Dynamics of Downwelling in an Eddying Marginal Sea: Contrasting the Eulerian and the Isopycnal Perspective. *Journal of Physical Oceanography*. https://doi.org/10.1175/JPO-D-19-0090.1

Buckley, M. W., & Marshall, J. (2016). Observations, inferences, and mechanisms of the atlantic meridional overturning circulation: A review. *Reviews of Geophysics*, *54*(1), 5–63. https://doi.org/https://doi.org/10.1002/2015RG000493

Chafik, L., Holliday, N. P., Bacon, S., & Rossby, T. (2022). Irminger sea is the center of action for subpolar amoc variability. *Geophysical Research Letters*, *49*(17). https://doi.org/10.1029/2022GL099133

Chafik, L., & Rossby, T. (2019). Volume, Heat, and Freshwater Divergences in the Subpolar North Atlantic Suggest the Nordic Seas as Key to the State of the Meridional Overturning Circulation. *Geophysical Research Letters*, *46*(9), 4799–4808. https://doi.org/10.1029/2019GL082110

Collins, M., Knutti, R., Arblaster, J., Dufresne, J.-L., Fichefet, T., Friedlingstein, P., Gao, X., Gutowski, W. J., Johns, T., Krinner, G., Shongwe, M., Tebaldi, C., Weaver, A. J., & Wehner, M. (2013). Long-term climate change: Projections, commitments and irreversibility. In T. F. Stocker, D. Qin, G.-K. Plattner, M. Tignor, S. K. Allen, J. Doschung, A. Nauels, Y. Xia, V. Bex, & P. M. Midgley (Eds.), *Climate change 2013: The physical science basis. contribution of working group i to the fifth assessment report of the intergovernmental panel on climate change* (pp. 1029–1136). Cambridge University Press. https://doi.org/10.1017/CBO9781107415324.024

Cooper, L. H. (1955). Deep water movements in the north atlantic as a link between climatic changes around iceland and biological productivity of the english channel and celtic sea. *Journal of Marine Research*, *14*(4).

Copernicus Marine Service. (2025). Global ocean physics analysis and forecast [Accessed on 2025-06-04]. https://doi.org/10.48670/moi-00016

Curry, B., Lee, C. M., Petrie, B., Moritz, R. E., & Kwok, R. (2014). Multiyear Volume, Liquid Freshwater, and Sea Ice Transports through Davis Strait, 2004–10 [Section: Journal of Physical Oceanography]. https://doi.org/10.1175/JPO-D-13-0177.1

Dai, A., Qian, T., Trenberth, K. E., & Milliman, J. D. (2009). Changes in continental freshwater discharge from 1948 to 2004. *Journal of Climate*, *22*(10), 2773–2792. https://doi.org/10.1175/2008JCLI2592.1

de Jong, M. F., Bower, A. S., & Furey, H. H. (2014). Two years of observations of warm-core anticyclones in the labrador sea and their seasonal cycle in heat and salt stratification. *Journal of Physical Oceanography*, *44*, 427–444.

de Jong, M. F., & de Steur, L. (2016). Strong winter cooling over the irminger sea in winter 2014–2015, exceptional deep convection, and the emergence of anomalously low sst. *Geophysical Research Letters*, *43*(13), 7106–7113. https://doi.org/10.1002/2016GL069596

Delandmeter, P., & van Sebille, E. (2019). The parcels v2.0 lagrangian framework: New field interpolation schemes. *Geoscientific Model Development*, *12*(8), 3571–3584. https://doi.org/10.5194/gmd-12-3571-2019

Dickson, R. R., & Brown, J. (1994). The production of north atlantic deep water: Sources, rates, and pathways. *Journal of Geophysical Research: Oceans*, *99*(C6), 12319–12341. https://doi.org/https://doi.org/10.1029/94JC00530

Duyck, E., Gelderloos, R., & de Jong, M. F. (2022). Wind-driven freshwater export at cape farewell. *Journal of Geophysical Research: Oceans*, *127*(5). https://doi.org/10.1029/2021JC018309

Ekman, V. W. (1905). On the influence of the earth's rotation on ocean-currents.

ECMWF. (n.d.). https://www.ecmwf.int/

Evans, D. G., Holliday, N. P., Bacon, S., & Le Bras, I. (2023). Mixing and air–sea buoyancy fluxes set the time-mean overturning circulation in the subpolar North Atlantic and Nordic Seas [Publisher: Copernicus GmbH]. *Ocean Science*, *19*(3), 745–768. https://doi.org/10.5194/os-19-745-2023

Fan, X., Send, U., Testor, P., Karstensen, J., & Lherminier, P. (2013). Observations of irminger sea anticyclonic eddies. *Journal of Physical Oceanography*, *43*(4), 805–823. https://doi.org/10.1175/JPO-D-11-0155.1

Fox-Kemper, B., Hewitt, H. T., Xiao, C., Aðalgeirsdóttir, G., Drijfhout, S. S., Edwards, T. L., Golledge, N. R., Hemer, M., Kopp, R. E., Krinner, G., Mix, A., Notz, D., Nowicki, S., Nurhati, I. S., Ruiz, L., Sallée, J.-B., Slangen, A. B. A., & Yu, Y. (2021). Ocean, cryosphere and sea level change. In V. Masson-Delmotte, P. Zhai, A. Pirani, S. L. Connors, C. Péan, S. Berger, N. Caud, Y. Chen, L. Goldfarb, M. I. Gomis, M. Huang, K. Leitzell, E. Lonnoy, J. B. R. Matthews, T. K. Maycock, T. Waterfield, O. Yelekçi, R. Yu, & B. Zhou (Eds.), *Climate change 2021: The physical science basis. contribution of working group i to the sixth assessment report of the intergovernmental panel on climate change* (pp. 1211–1362). Cambridge University Press. https://doi.org/10.1017/9781009157896.011

Fratantoni, P. S., & Pickart, R. S. (2007). The Western North Atlantic Shelfbreak Current System in Summer. *Journal of Physical Oceanography*. https://doi.org/10.1175/JPO3123.1

Fröb, F., Olsen, A., K. Våg and, G. W. K. M., Yashayaev, I., Jeansson, E., & Rajasakaren, B. (2016). Irminger sea deep convection injects oxygen and anthropogenic carbon to the ocean interior. *Nature Communications*, *7*. https://doi.org/10.1038/ncomms13244

Galloudec, O. L., Chune, S. L., Nouel, L., Fernandez, E., Derval, C., Tressol, M., Dussurget, R., Biardeau, A., & Tonani, M. (2025). *Roduct user manual for global ocean physical analysis and forecasting product* (tech. rep.). Copernicus Marine Environment Monitoring Service. https://doi.org/10.48670/moi-00016

Ganachaud, A., & Wunsch, C. (2003). Large-scale ocean heat and freshwater transports during the world ocean circulation experiment. *Journal of Climate*, *16*, 696–705.

Gascard, J.-C., & Clarke, R. A. (1983). The formation of labrador sea water. part ii. mesoscale and smaller-scale processes. *Journal of Physical Oceanography*, *13*(10), 1779–1797. https://doi.org/10.1175/1520-0485(1983)013<1779:TFOLSW>2.0.CO;2

Gelderloos, R., Katsman, C. A., & Drijfhout, S. S. (2011). Assessing the roles of three eddy types in restratifying the labrador sea after deep convection. *Journal of Physical Oceanography*, *41*(11), 2102–2119. https://doi.org/10.1175/JPO-D-11-054.1

Georgiou, S. (2021). *Boundary-interior exchanges controlling the labrador sea dynamics* [Doctoral dissertation, Delft Univertity of Technology]. https://doi.org/https://doi.org/10.4233/uuid:37028134-4e97-46b3-a50b-54ab2cdc25c4

Georgiou, S., Ypma, S. L., Brüggemann, N., Sayol, J.-M., van der Boog, C. G., Spence, P., Pietrzak, J. D., & Katsman, C. A. (2021). Direct and Indirect Pathways of Convected Water Masses and Their impacts on the Overturning Dynamics of the Labrador Sea. *Journal of Geophysical Research: Oceans*, *126*(1), e2020JC016654. https://doi.org/10.1029/2020JC016654

Gille, S. T., & Llewellyn Smith, S. G. (2003). Bathymetry and ocean circulation. In *Charting the secret world of the ocean floor: The gebco project 1903–2003*. International Hydrographic Organization; the Intergovernmental Oceanographic Commission of UNESCO.

Gille, S. T., Metzger, E. J., & Tokmakian, R. (2015). Seafloor Topography and Ocean Circulation. *Oceanography*, *17*(1), 47–54. https://doi.org/10.5670/oceanog.2004.66

Girton, J. B., & Sanford, T. B. (2003). Descent and Modification of the Overflow Plume in the Denmark Strait. *Journal of Physical Oceanography*. https://journals.ametsoc.org/view/journals/phoc/33/7/1520-0485_2003_033_1351_damoto_2.0.co_2.xml

Grist, J. P., Josey, S. A., Jacobs, Z. L., Marsh, R., Sinha, B., & van Sebille, E. (2015). Extreme air–sea interaction over the north atlantic subpolar gyre during the winter of 2013–2014 and its subsurface legacy. *Climate Dynamics*, *46*(11), 4027–4045. https://doi.org/10.1007/s00382-015-2819-3

Gurvan, M., Bourdallé-Badie, R., Bouttier, P.-A., Bricaud, C., Bruciaferri, D., Calvert, D., Chanut, J., Clementi, E., Coward, A., Delrosso, D., Ethé, C., Flavoni, S., Graham, T., Harle, J., Iovino, D., Lea, D., Lévy, C., Lovato, T., Martin, N., … Vancoppenolle, M. (2017, October). Nemo ocean engine. https://doi.org/10.5281/zenodo.3248739

Hadley, G. (1735). Vi. concerning the cause of the general trade-winds. *Philosophical Transactions of the Royal Society of London*, *39*(437), 58–62.

Handmann, P., Fischer, J., Visbeck, M., Karstensen, J., Biastoch, A., Böning, C., & Patara, L. (2018). The deep western boundary current in the labrador sea from observations and a high-resolution model. *Journal of Geophysical Research: Oceans*, *123*(4), 2829–2850. https://doi.org/10.1002/2017JC013702

Hansen, B., Húsgarð Larsen, K. M., Hátún, H., & Østerhus, S. (2016). A stable faroe bank channel overflow 1995–2015. *Ocean Science*, *12*(6), 1205–1220. https://doi.org/10.5194/os-12-1205-2016

Hátún, H., Eriksen, C. C., & Rhines, P. B. (2007). Buoyant eddies entering the labrador sea observed with gliders and altimetry. *Journal of Physical Oceanography*, *37*(12), 2838–2854. https://doi.org/10.1175/2007JPO3567.1

Hausfather, Z., & Peters, G. P. (2020). Emissions – the 'business as usual' story is misleading. *Nature*, *577*, 618–620. https://doi.org/10.1038/d41586-020-00177-3

Held, I. M., & Soden, B. J. (2006). Robust responses of the hydrological cycle to global warming. *Journal of Climate*, *19*(21), 5686–5699. https://doi.org/10.1175/JCLI3990.1

Higginson, S., Thompson, K. R., Huang, J., Véronneau, M., & Wright, D. G. (2011). The mean surface circulation of the North Atlantic subpolar gyre: A comparison of estimates derived from new gravity and oceanographic measurements. *Journal of Geophysical Research: Oceans*, *116*(C8). https://doi.org/10.1029/2010JC006877

Jochumsen, K., Köllner, M., Quadfasel, D., Dye, S., Rudels, B., & Valdimarsson, H. (2015). On the origin and propagation of denmark strait overflow water anomalies in the irminger basin. *Journal of Geophysical Research: Oceans*, *120*(3), 1841–1855. https://doi.org/10.1002/2014JC010397

Jochumsen, K., Moritz, M., Nunes, N., Quadfasel, D., Larsen, K. M. H., Hansen, B., Valdimarsson, H., & Jonsson, S. (2017). Revised transport estimates of the Denmark Strait overflow [Publisher: John Wiley & Sons, Ltd]. *Journal of Geophysical Research: Oceans*, *122*(4), 3434–3450. https://doi.org/10.1002/2017JC012803

Jochumsen, K., Quadfasel, D., Valdimarsson, H., & Jónsson, S. (2012). Variability of the denmark strait overflow: Moored time series from 1996–2011. *Journal of Geophysical Research: Oceans*, *117*(C12). https://doi.org/10.1029/2012JC008244

Johns, W. E., Baringer, M. O., Beal, L. M., Cunningham, S. A., Kanzow, T., Bryden, H. L., Hirschi, J. J. M., Marotzke, J., Meinen, C. S., Shaw, B., & Curry, R. (2011). Continuous, array-based estimates of atlantic ocean heat transport at 26.5°n. *Journal of Climate*, *24*(10), 2429–2449. https://doi.org/10.1175/2010JCLI3997.1

Katsman, C. A., Spall, M. A., & Pickart, R. S. (2004). Boundary current eddies and their role in the restratification of the labrador sea. *Journal of Physical Oceanography*, *34*(9), 1967–1983. https://doi.org/10.1175/1520-0485(2004)034<1967:BCEATR>2.0.CO;2

Klein, B., & Siedler, G. (1989). On the origin of the Azores Current. *Journal of Geophysical Research: Oceans*, *94*(C5), 6159–6168. https://doi.org/10.1029/JC094iC05p06159

Koszalka, I. M., Haine, T. W. N., & Magaldi, M. G. (2013). Fates and Travel Times of Denmark Strait Overflow Water in the Irminger Basin. *Journal of Physical Oceanography*. https://doi.org/10.1175/JPO-D-13-023.1

Lavender, K., Davis, R., & Owens, W. (2000). Mid-depth recirculation observed in the interior labrador and irminger seas by direct velocity measurements. *Nature*, *47*, 66–69. https://doi.org/10.1038/35024048

Lavin, A., Bryden, H. L., & Parilla, G. (1998). Meridional transport and heat flux variations in the subtropical north atlantic. *The Global atmosphere and ocean system*, *6*, 269–293.

Lazier, J. R. N., & Wright, D. G. (1993). Annual Velocity Variations in the Labrador Current. *Journal of Physical Oceanography*. Retrieved May 23, 2025, from https://journals.ametsoc.org/view/journals/phoc/23/4/1520-0485_1993_023_0659_avvitl_2_0_co_2.xml

Le Bras, I. A.-A., Straneo, F., Holte, J., de Jong, M. F., & Holliday, N. P. (2020). Rapid export of waters formed by convection near the irminger sea's western boundary. *Geophysical Research Letters*, *47*(3), e2019GL085989. https://doi.org/10.1029/2019GL085989

Le Bras, I. A.-A., Straneo, F., Holte, J., & Holliday, N. P. (2018). Seasonality of freshwater in the east greenland current system from 2014 to 2016. *Journal of Geophysical Research: Oceans*, *123*(12), 8828–8848. https://doi.org/10.1029/2018JC014511

Lellouche, J., Galloudec, O. L., Regnier, C., Gennip, S. V., Chune, S. L., Levier, B., Greiner, E., Drevillon, M., & Szczypta, C. (2025). *Quality information document* (tech. rep.). Copernicus Marine Environment Monitoring Service. https://doi.org/10.48670/moi-00016

Lilly, J. M., Rhines, P. B., Schott, F., Lavender, K., Lazier, J., Send, U., & D'Asaro, E. (2003). Observations of the labrador sea eddy field. *Progress in Oceanography*, *59*(1), 75–176. https://doi.org/10.1016/j.pocean.2003.08.013

Lin, P., Pickart, R. S., Jochumsen, K., Moore, G. W. K., Valdimarsson, H., Fristedt, T., & Pratt, L. J. (2020). Kinematic Structure and Dynamics of the Denmark Strait Overflow from Ship-Based Observations. *Journal of Physical Oceanography*. https://doi.org/10.1175/JPO-D-20-0095.1

Lozier, M. S. (2023). Overturning in the subpolar North Atlantic: A review [Publisher: Royal Society]. *Philosophical Transactions of the Royal Society A: Mathematical, Physical and Engineering Sciences*, *381*(2262), 20220191. https://doi.org/10.1098/rsta.2022.0191

Lozier, M. S., Bower, A. S., Furey, H. H., Drouin, K. L., Xu, X., & Zou, S. (2022). Overflow water pathways in the North Atlantic. *Progress in Oceanography*, *208*, 102874. https://doi.org/10.1016/j.pocean.2022.102874

Ma, Q., Shi, X., Scholz, P., Sidorenko, D., Lohmann, G., & Ionita, M. (2024). Revisiting climate impacts of an AMOC slowdown: Dependence on freshwater locations in the North Atlantic [Publisher: American Association for the Advancement of Science]. *Science Advances*, *10*(47), eadr3243. https://doi.org/10.1126/sciadv.adr3243

Madan, G., Gjermundsen, A., Iversen, S. C., & LaCasce, J. H. (2024). The weakening amoc under extreme climate change. *Climate Dynamics*, *62*, 1291–1309. https://doi.org/doi.org/10.1007/s00382-023-06957-7

Marine Regions. (n.d.). https://marineregions.org/gazetteer.php?p=details&id=2387

Marson, J. M., Myers, P. G., Hu, X., Petrie, B., Azetsu-Scott, K., & Lee, C. M. (2017). Cascading off the west greenland shelf: A numerical perspective. *Journal of Geophysical Research: Oceans*, *122*(7), 5316–5328. https://doi.org/10.1002/2017JC012801

Mastropole, D., Pickart, R. S., Valdimarsson, H., Våge, K., Jochumsen, K., & Girton, J. (2017). On the hydrography of denmark strait. *Journal of Geophysical Research: Oceans*, *122*(1), 306–321. https://doi.org/10.1002/2016JC012007

McDougall, T. J., & Barker, P. M. (2011). *Getting started with teos-10 and the gibbs seawater (gsw) oceanographic toolbox*. SCOR/IAPSO WG127.

NASA Jet Propulsion Laboratory. (2010, March). *Nasa study finds atlantic 'conveyor belt' not slowing* [Accessed: 2025-06-03]. NASA Jet Propulsion Laboratory. https://www.jpl.nasa.gov/news/nasa-study-finds-atlantic-conveyor-belt-not-slowing

NASA Ocean Motion. (n.d.). *Ocean in motion: Geostrophic flow* [Accessed: 2025-10-23]. https://oceanmotion.org/html/background/geostrophic-flow.htm

NOAA. (2024, June). What is the global ocean conveyor belt? [Accessed: 2025-06-03]. https://oceanservice.noaa.gov/facts/conveyor.html

OceanParcels. (2025a). Interpolation [Accessed on 2025-09-25]. https://docs.oceanparcels.org/en/latest/examples/tutorial_interpolation.html

OceanParcels. (2025b). Preventing stuck particles [Accessed on 2025-05-23]. https://docs.oceanparcels.org/en/latest/examples/documentation_unstuck_Agrid.html#3.-Slip-boundary-conditions

Østerhus, S., Woodgate, R., Valdimarsson, H., Turrell, B., de Steur, L., Quadfasel, D., Olsen, S. M., Moritz, M., Lee, C. M., Larsen, K. M. H., Jónsson, S., Johnson, C., Jochumsen, K., Hansen, B., Curry, B., Cunningham, S., & Berx, B. (2019). Arctic mediterranean exchanges: A consistent volume budget and trends in transports from two decades of observations. *Ocean Science*, *15*(2), 379–399. https://doi.org/10.5194/os-15-379-2019

Pickart, R. S., Torres, D. J., & Fratantoni, P. S. (2005). The East Greenland Spill Jet. *Journal of Physical Oceanography*. https://doi.org/10.1175/JPO2734.1

Pratt, L. J., & Whitehead, J. A. (2008). *Rotating hydraulics: Nonlinear topographic effects in the ocean and atmosphere*. Springer New York, NY. https://doi.org/10.1007/978-0-387-49572-9

Previdi, M., Smith, K. L., & Polvani, L. M. (2021). Arctic amplification of climate change: A review of underlying mechanisms. *Environmental Research Letters*, *16*(9). https://doi.org/10.1088/1748-9326/ac1c29

Rahmstorf, S. (2024). FEATURE ARTICLE • Is the Atlantic Overturning Circulation Approaching a Tipping Point? *Oceanography*, *37*(3), 16–29. https://doi.org/10.5670/oceanog.2024.501

Rieck, J. K., Böning, C. W., & Getzlaff, K. (2019). The nature of eddy kinetic energy in the labrador sea: Different types of mesoscale eddies, their temporal variability, and impact on deep convection. *Journal of Physical Oceanography*, *49*(8), 2075–2094. https://doi.org/10.1175/JPO-D-18-0243.1

Saberi, A., Haine, T. W. N., Gelderloos, R., Jong, M. F. d., Furey, H., & Bower, A. (2020). Lagrangian Perspective on the Origins of Denmark Strait Overflow. *Journal of Physical Oceanography*. https://doi.org/10.1175/JPO-D-19-0210.1

Sterl, M. F., & de Jong, M. F. (2022). Restratification structure and processes in the irminger sea. *Journal of Geophysical Research: Oceans*, *127*(12), e2022JC019126. https://doi.org/10.1029/2022JC019126

Stommel, H. (1958). The abyssal circulation. *Deep Sea Research (1953)*, *5*(1), 80–82. https://doi.org/10.1016/S0146-6291(58)80014-4

Stommel, H. (1961). Thermohaline convection with two stable regimes of flow. *Tellus*, *13*(2), 224–230. https://doi.org/10.1111/j.2153-3490.1961.tb00079.x

Tanhua, T., Olsson, K. A., & Jeansson, E. (2005). Formation of denmark strait overflow water and its hydro-chemical composition. *Journal of Marine Systems*, *57*(3), 264–288. https://doi.org/10.1016/j.jmarsys.2005.05.003

Tesdal, J.-E., & Haine, T. W. N. (2020). Dominant terms in the freshwater and heat budgets of the subpolar north atlantic ocean and nordic seas from 1992 to 2015. *Journal of Geophysical Research: Oceans*, *125*(10). https://doi.org/10.1029/2020JC016435

Tol, R. S. J. (2018). The economic impacts of climate change. *Review of Environmental Economics and Policy*, *12*(1), 4–25. https://doi.org/10.1093/reep/rex027

Trenberth, K. E., Caron, J. M., & Stepaniak, D. P. (2001). The atmospheric energy budget and implications for surface fluxes and ocean heat transports. *Climate Dyamics*, *17*, 259–276.

van Westen, R. M., Kliphuis, M., & Dijkstra, H. A. (2024). Physics-based early warning signal shows that AMOC is on tipping course [Publisher: American Association for the Advancement of Science]. *Science Advances*, *10*(6), eadk1189. https://doi.org/10.1126/sciadv.adk1189

van Westen, R. M., Vanderborght, E., Kliphuis, M., & Dijkstra, H. A. (2025). Physics-based indicators for the onset of an amoc collapse under climate change. *Journal of Geophysical Research: Oceans*, *130*(8), e2025JC022651. https://doi.org/10.1029/2025JC022651

Vancoppenolle, M., Bouillon, S., Fichefet, T., Goosse, H., Lecomte, O., Maqueda, M. A. M., & Madec, G. (2012). *The louvain-la-neuve sea ice model*. Note du Pôle de modélisation de l'Institut Pierre-Simon Laplace.

von Appen, W.-J., Mastropole, D., Pickart, R. S., Valdimarsson, H., Jónsson, S., & Girton, J. B. (2017). On the nature of the mesoscale variability in denmark strait. *Journal of Physical Oceanography*, *47*(3), 567–582. https://doi.org/10.1175/JPO-D-16-0127.1

von Appen, W.-J., Koszalka, I. M., Pickart, R. S., Haine, T. W., Mastropole, D., Magaldi, M. G., Valdimarsson, H., Girton, J., Jochumsen, K., & Krahmann, G. (2014). The east greenland spill jet as an important component of the atlantic meridional overturning circulation. *Deep Sea Research Part I: Oceanographic Research Papers*, *92*, 75–84. https://doi.org/10.1016/j.dsr.2014.06.002

Weijer, W., Cheng, W., Drijfhout, S. S., Fedorov, A. V., Hu, A., Jackson, L. C., Liu, W., McDonagh, E. L., Mecking, J. V., & Zhang, J. (2019). Stability of the atlantic meridional overturning circulation: A review and synthesis. *Journal of Geophysical Research: Oceans*, *124*(8), 5336–5375. https://doi.org/10.1029/2019JC015083

Whitehead, J. A. (1989a). Internal hydraulic control in rotating fluids—applications to oceans. *Geophysical & Astrophysical Fluid Dynamics*, *48*(1-3), 169–192. https://doi.org/10.1080/03091928908219532

Whitehead, J. A., Leetmaa, A., & Knox, R. (1974). Rotating hydraulics of strait and sill flows†. *Geophysical Fluid Dynamics*, *6*(2), 101–125. https://doi.org/10.1080/03091927409365790

Whitehead, J. A. (1989b). Giant ocean cataracts. *Scientific American*, *260*(2), 50–59. Retrieved June 2, 2025, from http://www.jstor.org/stable/24987139

Woods Hole Oceanographic Institution. (n.d.). *Curretns, gyres, eddies* [Accessed: 2025-10-23]. https://www.whoi.edu/ocean-learning-hub/ocean-topics/how-the-ocean-works/ocean-circulation/currents-gyres-eddies/

Xu, X., Schmitz Jr., W. J., Hurlburt, H. E., Hogan, P. J., & Chassignet, E. P. (2010). Transport of nordic seas overflow water into and within the irminger sea: An eddy-resolving simulation and observations. *Journal of Geophysical Research: Oceans*, *115*(C12). https://doi.org/10.1029/2010JC006351

Yashayaev, I. (2007). Hydrographic changes in the labrador sea, 1960–2005. *Progress in Oceanography*, *73*(3), 242–276. https://doi.org/https://doi.org/10.1016/j.pocean.2007.04.015

Yashayaev, I. (2024). Intensification and shutdown of deep convection in the labrador sea were caused by changes in atmospheric and freshwater dynamics. *Communications Earth & Environment*, *5*, 156. https://doi.org/10.1038/s43247-024-01296-9

Yashayaev, I., & Clarke, A. (2008). Evolution of north atlantic water masses inferred from labrador sea salinity series. *Oceanography*, *21*(1), 30–45. Retrieved October 13, 2025, from https://www.jstor.org/stable/24860152

A

Miscellaneous Plots

A.1. Particle Concentration Maps

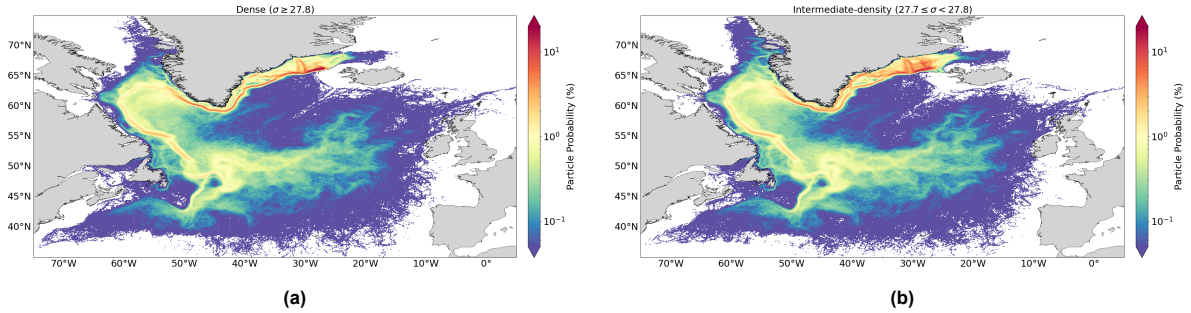

(a) **(b)**

Figure A.1: Particle concentration maps for **(a)** dense particles with an initial density at DS of 27.8 kg/m^3 or higher and **(b)** intermediate-density particles with an initial density at DS between 27.7 and 27.8 kg/m^3 as a percentage of all particles released.

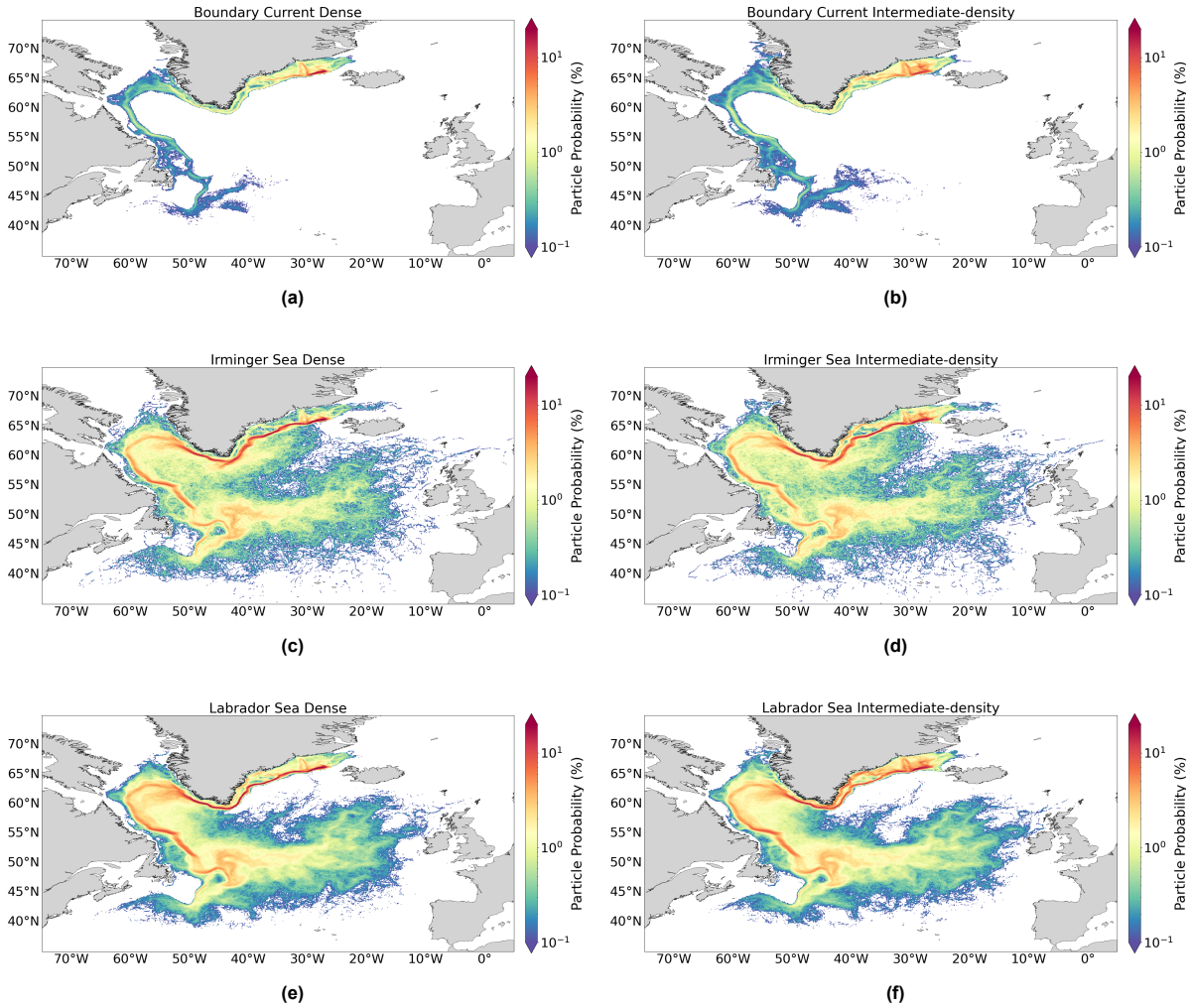

Figure A.2: Concentration plots for **(a)** all dense and **(b)** all intermediate-density particles categorised in the boundary current, **(c)** all dense and **(d)** all intermediate-density particles categorised in the Irminger Sea interior and **(e)** all dense and **(f)** all intermediate-density particles categorised in the Labrador Sea interior. Per region the particle probability is calculated as a percentage of the number of particles categorised in that region.

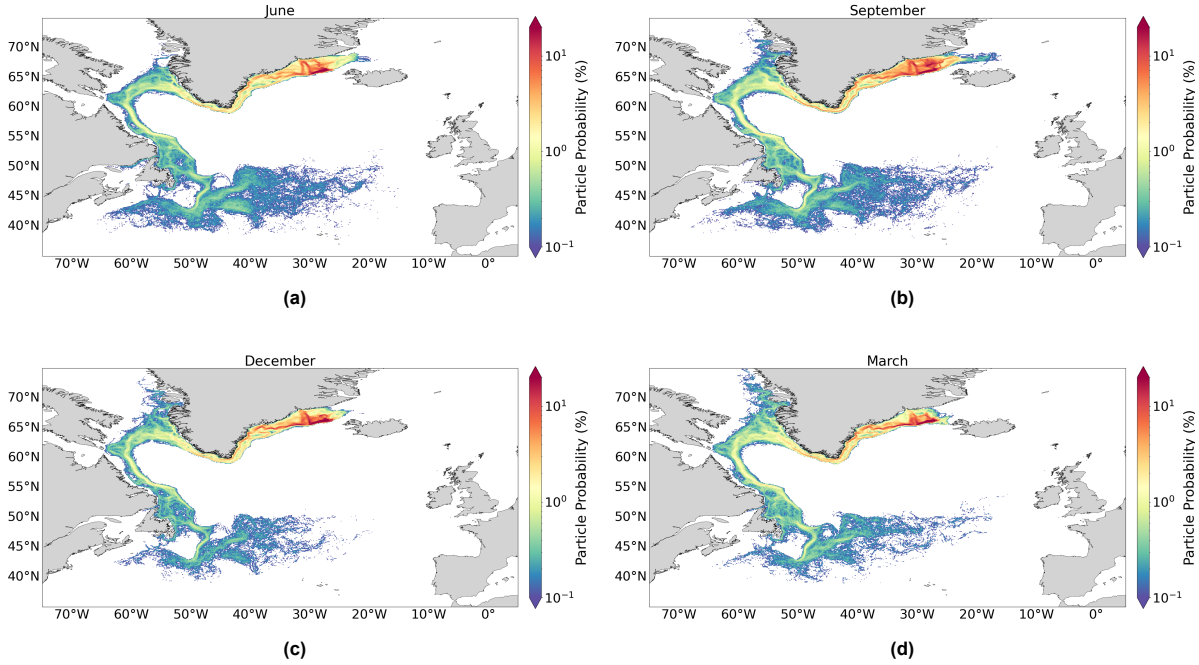

Figure A.3: Particles that stay in the boundary current and are seeded in **(a)** June '22, **(b)** September '22, **(c)** December '22 and **(d)** March '23.

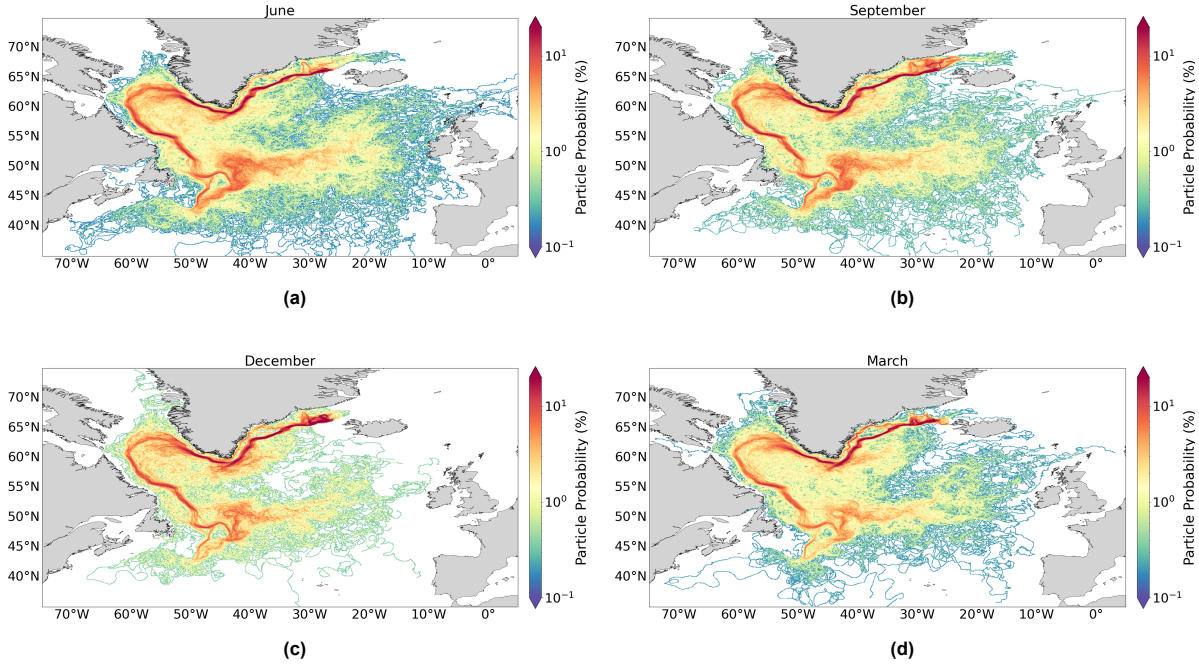

Figure A.4: Particles that enter the Irminger Sea interior as first interior and are seeded in **(a)** June '22, **(b)** September '22, **(c)** December '22 and **(d)** March '23.

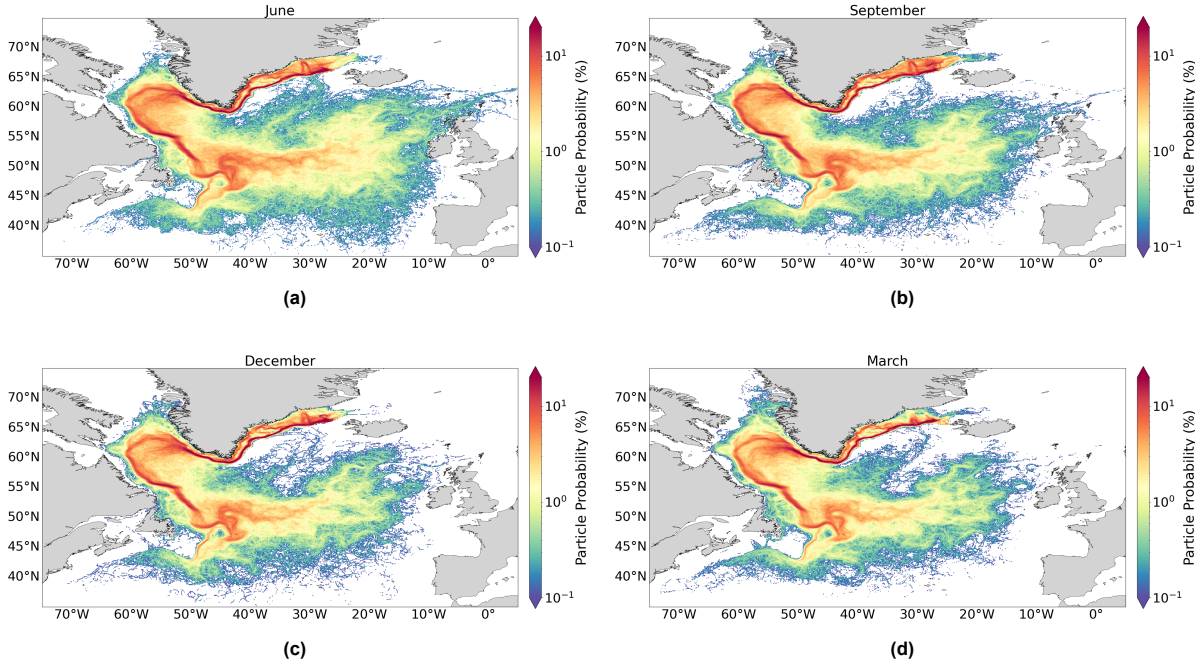

Figure A.5: Particles that enter the Labrador Sea interior as first interior and are seeded in **(a)** June ‘22, **(b)** September ‘22, **(c)** December ‘22 and **(d)** March ‘23.

A.2. T,S Diagrams per Season

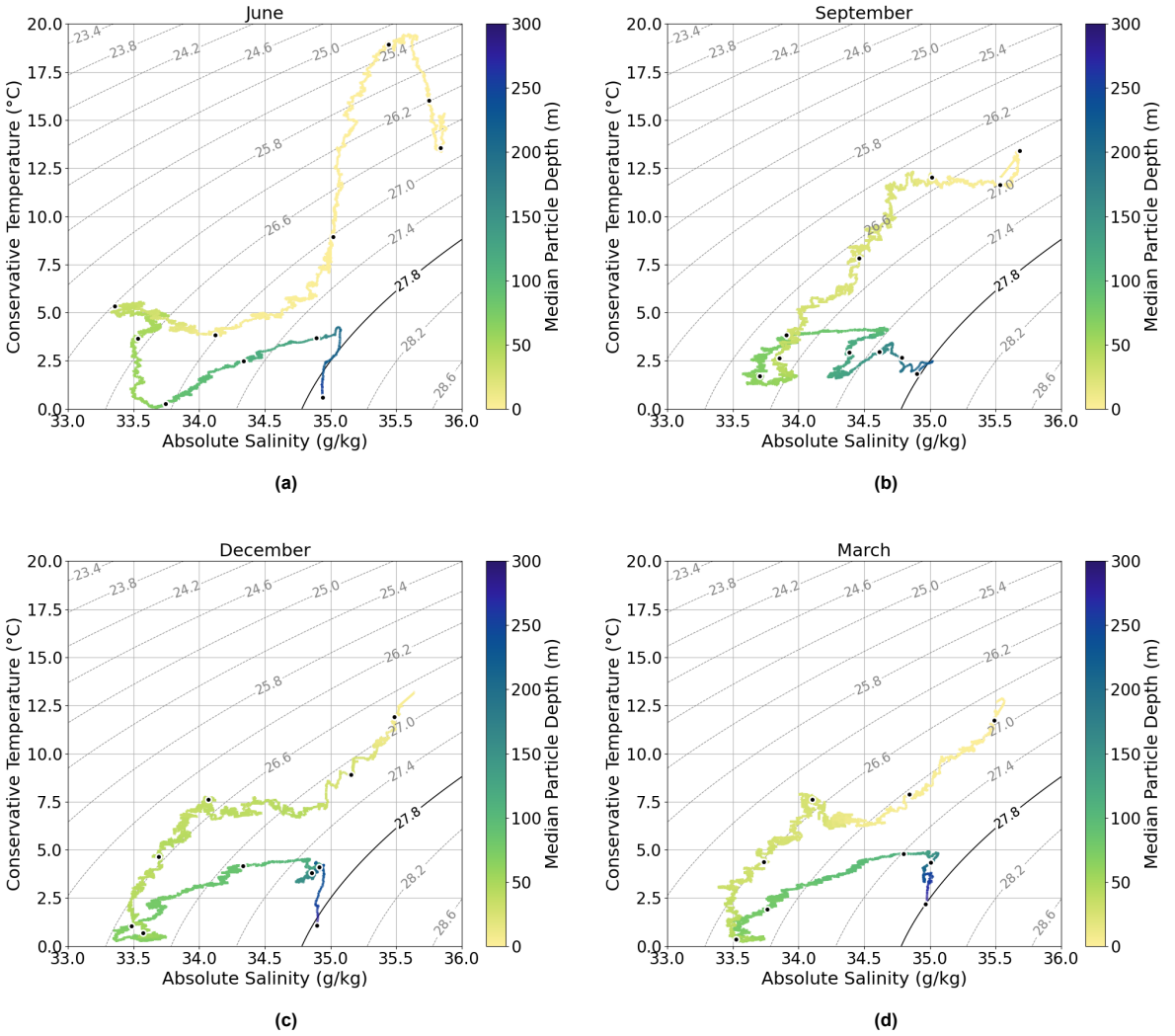

Figure A.6: T,S diagrams showing how median salinity (x-axis) and temperature (y-axis) evolve over time for particles categorised as BC-particles and seeded in **(a)** June '22, **(b)** September '22, **(c)** December '22 and **(d)** March '23. The dashed gray contours indicate isopycnals with the 27.8 kg/m^3 highlighted in solid black. The trajectory is coloured by median depth. The dots on the T,S evolution indicate intervals of 100 days since release.

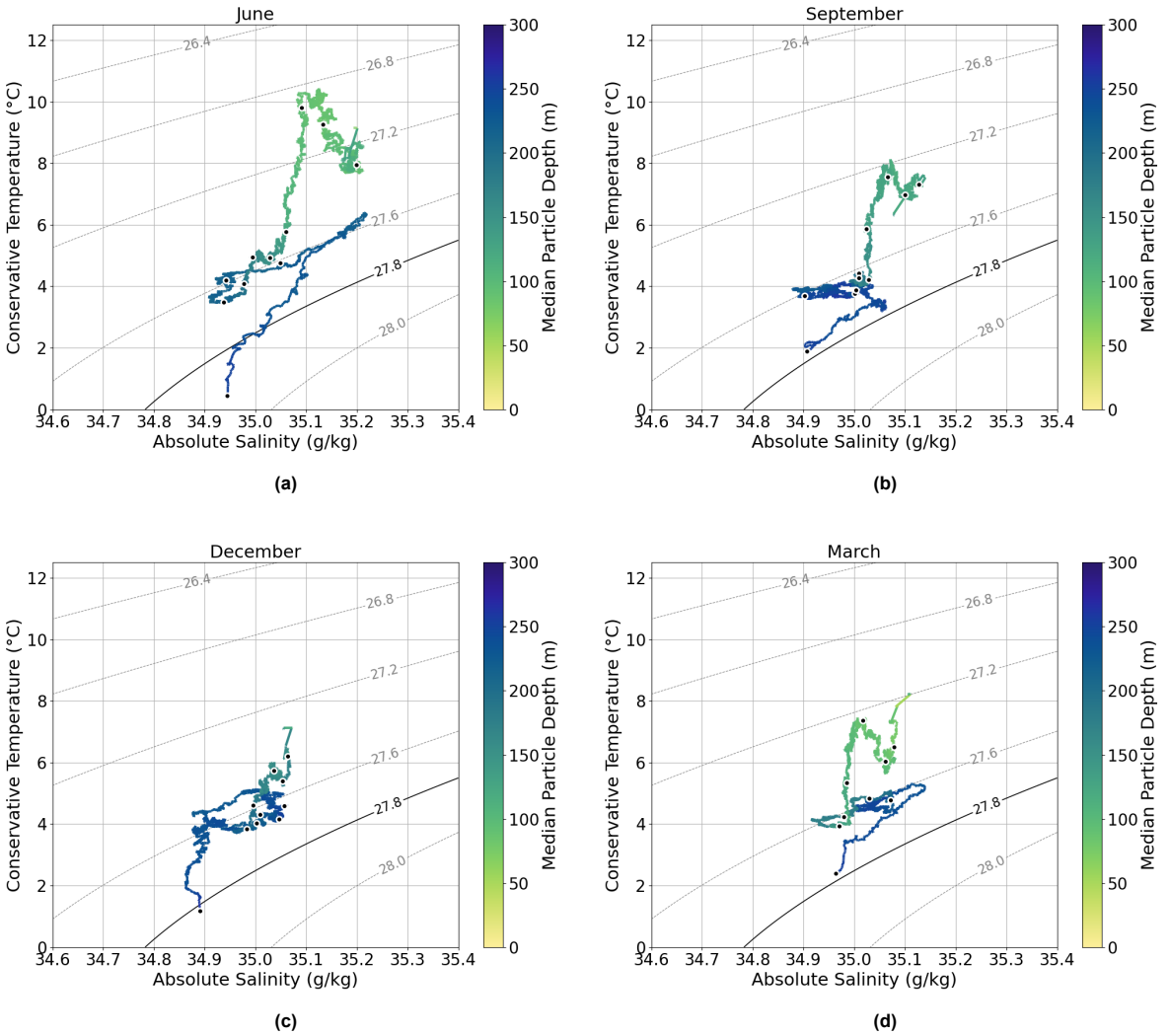

Figure A.7: As in Figure A.8, but for IrS-particles.

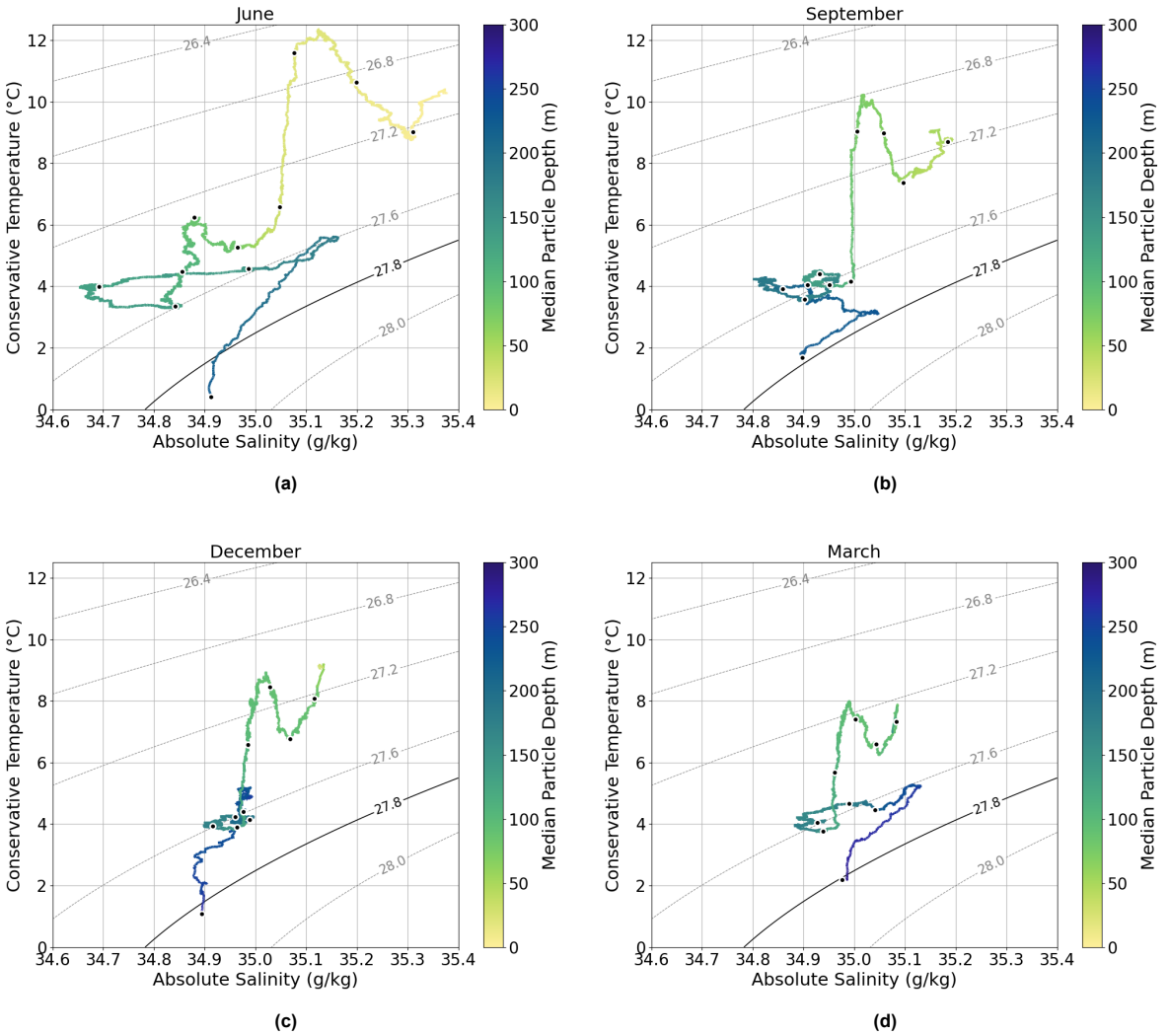

Figure A.8: As in Figure A.8, but for LS-particles.